Master of Science Thesis

Wing Optimisation for Tractor Propeller Configurations

Validation and Application of Low-Order Numerical Models Adapted to Include Propeller–Induced Velocities

H.K. Epema

June 26, 2017

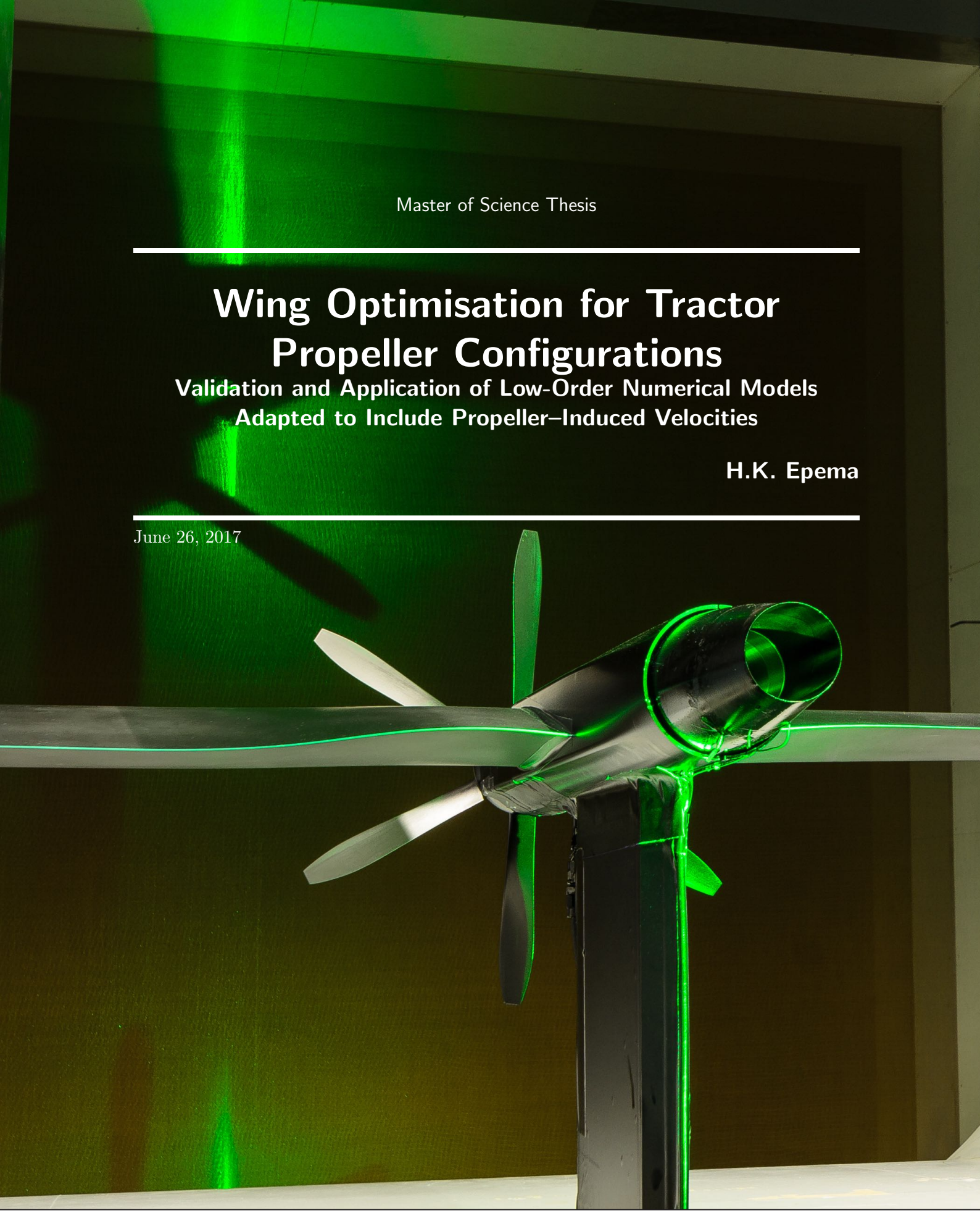

Aerodynamics

TU Delft

Faculty of Aerospace Engineering

Delft University of Technology

Wing Optimisation for Tractor Propeller Configurations

Validation and Application of Low-Order Numerical Models Adapted to Include Propeller–Induced Velocities

Master of Science Thesis

For obtaining the degree of Master of Science in Aerospace Engineering
at Delft University of Technology

H.K. Epema

June 26, 2017

Faculty of Aerospace Engineering · Delft University of Technology

Delft University of Technology

DELFT UNIVERSITY OF TECHNOLOGY
DEPARTMENT OF AERODYNAMICS

The undersigned hereby certify that they have read and recommend to the Faculty of Aerospace Engineering for acceptance the thesis entitled **"Wing Optimisation for Tractor Propeller Configurations"** by **H.K. Epema** in fulfillment of the requirements for the degree of **Master of Science**.

Dated: June 26, 2017

Supervisors:

ir. T. Sinnige

prof. dr. ir. L.L.M. Veldhuis

dr. ir. R. Vos

dr. A. Sciacchitano

Summary

Even though propellers are the oldest form of propulsion in aviation, propeller aircraft are still used today. The superior efficiency of propellers over jet engines is an important benefit in certain market segments. This is true for small aircraft in general aviation, passenger aircraft flying the shorter/regional routes and for the increasing market of Unmanned Aerial Vehicles (UAVs). This thesis focuses on the aircraft with two wing-mounted propellers. These aircraft experience strong propeller–wing interactions which affects the aerodynamic performance of the vehicle. This performance is of course crucial for the always important challenge to reduce fuel consumption (and therefore operating costs) or increase endurance or range.

This thesis focuses on optimising the wing in tractor propeller configurations in order to minimise the induced or total drag, with constant lift. This is done by modelling the propeller–wing interaction with low-order numerical models. These models are implemented and validated for predicting the differences in lift distribution due to changes in the wing chord and twist distribution. Thereafter, the models are used for the optimisation of the wing twist and chord distribution.

In this thesis only the time-averaged effects of propeller–wing interaction are considered. Even though the aerodynamics involved in the interaction is of an unsteady nature, it is shown in literature that for design purposes considering only the time-averaged effects is sufficient. These time-averaged effects can be put into two categories: the effect of the propeller on the wing and the effect of the wing on the propeller and its slipstream. The effects in the first category are captured with a Lifting Line and Vortex Lattice Method, both adapted to include the effect of the propeller-induced velocities on the wing, respectively called Adapted LL and Adapted VLM. The effects in the second category are modelled with a propeller analysis tool (XROTOR) and a combination of slipstream models. These slipstream models are for the slipstream contraction, deflection, axial development of the axial velocity and swirl recovery. The Adapted LL and VLM models use XROTOR and the slipstream models for the propeller-induced velocities on the wing. Two corrections are applied in these combinations of models: a swirl recovery factor (SRF) is applied to the propeller-induced tangential velocity and the axial velocity component of the propeller-induced velocities is removed from the equation for the lift ($l = \rho\Gamma(V_\infty + u_w)$ instead of $l = \rho\Gamma(V_\infty + u_w + u_p)$). Next to these models, an analytic

solution for the optimal lift distribution for minimum induced drag is implemented and is referred to as the AN.

The result of the Adapted LL and Adapted VLM models, are compared with the existing experimental data. This shows a valid prediction of the integral lift and lift distribution for the Adapted VLM model. The Adapted LL displays the correct behaviour, but is not accurate for absolute values. Therefore, the Adapted VLM is the preferred method in this thesis. The integral induced and total drag are also compared with the same experimental data. While these results show that the total drag is only accurate to the right order of magnitude, the prediction of the induced drag is accurate. The comparison with this experiment confirms the need of the SRF and the choice to modify the equation for the local lift. The velocities in the propeller slipstream were obtained from XROTOR. Based on a comparison of the integral propeller thrust with existing experimental data, it is concluded that XROTOR provides an adequate prediction of the propeller performance.

A wind tunnel experiment was performed in order to validate the capability of the numerical models to predict the changes in lift distribution due to changes in the wing chord and twist distribution. Therefore, a propeller mounted in front of a Control and Modified wing was tested in the Open Jet Facility of Delft University of Technology. The wing was mounted against a wall that acted as a symmetry plane. This setup simulated a twin engine propeller aircraft with both propellers rotating inboard-up. Planar particle-image velocimetry (PIV) measurements were performed on cross-sections around the wing on 11 locations along the wingspan. The acquired velocity fields were used to determine the circulation on every wingspan location. The propeller slipstream was characterised by a Planar PIV measurement of the axial cross-section on top of the nacelle and by total and static pressure measurement on the horizontal line inside the slipstream perpendicular to the flow direction. The thrust was estimated based on the pressure measurement and the axial velocity found in the flow field acquired by the PIV measurement.

The experimental results of the propeller slipstream are used to validate the slipstream models. Small differences between the experimental results and what the models predict are found for the slipstream contraction, deflection and axial development. The swirl recovery could not be validated. For the propeller thrust an overprediction by XROTOR of 15% is found. However, in general the propeller-induced axial velocity is predicted adequately. It is therefore assumed that this is also true for the propeller-induced tangential velocity.

The flow fields around the wing show the expected behaviour. For every location outside of the slipstream (propeller-off configuration included), the typical flow field around an airfoil is found: accelerated flow over the top of the airfoil, decelerated flow below, a stagnation point on the nose and a lower wake velocity directly behind the airfoil. When the propeller is on, the flow around the wing inboard of the slipstream indicates a slight increase of the lift. Inside the slipstream, the increase in axial velocity and the upwash or downwash are very clear. On the edges of the slipstream, the shear effect the wing surface has on the slipstream is clearly visible. Comparing the Control and Modified wing shows the flow behaves as expected, indicating an increase of the lift when the twist angle is higher and vice versa. The lift distribution that is extracted via the circulation found in every flow field shows the typical propeller–wing interaction effects: the lift increases behind the upgoing blade, decreases where the blade goes

down and changes correspondingly outside the slipstream. The lift distribution predicted by the Adapted VLM follows the same trend, however it does fall outside of the measurement error range in the experimental results. This is mainly due to the error in the SRF model. Inside the slipstream, the lift is overpredicted both behind the upgoing blade as well as the downgoing one. Therefore, the effect of the SRF is not strong behind the upgoing blade, while it is too strong behind the downgoing one. This indicates the swirl recovery needs to be modelled as a factor that varies along the wingspan, instead of one constant factor for the whole slipstream. Even though the lift distribution prediction by the Adapted VLM model falls outside the measurement error range, the changes in the lift distribution due to wing twist changes are captured well.

Although the Adapted VLM model contains inaccuracies in predicting the lift and drag distributions, it does follow the correct trend in the lift and drag distribution on one wing as well as the changes between two different wings. It can therefore be used for optimisation studies, as long as the results are carefully interpreted. This means that qualitative design choices based on the results of the Adapted VLM are expected to be correct, while the absolute values of the resulting design can be inaccurate. For example, it is found that the twist angle of the wing section behind the upgoing blade must be decreased to find the best compromise between the local beneficial effect of the propeller-induced upwash and the local counteracting effect of the wing-induced downwash. This effect is considered to be accurate. The wing design resulting from an optimisation with the Adapted VLM model might say this twist angle must be -2 deg. This specific design value can be inaccurate and should be verified with higher-order numerical models or a wind tunnel experiment.

The Adapted VLM is used to investigate the behaviour of the optimum wing chord and twist distribution for a propeller–wing interaction problem. First, the investigation into the optimal lift distribution show that the AN method does not predict this correctly. The effect of the wing on the propeller and slipstream cannot be neglected. Second, it is used to investigate the behaviour of the optimum wing chord and twist distribution for minimum induced/total drag, while keeping the lift constant. It is shown that the optimal lift distribution for minimum induced drag is not predicted correctly by the Adapted AN model. This model neglects the effects of the wing on the propeller and slipstream, which is likely the cause for the error. A small reduction of the induced drag is possible by changing the twist distribution. The main reduction is realised in the propeller-induced upwash region, where the twist angle is decreased (aligning the wing section more with the incoming flow). The total drag can also be reduced by changing the chord and twist. The twist distribution is similar to the twist distribution for minimum induced drag, only with smaller amplitudes. The wing chord is reduced on the largest part of the wing, which reduces the viscous drag and helps in the reduction of the induced drag.

In conclusion the Adapted VLM model is used successfully to study the optimum wing chord and twist distribution for minimum induced/total drag. Even though the result should be carefully interpreted, the model is ready to be used on a real aircraft wing in order to determine the how much drag reduction is really possible.

Table of Contents

Nomenclature

Abbreviations

AN	Analytical solution for optimal propeller–wing interaction (Section 3.1)
AR	Aspect ratio
CNC	Computer Numerical Control
FOV	Field Of View
LE	Leading Edge
LL	Lifting Line method
MAC	Mean Aerodynamic Chord
MTOW	Maximum Take-Off Weight
OJF	Open Jet Facility (open jet wind tunnel at Delft University of Technology)
PIV	Particle Image Velocimetry
SI	Slipstream model I (as defined in Section 3.5)
SII	Slipstream model II (as defined in Section 3.5)
SIII	Slipstream model III (as defined in Section 3.5)
SIV	Slipstream model IV (as defined in Section 3.5)
SV	Slipstream model V (as defined in Section 3.5)
TE	Trailing Edge
UAV	Unmanned Aerial Vehicle
VLM	Vortex Lattice Method

Coefficients

$c_d = \frac{d}{q_\infty c}$	Drag coefficient [-]
$C_D = \frac{D}{q_\infty S}$	Drag coefficient [-]
$c_l = \frac{l}{q_\infty c}$	Local lift coefficient[-]
$C_L = \frac{L}{q_\infty S}$	Lift coefficient [-]
$C_T = \frac{T}{\rho n^2 D^4}$	Thrust coefficient [-]
$c_{l_\alpha} = \frac{\mathrm{d}c_l}{\mathrm{d}\alpha}$	Lift curve slope [1/rad]
$T_c = \frac{T}{\rho V^2 D^2}$	Thrust coefficient [-]

Greek Symbols

α	Angle of attack [rad]
β	Propeller blade pitch [deg]
Γ	Circulation [m^2/s]
λ	Lagrange multiplier [-]
ν	Kinematic viscosity [m^2/s]
ρ	Air density [kg/m^3]
σ	Standard deviation [-]
θ	Alternative spanwise coordinate [rad]
θ	Wing twist angle [deg]
ε	Error [-]

Latin Symbols

$\mathbf{f}$	Local force vector [N/m]
$\mathbf{l}$	Length of an vortex element [m]
$\mathbf{n}$	Normal unit vector [-]
$\mathbf{V}$	Velocity vector [m/s]
A	Area [m^2]
A	Fourier series coefficient [-]
B	Propeller blade count [-]
b	Wing span [m]
c	Wing chord [m]
D	Diameter [m]
D_{ind}	Induced drag force [N]
d_{ind}	Local induced drag force [N/m]
D_{tot}	Total drag force [N]
d_{tot}	Local total drag force [N]
D_{visc}	Viscous drag force [N]
d_{visc}	Local viscous drag force [N/m]
f	Cost function
$J = \frac{V}{nD}$	Advance ratio [-]
L	Characteristic length (for Reynolds number) [m]
L	Lift force [N]
l	Local lift force [N/m]
M	Mach number [-]
n	Propeller rotational velocity [rev/s]
n	Station along the wingspan [-]
p_{static}	Static pressure [N/m^2]
p_{tot}	Total pressure [N/m^2]
$q = \frac{1}{2}\rho V^2$	Dynamic pressure [N/m^2]
R	Propeller radius [m]

r	Radial coordinate [m]
$Re = \frac{VL}{\nu}$	Reynolds number [-]
S	Wing area [m^2]
T	Thrust [N]
u	Velocity component in freestream (x) direction [m/s]
V	Velocity [m/s]
v	Spanwise velocity component (y direction) [m/s]
w	Downwash [m/s]
w	Downwash velocity component (z direction) [m/s]
y	Wing span coordinate [m]

Subscripts

0	Considering the local coordinate
∞	At freestream conditions
a	Axial component
Cw	Considering the Control wing
c	Considering the chord
d	Considering the downstream value
eff	Effective
g	Geometric
hub	Considering the propeller hub
ind	Induced (drag or angle of attack)
$l = 0$	For local lift equal to zero
pOff	Considering propeller off case
pOn	Considering propeller on case
root	Considering the root of either the wing or propeller
r	Radial component
tip	Considering the tip of either the wing or propeller
tot	Total (drag)
t	Tangential component
u	Considering the upstream value
visc	Viscous (drag)

Chapter 1

Introduction

Even though propellers are the oldest form of propulsion in aviation, propeller aircraft are still used today. The superior efficiency of propellers over jet engines is an important benefit in certain market segments. This is true for small aircraft in general aviation, passenger aircraft flying the shorter/regional routes and for the increasing market of Unmanned Aerial Vehicles (UAVs). This thesis focusses on the aircraft with two wing-mounted propellers. These aircraft experience strong propeller–wing interactions which affects the aerodynamic performance of the vehicle. This performance is of course crucial for the always important challenge to reduce fuel consumption (and therefore operating costs) or increase endurance or range.

The propeller–wing interaction effects can be beneficial for the performance of the aircraft. For example, Miranda and Brennan (1), Kroo (2) and Veldhuis (3) show that, due to swirl recovery, a wing with an inboard up rotating propeller experiences a higher lift/drag ratio with respect to the case without propeller. Besides this effect, the wing design itself can be optimised to increase the performance. Veldhuis (3), Rakshith et al. (4) and Alba (5) used low-order numerical models to predict the propeller–wing interaction effects by adapting the standard Lifting Line (LL) and Vortex Lattice Method (VLM) models to include the propeller-induced velocities on the wing. The models are used to optimise the wing twist and chord distribution in order to minimise either the induced or total drag, while keeping the lift constant. However, a validation of either the numerical model to use for the optimisation, or of the optimum design itself are still missing in literature.

This thesis aims to validate the use of the low-order numerical models for optimisation. This is done by predicting the lift and drag distribution on two different wings and comparing them with the results of a wind tunnel experiment involving the same two wings. Such a validation is important because, for optimisation, the effect of changes made to the wing design need to be predicted correctly. The numerical models need to have fast run times since optimisation requires a large number of design iterations. Therefore, the models need to be of low-order, like the LL and VLM.

This leads to the following research objective:

Validation and application of low-order numerical models, adapted to include propeller–wing interaction effects, for the optimisation of the wing chord and twist distribution in a tractor propeller configuration. The low-order numerical models involved are:

1. *an analytic solution for the optimum lift distribution for minimum induced drag (AN).*
2. *a Lifting Line (LL) and a Vortex Lattice Method (VLM) both adapted to include the effects of propeller-induced velocities.*
3. *the propeller analysis code called XROTOR.*
4. *slipstream models for the propeller-induced velocities on the wing.*

In order to reach this objective the following steps are performed:

1. Introduce the relevance of this thesis: propeller–wing interaction effects are an important design consideration for twin propeller aircraft. Low-order numerical models, considering the propeller–wing interaction effects, are used to optimise the wing twist and chord distribution in order to minimise induced/total drag with constant lift. The capability of these models to be used for optimisation needs to be validated.
2. Determine from literature the aerodynamic flow effects of the propeller–wing interaction relevant for the design of the chord and twist distribution of the wing.
3. Implement four low-order numerical models mentioned in the research objective. The LL and VLM are adapted to account for the propeller induced velocities. These velocities are based on the far downstream slipstream velocity results of XROTOR and corrected with the slipstream models. The correction are applied for the slipstream contraction, axial development, slipstream deflection and swirl recovery.
4. Validate the correct implementation of the numerical models. This is done by comparing the results for lift and drag, by the LL and VLM models, on an isolated elliptical wing for the propeller-off configuration with the analytical solution. The same is done with the existing experimental results on a propeller–wing combination. Finally, the thrust results of XROTOR are validated using existing experimental data.
5. Perform a wind-tunnel experiment on a propeller–wing combination to determine the lift distribution using planar particle-image velocimetry (PIV). Characterize the propeller slipstream with planar PIV and total and static pressure measurements. From the slipstream results the propeller thrust is estimated.
6. The wind-tunnel results of the slipstream are compared with the predictions made by XROTOR and the different slipstream models.
7. Using the results from the wind-tunnel experiment on the wing, the numerical models are validated for predicting the lift distribution for a change in twist distribution along the wing.
8. The numerical models are used to optimise the wing chord and/or twist distribution for minimum induced/total drag with constant lift. The optimisation is performed on the Control wing and on a representative UAV wing.
9. Conclude on the applicability the AN, LL and VLM models to perform optimisation of the wing chord and twist distribution for minimum induced/total drag. Make recom-

mendations on what the next steps are in improving in these numerical models.

The steps described above correspond to the chapters in this report. A roadmap of the thesis is shown in Figure 1.1 to indicate how the different steps and chapters are linked together.

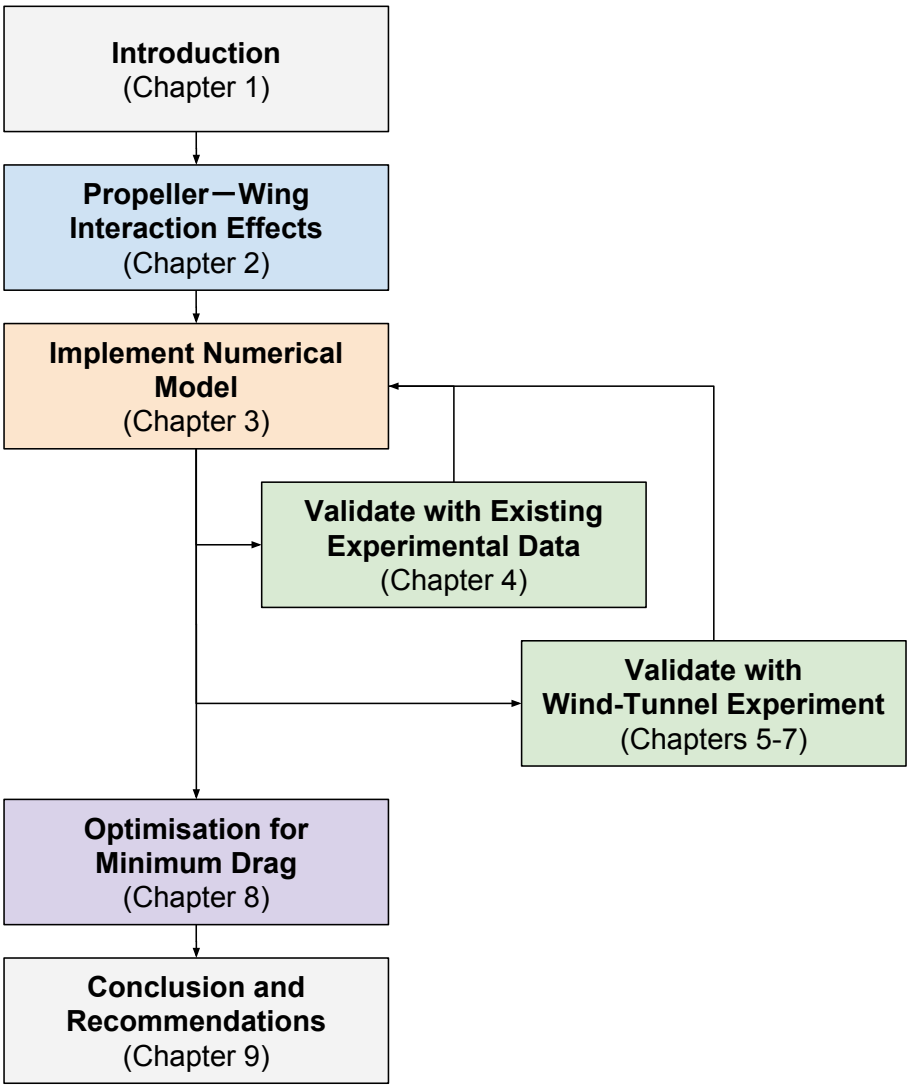

Figure 1.1: Thesis roadmap.

Chapter 2

Propeller–Wing Interaction Effects

On a wing-mounted propeller, a mutual interaction between the propeller and wing exists. These propeller–wing interaction effects are unsteady in general. Regarding the unsteadiness, Cho and Cho (6) show that when the induced velocities in the propeller plane and slipstream are circumferentially averaged, which removes the time dependency, that useful performance predictions of the wing can be made. This simplification has been used by Veldhuis (3), Rakshith et al. (4) and Alba (5) for the optimisation of the wing accounting for propeller–wing interactions.

Therefore, for the performance (lift and drag) of the wing, considering the time-averaged effects is sufficient. This is done in this thesis: it considers the time-averaged effects of the propeller–wing interaction and neglects the unsteady effects.

This chapter introduces the relevant, time-averaged, effects of propeller–wing interaction in Section 2.1. Also, it discusses the relevance of compressibility and Reynolds number effects in Sections 2.2 and 2.3, respectively.

2.1 Time-Averaged Effects

The time-averaged effects can be divided into three groups and are discussed in the following subsections: the propeller slipstream changing the inflow conditions of the wing (Subsection 2.1.1), the wing changing the inflow conditions of the propeller (Subsection 2.1.2) and the slipstream deformation (Subsection 2.1.3).

2.1.1 Effects of the Propeller Slipstream on the Wing

The propeller changes the inflow conditions of the section of the wing that is washed by the slipstream. The flow inside the slipstream is characterised by an increase of the axial velocity

and tangential velocity. On the wing, these additional velocities affect the lift, induced drag and viscous drag distribution. However, the changes on the wing are not limited to the wing section that is washed by the slipstream. A good summary of these effects is given by Veldhuis (3) and is repeated here for clarity. Four zones of influence are identified in Figure 2.1, which also shows the change in lift distribution due to the propeller slipstream effect on the wing. In the following explanation a wing with a wing-mounted, inboard-up rotating propeller is considered; for outboard-up the effects are similar but reversed as is shown in Figure 2.1.

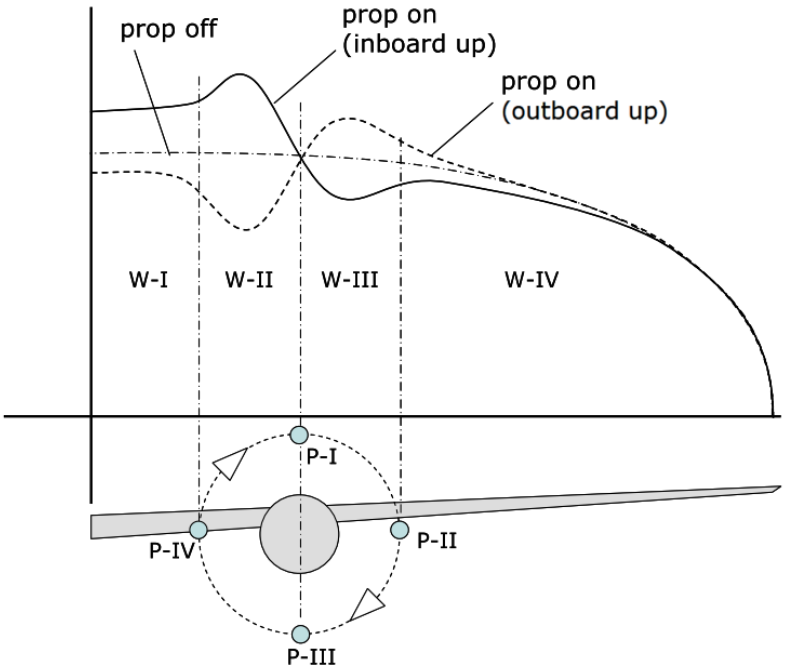

Figure 2.1: Changes in wing lift distribution due to propeller–wing interaction. The wing is divided into four zones and four locations for the propeller blade are identified. Image taken from Veldhuis (3) and annotations P-I to P-IV.

- Starting with zone W-II, inside the slipstream behind the upgoing blade the lift is increased with respect to the propeller-off case due to two effects: the increase of axial velocity (or dynamic pressure) and the angle of attack increase due to the upwash velocity in the slipstream (the tangential velocity inside the slipstream is an upwash on the wing behind the upgoing blade).
- Zone W-III is also inside the slipstream, but because this section is behind the downgoing blade the wing experiences a downwash. This results in a decrease of the lift. With respect to the propeller-off case, the dip in the lift is smaller than the peak in zone W-II. This is because the decrease in lift due to the downwash is counteracted somewhat by the local increase in axial velocity.
- Even though zone W-I is not washed by the propeller slipstream, the lift actually increases with respect to the propeller-off case. The cause of this lies in zone W-II. Here the lift increases and leaves a trailing vortex around the inboard edge of the slipstream. This vortex induces an upwash in zone W-I, which increases the local angle of attack and therefore the lift as well.

- A similar, but reversed, effect occurs in zone W-IV. The decrease of lift with respect to the propeller-off case in zone W-III leaves a trailing vortex on the outboard edge of the slipstream. This vortex induces an downwash in zone W-IV, which results in a decrease of the angle of attack and therefore a lower lift. In the middle of the slipstream, on the propeller axis, another trailing vortex is created by the changes in the lift distribution. This vortex actually counteracts the effects described for zone W-I and W-IV. However, since it is further apart from these zones, its effect is also smaller. Therefore, the effects of the other two trailing vortices are dominant.

Besides the lift, the drag changes as well. The induced drag distribution changes due to the upwash and downwash in the propeller slipstream. Behind the upgoing blade, where the wing experiences a propeller induced upwash, the local angle of attack increases. This also means the local lift vector points more forward with respect to the propeller-off case. Therefore, the local induced drag decreases. It can even become negative (and therefore thrust) when the upwash is strong enough. In the downwash region behind the downgoing blade, the angle of attack decreases and therefore the induced drag increases. With an inboard-up rotating propeller the positive effect behind the upgoing blade is larger than the negative one on the downgoing side. This is because the lift is stronger on the inboard wing. Therefore, an inboard-up rotating propeller performs better in terms of induced drag with respect to an outboard-up rotating one. This was confirmed experimentally by Veldhuis (3). The viscous drag increases inside the propeller slipstream due to the increase in dynamic pressure. The viscous drag is further modified by local angle of attack changes on the wing.

2.1.2 Effect of the Wing on the Propeller

The wing influences the inflow conditions of the propeller. Due to the upwash in front of the wing, the propeller blade experiences a different local angle of attack throughout a full revolution. This effect is similar as for a propeller at an inclination angle. Veldhuis (3) defines four locations of the propeller blade (see locations P-I to P-IV in Figure 2.1) and explains the changes due to the wing upwash. An inboard-up rotating propeller, mounted in front of the wing, is considered in the following explanation; for an outboard-up rotating propeller the effects at P-II and P-IV are reversed.

- At P-II the blade goes down and experiences a higher tangential velocity component with respect to the isolated propeller case. This is because the propeller blade rotates against the upwash of the wing. The higher tangential velocity increases the local angle of attack of the blade and therefore also increases the blade loading at this location. Figure 2.2 shows the effect the upwash of the wing has on the local blade angle of attack for the locations P-II and P-IV.
- The blade at P-IV experiences a lower blade loading because the upwash induced by the wing is now in the same direction as the propeller blade rotation. This reduces the effective velocity and therefore the local angle of attack.
- P-I is the blade location where a slightly higher axial velocity is induced by the wing, with respect to the propeller axis (flow is accelerated over the top of the wing, which

starts already in front of the wing). Due to a higher axial velocity the angle of attack perceived by the blade and therefore blade loading decreases.

- At P-III the effect is opposite to that experienced at P-I. A slightly lower axial velocity induced by the wing causes a higher blade loading.

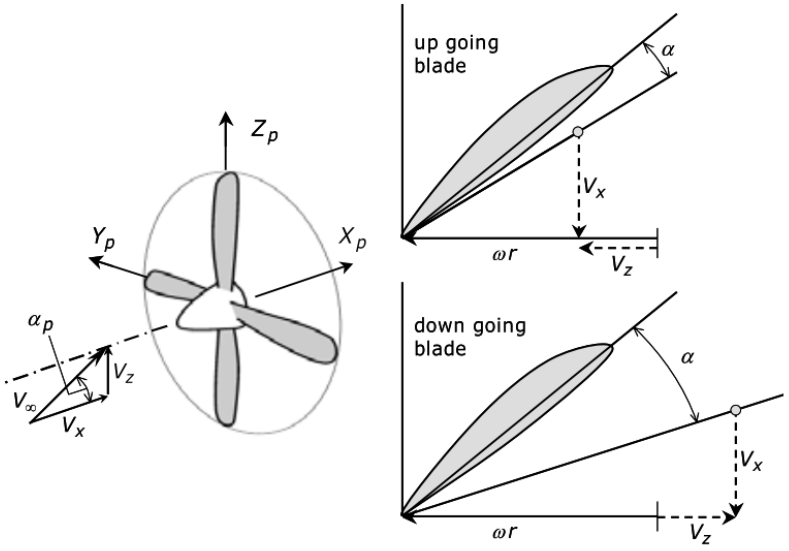

Figure 2.2: The propeller experiences varying angle of attack when it is in the upwash (V_z) of the wing. When the blade goes up the angle of attack decreases, when the blade goes down the angle of attack increases (3).

Even though the effects the blade perceives at locations P-I to P-IV are explained for these discrete locations, the blade loading will change continuously as it rotates through the positions P-I to P-IV. Figure 2.3 shows how the blade loading changes over the propeller plane, for a propeller at a nonzero inclination angle α. This confirms the continuous change of the blade loading, but it also shows another interesting effect. Namely the maximum and minimum blade loading is shifted with approximately 30 degrees with respect to the locations P-II and P-IV, respectively. Gonzalez-Martino et al. (7) attributes this to the interaction of the propeller blades with their trailing wake.

The fact that the blade loading varies with the circumferential position undoubtedly also means the velocities inside the slipstream are not axissymmetric. These effects, however, are neglected in the numerical models used in this thesis. The reason for this is twofold: one, modelling these effects requires a technique to analyse the propeller with a free moving wake (7). This is possible as Gonzalez-Martino et al. (7) show, however, the runtime of the model may become unacceptably high for design purposes. Second, as mentioned earlier, Cho and Cho (6) show, the performance of the wing (in terms of lift and drag) can be predicted with acceptable accuracy for design purposes when the slipstream velocities are circumferentially averaged.

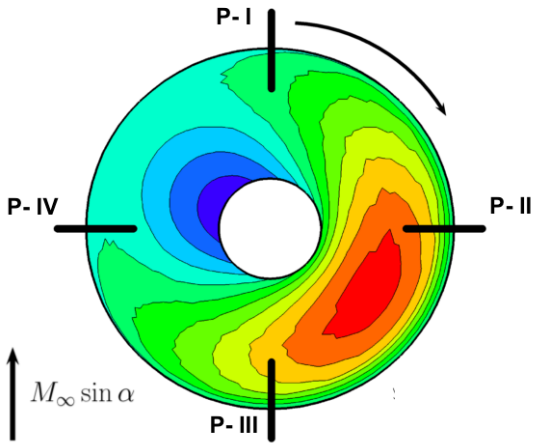

Figure 2.3: Typical blade loading distribution in the propeller plane for a propeller at a nonzero inclination angle α. Image taken from Gonzalez-Martino et al. (7), mirrored to match inboard-up in Figure 2.1 and added annotations P-I to P-IV.

2.1.3 Slipstream Deformation

The propeller slipstream deforms under its own influence and due to wing induced velocities.

An isolated propeller increases the axial and tangential velocity inside the slipstream. The axial velocity continues to accelerate behind the propeller plane, while the development of the tangential velocity is almost instant. Just behind the propeller plane the static pressure is increased with respect to just in front of the propeller plane. Moving downstream, the static pressure gradually recovers towards the freestream static pressure. This effect causes the axial velocity to keep on developing (following to Bernoulli's principle, which is conservation of energy) until the static pressure is fully recovered. While the axial velocity increases the slipstream radius decreases in radial direction with respect to the propeller radius. This is due to mass conservation. These effects are called slipstream contraction and axial development of the slipstream.

When the propeller is operating in front of the wing some additional effects occur (on top of the slipstream contraction and axial development of the slipstream):

- First, the upwash in front of the wing causes the propeller to virtually operate at a nonzero inclination angle. The propeller creates a force normal to the freestream as a result of it. In turn, the slipstream bends slightly downward because of conservation of momentum. Another effect of the wing induced velocities is the following: in front of the wing the upwash bends the slipstream upwards (counteracting the downward deflection due to the propeller normal force) and behind the wing the downwash bends the slipstream back down. In this thesis these two effects are called slipstream deflection.
- Second, when the slipstream impinges on the wing it is cut into two halves. While the slipstream moves over the wing surface it also displaces, such that when leaving the wing the slipstream is sheared. Figure 2.4 shows the contour lines of total pressure behind

a wing with tractor propeller configuration. The shearing of the slipstream is clearly recognisable in this figure: the upper part of the slipstream is displaced outboard and the lower part inboard. This is caused by the velocities the mirror vortices induce on the tip vortices when they move over the wing surface. This is explained by Witkowski et al. (8) as follows: when the tip vortex moves over the wing surface there is a small component of this vortex in the x-axis (in the direction of flight). Since the wing surface acts as a symmetry plane the tip vortex has a virtual mirror vortex on the other side of the wing surface. The mirror vortex induces a velocity on the tip vortex which causes it to displace. The direction of displacement following this explanation is in agreement with the slipstream shearing found in Figure 2.4.

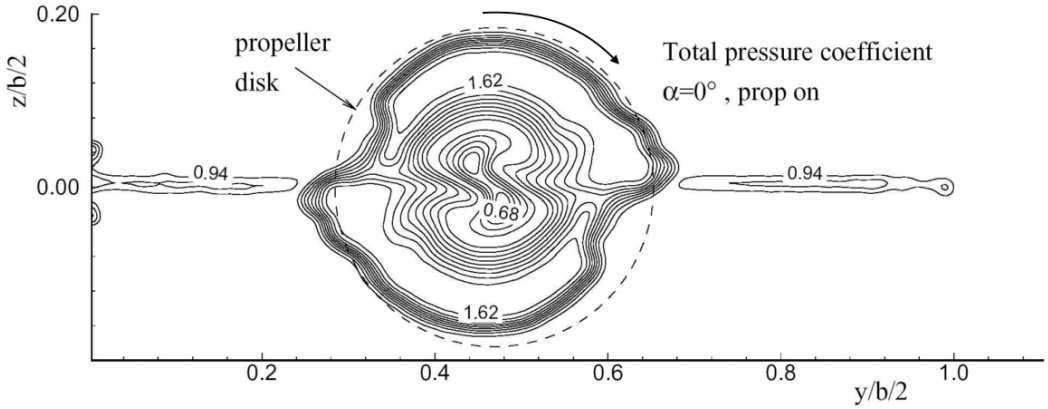

Figure 2.4: Contour lines of the total pressure coefficient measured 1 chord length behind the wing with a propeller running inboard-up, wing is at $\alpha = 0$ deg (3).

2.2 Effect of Compressibility

Depending on the Mach number, the flow experiences some kind of compressibility. For low Mach numbers, $M < 0.3$, the flow behaves as if it were not compressible (9). In the range of Mach numbers $0.3 < M < 0.8$, the effect of compressibility is noticeable. In this regime the flow can be modelled similarly as for the low Mach number regime, as long as a compressibility correction is applied (9). This can be done, for example, with the Prandtl-Glauert compressibility correction. For even higher Mach numbers like $0.8 < M < 1.2$, which is transonic flow, the compressibility is extremely important. In this regime the compressibility cannot be neglected, nor can it be corrected for, and it needs another way of modelling the flow. This is outside of the scope of this thesis.

To show it is reasonable to consider the flow regime below $M = 0.8$, the Mach numbers for the aircraft considered in this thesis are determined. This is done for two types of aircraft: twin propeller variants of UAVs and passenger aircraft. The UAVs generally operate at very low Mach numbers ($M < 0.3$), this holds for both the wing as well as the propellers. This means that compressibility is not of concern for such UAVs. The passenger aircraft operate at higher velocities and altitude and therefore higher Mach numbers. For example, the wing

of the Fokker 50 operates at $M \approx 0.5$ and its propeller tip at $M \approx 0.75$ (based on 1200 RPM (3), propeller radius of $R = 1.83$m and the speed of sound at 7,500 meter). This means compressibility is definitely important for the Fokker 50 and similar passenger aircraft, but it is also falls in the range where the compressibility correction can be used. This is true as long as the Mach number, of in particular the propeller tip, does not exceed $M = 0.8$.

2.3 Effect of Reynolds Number

The Reynolds number at which the wing or propeller operates, affects the characteristics of the boundary layer. Miley (10) defines 'low Reynolds numbers' (based on the chord) to be $Re_c < 4 \cdot 10^6$ and the rest are 'high Reynolds numbers'. When the flow is above this Reynolds number the boundary layer is almost certain to transition from laminar to turbulent. For low Reynolds numbers this is not a guarantee as the flow might first separate before transition to turbulent flow occurs. This is important since the turbulent boundary layer has a higher skin friction drag with respect to a laminar one. However, separated flow increases the drag even more.

This has a few implications on the aircraft that are considered in this thesis. The Reynolds number for passenger aircraft is typically high, for example the Fokker 50 operates at $Re = 22 \cdot 10^6$ during cruise. Therefore, the flow in the boundary layer on the wing is in the high Reynolds number regime and there is no risk of laminar separation. On UAVs, depending on their size and operating speed, the Reynolds numbers are generally a lot lower. This means the UAVs can benefit from laminar flow over the wing when the Reynolds number is low enough. But special care must be taken in the design of the airfoil in order to prevent (or control) laminar separation.

Chapter 3

Low-Order Modelling Techniques for Propeller–Wing Interactions

This chapter discusses the low-order modelling techniques for the propeller–wing interaction effects. The analytic solution for the optimal lift distribution for a propeller–wing combination is described in Section 3.1. The Lifting Line in Section 3.2 and Vortex Lattice Method in Section 3.3 show models for the wing analysis and account for the propeller-induced velocities effect on the wing. The propeller-induced velocities are modelled as explained in Section 3.4.

3.1 Analytical Solution of Optimal Lift Distribution for Minimum Induced Drag (AN)

The analytic solution of the optimal lift distribution for minimum induced drag for a propeller–wing combination is implemented based on the work of Kroo (2). This method models the propeller with a helical wake, without the effects of contraction. The wing is modelled with a flat wake, without the wake rollup. The generalised version of Munk his stagger theorem (11) is used to justify placing the propeller far upstream of the wing. The benefit is that the effect of the wing on the propeller does not have to be computed. Instead, only the effect of the propeller-induced velocities in the slipstream on the wing is considered.

The method of Kroo is implemented with one correction: the axial velocity induced by the propeller is removed from the equation for the local and integral lift. The reason for this is explained in Section 3.3.2 and Appendix A. The optimal lift distribution is found by solving this objective function for minimum induced drag and constant lift:

$$\text{Obj} = D_{\text{ind}} + \lambda \left(L - \frac{4}{\pi b} \sum_n A_n I_{un} \right) \tag{3.1}$$

where λ is a Lagrange multiplier, b the wingspan, n the nth station along the wingspan. The lift L and drag D_{ind} given by:

$$L = \frac{4}{\pi b} \sum_n A_n I_{un} \tag{3.2}$$

$$D_{\text{ind}} = \frac{1}{q\pi b^2} \sum_n n A_n^2 + \frac{4}{\pi b} \sum_n A_n I_{un} \tag{3.3}$$

$$I_{un} = \int_{-b/2}^{b/2} \sin(n\theta)\ \mathrm{d}y \tag{3.4}$$

$$I_{wn} = \int_{-b/2}^{b/2} \sin(n\theta) w_p\ \mathrm{d}y \tag{3.5}$$

$$\theta = \arccos\left(\frac{2y}{b}\right) \tag{3.6}$$

where $q = \frac{1}{2}\rho V_\infty^2$ is the freestream dynamic pressure, w_p the propeller-induced downwash and y the coordinate along the wingspan. The solution for Equation 3.1 is given by (2):

$$A_n = \frac{\rho V_\infty b}{n} \left[\left(\frac{\pi}{4\rho V_\infty^2} + \sum_j \frac{I_{uj} I_{wj}}{j} \right) \left(I_{un} / \sum_j \frac{I_{uj}^2}{j} \right) - I_{wn} \right] \tag{3.7}$$

This result is substituted into the following equation to obtain the optimal lift distribution.

$$l = \frac{4}{\pi b} \sum_n A_n \sin(n\theta) \tag{3.8}$$

When the effect of the propeller induced velocities is removed ($w_p = 0$) the result reduces to the optimal lift distribution for an isolated wing, which the elliptical lift distribution as given for example by Abott and Von Doenhoff (12).

3.2 Lifting Line (LL)

3.2.1 Standard Formulation

The Lifting Line (LL) to analyse a finite wings dates back to Ludwig Prandtl. Here it is implemented based on his theory as explained by Anderson (9). The principle is as follows.

The wing is modelled by an infinite number of horseshoe vortices all with a certain circulation Γ. With this circulation the local lift force can be calculated with the Kutta-Joukowski theorem: $l = \rho_\infty V_\infty \Gamma$. Therefore, the distribution of circulation along the wingspan defines the distribution of lift.

At the same time, the local lift force can be calculated based on the local lift coefficient: $l = c_l \frac{1}{2} \rho_\infty V_\infty^2 c$. Equating both allows for the circulation to be solved. With the circulation known the lift and drag forces can be determined.

Circulation Distribution

The circulation is calculated by equating the local lift force defined by the Kutta-Joukowski theorem with the lift due to the effective angle of attack:

$$l = \rho_\infty V_\infty \Gamma = c_l \frac{1}{2} \rho_\infty V_\infty^2 c \tag{3.9}$$

with ρ_∞ and V_∞ the air density and velocity at free stream conditions, c the local wing chord and Γ the circulation. The local lift coefficient c_l is calculated by:

$$c_l = c_{l_\alpha} \left(\alpha_{\text{eff}} - \alpha_{l=0} \right) \tag{3.10}$$

Where c_{l_α} is the lift curve slope. For an airfoil in 2D this is in theory equal to $c_{l_\alpha} = 2\pi$ and it is used for this analysis. The effective angle of attack α_{eff} is defined as:

$$\alpha_{\text{eff}} = \alpha_g - \alpha_{\text{ind}} \tag{3.11}$$

Where α_g is the geometric angle of attack of the wing (which includes the angle of attack of the wing and the wing twist: $\alpha_g = \alpha_w + \alpha_t$) and the induced angle of attack is given by:

$$\alpha_{\text{ind}} = \tan^{-1} \left(\frac{w_w}{V_\infty} \right) \tag{3.12}$$

Here is w_w the downwash behind the wing (note that the orientation is downward positive, thus w_w is positive when it points down). It is assumed to be much smaller than the free stream velocity V_∞. Therefore the equation for the induced angle of attack can be simplified to:

$$\alpha_{\text{ind}} = \frac{w_w}{V_\infty} \tag{3.13}$$

The downwash is given by (for a derivation of this result the reader is referred to Anderson (9)):

$$w_w = \frac{1}{4\pi} \int_{-b/2}^{b/2} \frac{\frac{\mathrm{d}\Gamma}{\mathrm{d}y}}{y_0 - y} \, \mathrm{d}y \tag{3.14}$$

Substitute this into the relation for the induced angle of attack:

$$\alpha_{\text{ind}} = \frac{1}{4\pi V_\infty} \int_{-b/2}^{b/2} \frac{\frac{\mathrm{d}\Gamma}{\mathrm{d}y}}{y_0 - y} \, \mathrm{d}y \tag{3.15}$$

At this point all parts of equation 3.9 given at the start of this section are defined in either known quantities of the free stream conditions, the wing design or the still unknown circulation. Now this equation is used to find the circulation. First substitute everything back into this equation:

$$\rho_\infty V_\infty \Gamma = \frac{1}{2} \rho_\infty V_\infty^2 c_{l_\alpha} \left(\alpha_g - \frac{1}{4\pi V_\infty} \int_{-b/2}^{b/2} \frac{\frac{\mathrm{d}\Gamma}{\mathrm{d}y}}{y_0 - y} \, \mathrm{d}y - \alpha_{l=0} \right) \tag{3.16}$$

This can be simplified to:

$$\alpha_g = \frac{2\Gamma}{c_{l_\alpha} V_\infty c} + \alpha_{l=0} + \frac{1}{4\pi V_\infty} \int_{-b/2}^{b/2} \frac{\frac{\mathrm{d}\Gamma}{\mathrm{d}y}}{y_0 - y} \, \mathrm{d}y \tag{3.17}$$

This equation is the *'fundamental equation of Prandtl's lifting-line theory'*. What it states is that the effective angle of attack together with the induced angle of attack is equal to the geometric angle of attack. This is also shown in Figure 3.1. The circulation is the only unknown in this equation and can therefore be solved for.

Lift and Drag Forces

When the circulation along the span is known the lift and drag coefficient can be calculated. First the lift distribution is given by the Kutta-Joukowski theorem:

$$l = \rho_\infty V_\infty \Gamma \tag{3.18}$$

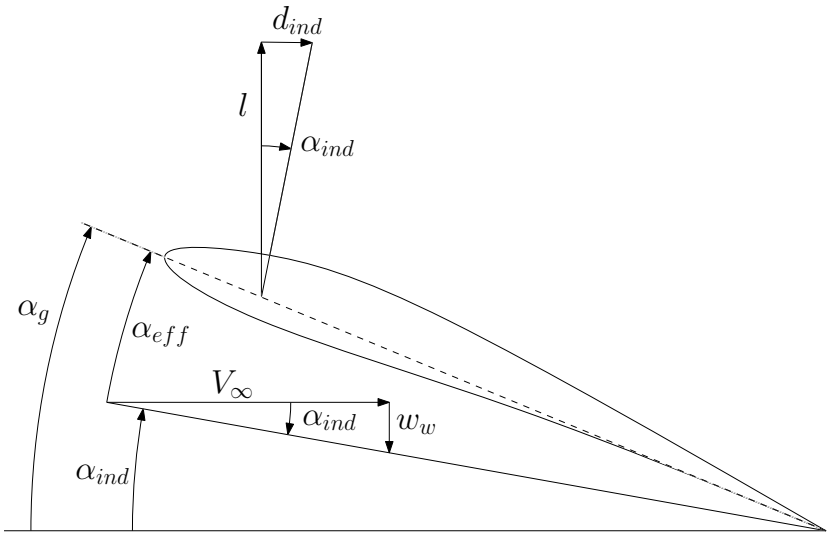

Figure 3.1: Definition of the angles of attack for a local airfoil in a finite wing.

Integrate this over the whole span:

$$L = \rho_\infty V_\infty \int_{-b/2}^{b/2} \Gamma \, \mathrm{d}y_0 \tag{3.19}$$

Following Figure 3.1 the induced drag is given by:

$$d_{ind} = l \frac{w_w}{V_\infty} = \rho_\infty \Gamma w_w \tag{3.20}$$

Substitute the relation for l and integrate this over the span:

$$D_{ind} = \rho_\infty \int_{-b/2}^{b/2} \Gamma w \, \mathrm{d}y_0 \tag{3.21}$$

The viscous drag is determined with strip theory. This means the profile drag of the local airfoil is estimated by performing a 2D analysis with XFOIL (15) at the local dynamic pressure, Reynolds number and lift coefficient.

$$d_{\text{visc}} = \frac{1}{2} \rho V_\infty^2 c_{d_{\text{visc}}} c \tag{3.22}$$

with

$$c_{d_{\text{visc}}} = f(Re, c_l) \tag{3.23}$$

The total drag is a summation of the induced and viscous drag.

3.2.2 Adapted Formulation to Account for Propeller–Induced Velocities

The Lifting Line is adapted to include the effects of the propeller-induced velocities on the wing. This model is called the Adapted LL. First the circulation distribution is derived, then the lift and drag forces are determined

Circulation Distribution

Consider the wing to be immersed in a propeller slipstream. In the slipstream the wing experiences additional velocities induced by the propeller. This is shown in Figure 3.2. Compared to the standard LL two propeller-induced velocities are added: the axial and downwash components u_p and w_p, respectively.

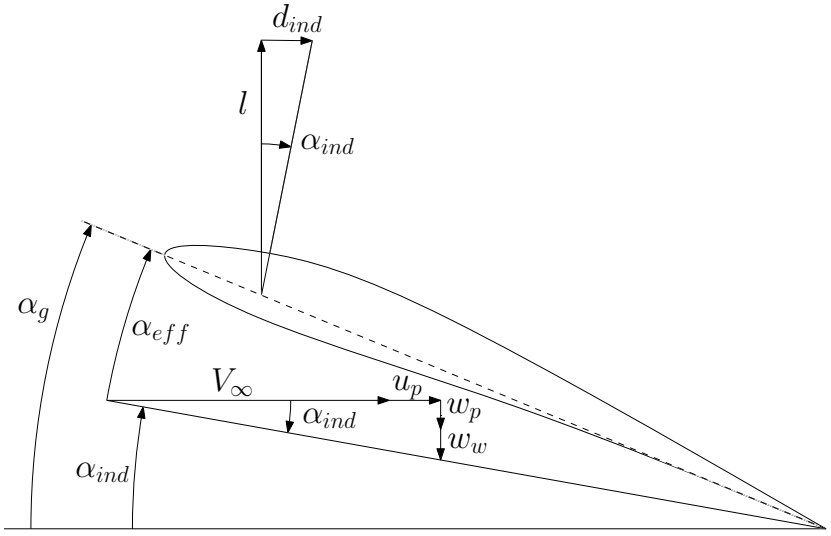

Figure 3.2: Definition of the angles of attack for a local airfoil in a finite wing immersed in a slipstream.

Based on the figure, the equation for the induced angle of attack needs to be updated (using the small angle assumption):

$$\alpha_{\text{ind}} = \tan^{-1}\left(\frac{w_w + w_p}{V_\infty + u_p}\right) \approx \frac{w_w + w_p}{V_\infty + u_p} \tag{3.24}$$

This changes the form of the *fundamental equation of Prandtl's Lifting Line theory* for the Adapted LL to:

$$\alpha_g = \frac{2\Gamma}{c_{l_\alpha} V_\infty c} + \alpha_{l=0} + \frac{1}{4\pi V_\infty} \int_{-b/2}^{b/2} \frac{\frac{\mathrm{d}\Gamma}{\mathrm{d}y}}{y_0 - y}\, \mathrm{d}y + \frac{w_p}{V_\infty + u_p} \tag{3.25}$$

This equation is very similar to Equation 3.17, for the standard LL. Only the last term is added to account for the propeller-induced velocities. Note that this derivation assumes the equation that relates lift and circulation does not change (Equation 3.18). This is the same assumption as made for the Adapted AN method and will be elaborated on in Section 3.3.2 and Appendix A.

Lift and Drag Forces

The local lift is still calculated with Equation 3.18 and the integral lift with Equation 3.19. The equations for the drag, however, are changed to:

$$d_{\text{ind}} = \rho_\infty \Gamma \left(w_w + w_p\right) \tag{3.26}$$

and

$$D_{\text{ind}} = \rho_\infty \int_{-b/2}^{b/2} \Gamma \left(w_w + w_p\right)\ \mathrm{d}y_0 \tag{3.27}$$

3.3 Vortex Lattice Method (VLM)

An adapted Vortex Lattice Method (Adapted VLM) is implemented to model the propeller–wing interaction based on the work of Veldhuis (3) and Alba (5). The starting point was a standard VLM code written in Matlab® : Tornado (13). The Adapted VLM model can be used in combination with different slipstream models (as will be explained in Section 3.5). Figure 3.3 shows the flow of the model with all and without any of the slipstream models active.

This section starts with a recap of the standard VLM model, followed by the changes made to the Adapted VLM model to include the effects of propeller-induced velocities.

3.3.1 Standard Formulation

In a VLM the wing is modelled by a number of panels placed on the surface or camber line of the wing. On every panel a horseshoe vortex is placed with its bound vortex on the quarter

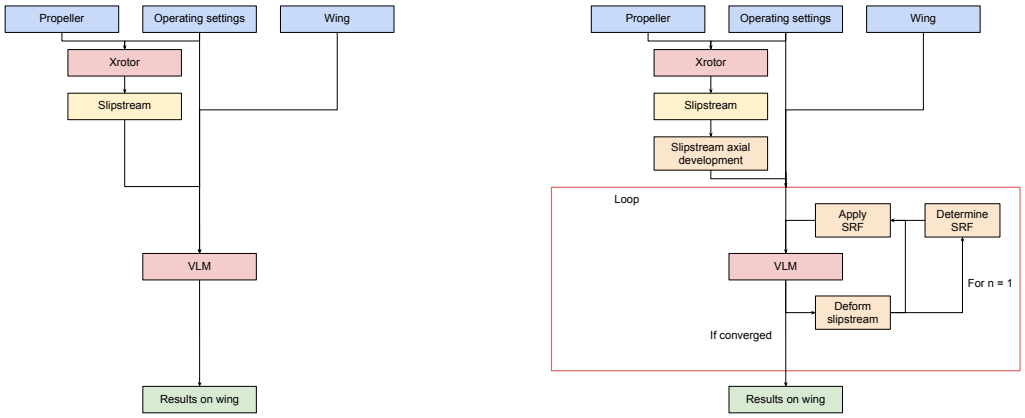

(a) No slipstream modelling

(b) With all slipstream models

Figure 3.3: Flowchart of the Adapted VLM model, shown for no slipstream modelling and with all slipstream models.

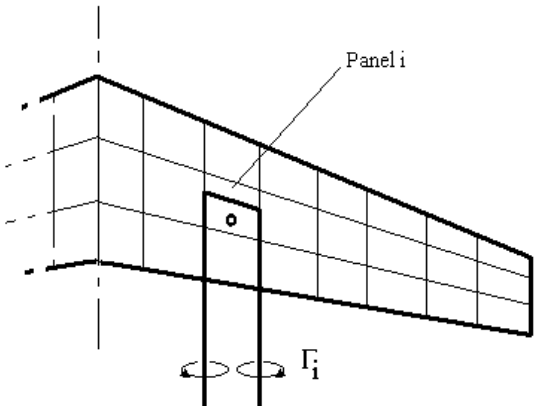

Figure 3.4: Example of a wing in a VLM modelled by panels with horseshoe vortices.

chord line,while the trailing vortices span from the bound vortex to infinitely downstream (in the direction of the chord). See Figure 3.4 for an example.

The vortices all produce a certain induced velocity on every other panel following the Biot-Savart Law:

$$\mathbf{dV} = \frac{\Gamma}{4\pi}\frac{\mathbf{dl}\times\mathbf{r}}{|\mathbf{r}|^3} \tag{3.28}$$

The strength of the vortex on every panel is such that the velocity normal to the panel is zero.

Thus, the wing induced velocities ($\mathbf{V}_{\text{wing}}$) counter the freestream velocity on every panel:

$$\mathbf{V} \cdot \mathbf{n} = (\mathbf{V}_\infty + \mathbf{V}_{\text{wing}}) \cdot \mathbf{n} = 0 \tag{3.29}$$

With this boundary condition the circulation can be calculated by solving the following equation.

$$\mathbf{AIC} \times \Gamma = -\mathbf{V}_\infty \cdot \mathbf{n} \tag{3.30}$$

The Aerodynamic Influence Coefficient (AIC) matrix is determined with the Biot-Savart law considering the strength of each vortex to be unity. The cross product of this matrix with the actual vortex strengths Γ results in the wing induced velocities $\mathbf{V}_{wing}$.

When the vortex strengths are known the force on the panel can be calculated with:

$$\mathbf{dF} = \rho\Gamma\mathbf{V} \times \mathbf{dl} \tag{3.31}$$

This is a vector interpretation of the Kutta-Joukowski theorem given by Phillips and Snyder (14). The result of this equation is a local force vector (in Newton per meter), which can be decomposed into the lift, induced drag and a spanwise force.

$$\mathrm{d}D_{\text{ind}} = \rho\Gamma\,(v\ \mathrm{d}z - w\ \mathrm{d}y) \tag{3.32}$$
$$\mathrm{d}F_y = \rho\Gamma\,(w\ \mathrm{d}x - u\ \mathrm{d}z) \tag{3.33}$$
$$\mathrm{d}L = \rho\Gamma\,(u\ \mathrm{d}y - v\ \mathrm{d}x) \tag{3.34}$$

When the vector **dl** only has a component in the y (spanwise) direction, implying that the wing has no taper, sweep or dihedral, then the equations reduce to the well known formulas for local lift and induced drag:

$$d_{\text{ind}} = \rho\Gamma w_w \tag{3.35}$$
$$l = \rho\Gamma\,(V_\infty + u_w) \tag{3.36}$$

The integral induced drag and lift are calculated by integrating the local values over the span

$$D_{\text{ind}} = \int_{-b/2}^{b/2} d_{\text{ind}}(y)\ \mathrm{d}y \qquad\qquad L = \int_{-b/2}^{b/2} l(y)\ \mathrm{d}y \tag{3.37}$$

The viscous drag is determined as is explained for the LL in Section 3.2.

3.3.2 Adapted Formulation to Account for Propeller–Induced Velocities

To account for the propeller slipstream velocities on the wing the VLM is adapted. The changes with respect to the standard VLM are highlighted in this section.

The velocity on the panels now includes the propeller induced velocities:

$$\mathbf{V} = \mathbf{V}_\infty + \mathbf{V}_{\text{wing}} + \mathbf{V}_{\text{prop}} \tag{3.38}$$

The strength of the vortices is determined by solving this equation:

$$\mathbf{AIC} \times \Gamma = -\left(\mathbf{V}_\infty + \mathbf{V}_{\text{prop}}\right) \cdot \mathbf{n} \tag{3.39}$$

With the vortex strengths known, the lift and drag forces can be calculated with Equation 3.31. For a wing with no taper, sweep and dihedral this results in the induced drag and lift fore:

$$d_{ind} = \rho\Gamma\left(w_w + w_p\right) \tag{3.40}$$

$$l = \rho\Gamma\left(V_\infty + u_w + u_p\right) \tag{3.41}$$

Note that the propeller induced velocities are included. For the local induced drag this formulation is fine, as will be shown in Section 4.2.2. However, for the local lift a better formulation is without the propeller induced velocity:

$$l = \rho\Gamma\left(V_\infty + u_w\right) \tag{3.42}$$

With this correction the lift distribution is predicted good as is shown in Section 4.2.1. Appendix A shows that without the correction the resulting lift distribution is wrong.

The equations for the integral lift and induced drag do not change compared to the standard VLM model. The viscous drag however, is changed to:

$$d_{\text{visc}} = \frac{1}{2}\rho V^2 c_{d_{\text{visc}}} c \tag{3.43}$$

where the velocity V is the local velocity (including the propeller-induced effects). For the lift and drag coefficients one change is made to the integral lift coefficient: it includes the propeller normal force coefficient as defined in Subsection 3.4.3.

3.4 Propeller Slipstream Modelling

The propeller-induced velocities needed as input for the Adapted LL and VLM are determined by a combination models. The far downstream values of the slipstream velocities are estimated with XROTOR (Subsection 3.4.1). Between the propeller plane and far downstream the slipstream undergoes a contraction and development of its axial velocity, which is described in Subsection 3.4.2. The slipstream is deflected by the wing upwash and downwash as modelled in Subsection 2.1.3. Finally, the tangential velocity in the slipstream decreases when the flow passes the wing. This is called swirl recovery and is described in Subsection 3.4.4.

3.4.1 Propeller–Induced Velocities from XROTOR

The propeller induced velocities are determined by what would be measured in the propeller slipstream. For the SIM model the slipstream is modelled as a straight cylinder with an axial and tangential velocity distribution over the radius. In axial direction they are kept constant. The velocity distributions are taken from the far field result of XROTOR. This means that this slipstream model assumes the the axial and tangential velocity are fully developed directly behind the propeller plane. Also no contraction of the slipstream is modelled.

XROTOR is an open source propeller analysis program developed by Drela (16). In XROTOR the potential formulation is used for all analysis, since this gives a good compromise between computational speed and accuracy. The potential formulation is based on the Goldstein method (18). The important aspects of this method are:

- The propeller is modelled with a system of horseshoe vortices of which the bound vortex is along the span of the propeller blade and the trailing vortices form a system with a straight vortex extending from the propeller axis and the other vortices forming a helical system around it (similar to a lifting line for wings).
- The flow is modelled as a potential flow, so any viscous and compressibility effects in the wake are neglected.
- No contraction of the slipstream is modelled.

3.4.2 Slipstream Axial Development and Contraction

The analysis with XROTOR results in the distribution of the axial and tangential velocities at a plane infinitely far downstream of the propeller. However, in the actual flow there is a certain development of the velocity distribution and contraction of the slipstream. The tangential velocity (or swirl) is assumed to be fully developed directly behind the propeller plane. The axial velocity develops following the model suggested by Conway (19) and implemented by Alba (5). The contraction of the slipstream is modelled based on an approach of Veldhuis (3).

Conway models the propeller and its slipstream as a combination of two vortex systems. One is a series of vortex rings which follow the outside slipstream surface. The second is a distribution of radial vorticity on the propeller plane, a surface distribution of vorticity on the slipstream surface and a trailing vortex extending from the propeller axis downstream. With these vortex systems the velocity field can be calculated. Based on an initial elliptical axial velocity distribution, the axial is given by (19):

$$V_x(r,x) = 2V_x(r,0) + V_{x_0}\left(-a + \frac{x}{R}\arcsin\left(\frac{2R}{\sqrt{x^2+(R+r)^2}+\sqrt{x^2+(R-r)^2}}\right)\right) \tag{3.44}$$

$$a = \sqrt{\frac{\sqrt{(R^2-r^2-x^2)^2+4R^2x^2}+R^2-r^2-x^2}{2R^2}} \tag{3.45}$$

with the velocity distribution at $x = 0$ being elliptical:

$$V_x(r,0) = \frac{V_{x_0}}{R}\sqrt{R^2-r^2} \tag{3.46}$$

The equation for the axial velocity is reformulated to produce a factor with which the resulting axial velocity from XROTOR can be multiplied. This is done by dividing the equation by the velocity distribution at the propeller plane $V_x(r,0)$.

$$f_{V_a} = \frac{V_x(r,x)}{V_x(r,0)} = 2 + \left(-a + \frac{x}{R}\arcsin\left(\frac{2R}{\sqrt{x^2+(R)^2}+\sqrt{x^2+(R)^2}}\right)\right) \tag{3.47}$$

Veldhuis models the propeller as an actuator disk with an uniform loading and uses the momentum theory to find the contraction ratio:

$$\frac{R_x}{R} = \sqrt{\frac{1+b}{1+b\left(1+\frac{x}{\sqrt{R^2+x^2}}\right)}} \tag{3.48}$$

$$b = \frac{1}{2}\left(-1+\sqrt{1+\frac{8}{\pi}T_c}\right) \tag{3.49}$$

With these models the velocity inside the slipstream is calculated as follows:

$$V_a(x,r) = (V_a)_{XROTOR}\left(x, r\frac{R}{R_x}\right) \cdot f_{V_a}\left(x, r\frac{R}{R_x}\right) \tag{3.50}$$

$$V_t(x,r) = (V_t)_{XROTOR}\left(x, r\frac{R}{R_x}\right) \tag{3.51}$$

3.4.3 Slipstream Deflection

A propeller placed at an angle of attack with respect to the freestream produces a normal force and deflects the slipstream. The implementation of this model in this thesis is adopted from Alba (5), who based it on the equations suggested by De Young (20).

The slope of the normal force with respect to the angle of attack is approximated by:

$$\frac{dC_N}{d\alpha_p} = \frac{4.25\sigma_e}{1+2\sigma_e} \cdot \sin(\beta_0+3) \cdot f \cdot \frac{\pi J^2}{8} \tag{3.52}$$

$$\sigma_e = \frac{4B}{3\pi} \cdot \frac{c_{av}}{2R} \cdot \frac{C_{l_{\alpha_{av}}}}{0.95 \cdot 2\pi} \tag{3.53}$$

$$f = 1 + 0.5 \cdot \left(\sqrt{1+T_C}-1\right) + \frac{T_C}{4(2+T_C)} \tag{3.54}$$

$$T_C = \frac{8}{\pi J^2} C_T \tag{3.55}$$

And for the slope of the deflection of the slipstream with respect to the angle of attack:

$$\frac{d\theta_S}{d\alpha_p} = \frac{1+T_C-\sqrt{1+T_C}}{2+T_C} + \frac{3+2T_C+\sqrt{1+T_C}}{(2+T_C)^2} \cdot \frac{\sqrt{1+T_C}}{4} \cdot \left[\frac{dC_N}{d\alpha_p}\right]_{T_C=0} \cdot \frac{8}{\pi J^2} \tag{3.56}$$

The normal force and slipstream deflection are now calculated based on the angle of attack of the propeller plus the angle due to the upwash of the wing:

$$C_N = \frac{dC_N}{d\alpha_p}\left(\alpha_p + \arctan\left(\frac{w}{V_\infty}\right)\right) \tag{3.57}$$

$$\theta_{S_{prop}} = \frac{d\theta_S}{d\alpha_p}\left(\alpha_p + \arctan\left(\frac{w}{V_\infty}\right)\right) \tag{3.58}$$

The normal force created by the propeller is also part the complete propeller–wing combination and is therefore added to the lift coefficient of the wing as follows:

$$C_L = C_{L_{wing}} + 2C_N = \frac{2 \cdot (L + 2N)}{\rho V_\infty^2 S} \tag{3.59}$$

Downstream of the propeller, the flow around the wing deflects the slipstream even more. In front of the wing, the upwash deflects the slipstream upwards and behind the quarter chord the downwash deflects the slipstream downwards:

$$\theta_{S_{\text{front}}} = \theta_{S_{\text{prop}}} + \arctan\left(\frac{\bar{w}_{\text{front}}}{V_\infty}\right) \tag{3.60}$$

$$\theta_{S_{\text{rear}}} = \theta_{S_{\text{prop}}} + \arctan\left(\frac{\bar{w}_{\text{rear}}}{V_\infty}\right) \tag{3.61}$$

Here $\bar{w}_1$ and $\bar{w}_2$ are the average upwash and downwash on the sections in upstream of the quarter chord point on the wing and downstream of this point, respectively. The downwash value is found by first taking the average over the cross-section of the slipstream at a certain axial location downstream of the propeller plane. Then the average is taken over the values along the section in flow direction.

3.4.4 Swirl Recovery

The wing recover part of the swirl velocity. On the wing this is noticed by the local reduction of the induced drag. In the slipstream the swirl (or tangential) velocity is reduced. Therefore, the wing does not experience the full tangential component of the propeller-induced velocity. This velocity needs to be corrected. In literature both Veldhuis (3) and Alba (5) use a swirl recovery factor (SRF) to do this. As is in Section 4.2.1 and Appendix B the application of the swirl recovery factor is necessary to achieve good agreement with experimental results.

Veldhuis uses a constant factor of 0.5 (3), while Alba determines a swirl recovery factor dependent on the specific situation(5). Both the approach of Veldhuis as well as of Alba are implemented in the Adapted VLM model in this thesis. The method of Alba works as follows.

The amount of swirl energy, which is the kinetic rotational energy, in a cross section of the slipstream behind the propeller plane can be calculated with Equation 3.62.

$$E_K = \int_{r_{hub}}^{r_{tip}} \pi \rho V_t^2 r dr \tag{3.62}$$

When a wing is present, the swirl energy decays downstream of the propeller plane. The wing induces velocities on top of the slipstream velocities, which reduces the amount of swirl energy present. A measure of this decay is determined by calculating the decay of the swirl energy with the VLM model without the effect of the swirl recovery factor. The decay with respect to the swirl energy directly behind the propeller plane is calculated in axial direction from the propeller plane to the wing trailing edge. Finally the mean value of the decay over this range is taken as the swirl recovery factor.

Two remarks can be made on this method. One, the swirl recovery factor is not determined based on the physical flow phenomena. Actually it is more a trick that is applied and observed be necessary and to work well (that is the reason why it is implemented). It is therefore an indication that not all flow phenomena are completely modelled by the adapted VLM model. However, with respect to the constant SRF of Veldhuis this method has the advantage that it depends on the wing design, which is a benefit when doing an optimisation.

Two, the swirl recovery factor is applied to the whole cross section of the slipstream at once. Differences between the swirl recovery of the inboard wing compared to the outboard part might not be modelled correctly. This might introduce errors in the optimum design of the wing.

3.5 Overview and Naming of Numerical Models

This section introduces a naming convention in order to keep track of the different numerical models introduced in this chapter. In this chapter a number of numerical models are introduced, this section serves as an overview of these models and by what name they are referenced. These models are divided into two categories: models to analyse the wing and models for the slipstream velocities.

In Table 3.1 the models used for the analysis of the wing are shown. The AN model does not actually analyse the wing, but it does provide the optimal lift distribution on the wing, which is why it is put in this category. As is clear from the table 'Adapted' is used to describe when the model is adapted to include the effects of propeller-induced velocities.

Table 3.2 defines the names for propeller slipstream models. The first model, SI, are the slipstream velocities far downstream of the propeller as predicted by XROTOR (Subsection 3.4.1). Model SII uses the slipstream velocity results from XROTOR and then corrects these values for the finite distance of the wing behind the propeller. This is done by applying the

Table 3.1: Names for the numerical models for the analysis of the wing.

Name	Description of the model
AN	Analytic solution of the optimal lift distribution for minimum induced drag (Subsection 3.1).
Adapted AN	AN, adapted to include the effect of propeller-induced velocities (Subsection 3.1).
LL	Lifting Line (Subsection 3.2.1).
Adapted LL	LL, adapted to include the effect of propeller-induced velocities (Subsection 3.2.2).
VLM	Vortex Lattice Method (Subsection 3.3.1).
Adapted VLM	VLM, adapted to include the effect of propeller-induced velocities (Subsection 3.3.2).

slipstream contraction and axial development of the slipstream as described in Subsection 3.4.2. The next model, SIII, is the same as model SII with the addition of a prescribed (and constant) SRF for the tangential velocities in the slipstream. Model SIV is also based on model SII but now with a design based SRF. The use and determination of the SRF is described in Subsection 3.4.4. The last model, SV, is based on model SIV with the addition of modelling the slipstream deflection as described in Subsection 3.4.3.

Table 3.2: Names for the propeller slipstream models.

	Model name				
Model description	**SI**	**SII**	**SIII**	**SIV**	**SV**
Velocities directly from XROTOR (Subsection 3.4.1)	✓	-	-	-	-
Slipstream contraction (Subsection 3.4.2)	-	✓	✓	✓	✓
Axial development of the slipstream (Subsection 3.4.2)	-	✓	✓	✓	✓
Prescribed SRF (Subsection 3.4.4)	-	-	✓	-	-
Design based SRF (Subsection 3.4.4)	-	-	-	✓	✓
Slipstream deflection (Subsection 3.4.3)	-	-	-	-	✓

The adapted versions of the numerical models for the wing analysis always require a propeller slipstream model to provide the propeller-induced velocities. To indicate which model is used the name of the propeller slipstream model is simply added to the wing analysis model. For example, VLM-SV indicates the Adapted VLM is combined with propeller slipstream model SV. Note that combining VLM with SV indicates the Adapted VLM is used (instead of VLM) so the word 'Adapted' can be dropped. In the remainder of this thesis, the following combinations of wing analysis and propeller slipstream models are used (unless otherwise stated):

- Adapted AN is in fact AN-SI
- Adapted LL is used for LL-SIII

- Adapted VLM is used for VLM-SV

Note that different propeller slipstream models are used for the different wing analysis models. For the Adapted AN, this is because any slipstream modelling would go against the assumptions made by the author of the model (see Subsection 3.1). The Adapted LL uses the most advanced propeller slipstream model currently implemented (which is SIII). For the Adapted VLM the most advanced model is SV, which is therefore used by default. There is no inherent constraint to implement model SIV and SV for the Adapted LL, however this was not done due to time constraints.

3.6 Analysis of the Numerical Model Execution Time

For the use of a numerical model for optimisation short execution times are very important. This section analyses these times for the numerical models used in this thesis. Besides the numerical models used in this thesis, also the results for AVL are added for reference. The analysis is performed for a wing with 100x5 (spanwise x chordwise) panels. The AN and LL models do not use chordwise panels so they actually model a wing with 100x1 panels. The AVL program analyses the wing in isolated configuration, while the other methods analyse the wing immersed in a propeller slipstream.

Table 3.3 shows a summary of the typical execution times. All models have execution times in the order of seconds or less, which means they are fast with respect to higher-order methods like computational fluid dynamics (which has execution times in the order of hours). This is a strong benefit since for optimisation requires to make a large number of iterations.

Table 3.3: Typical execution time for the numerical methods used in this thesis to perform an analysis of a wing with 100x5 (spanwise x chordwise) panels. The computer used is a MacBook Air (13-inch, Mid 2013) with a 1.3 GHz Intel Core i5-4250U processor. The column 'w.r.t. AVL' is the execution time divided by the execution time of AVL.

Method	Execution time	w.r.t. AVL
AVL	1.81 sec	1
AN-SI	0.04 sec	0.02
LL-SI	0.07 sec	0.04
LL-SII	0.07 sec	0.04
LL-SIII	0.08 sec	0.04
VLM-SI	8.7 sec	4.8
VLM-SII	8.7 sec	4.8
VLM-SIII	8.5 sec	4.7
VLM-SIV	16.4 sec	9.0
VLM-SV	25.8 sec	14.3

Between the numerical models large differences in speed are recognisable. The AN-SI method is by far the fastest, which is because it is an analytical solution. However, this method only gives a lift distribution as a result and not the corresponding design of the wing that would satisfy this lift distribution. Just a fraction slower are the models LL-SI to LL-SIII. The benefit with respect to AN is that it is based on the actual wing design. This means that using the models LL-SI to LL-SIII for optimisation results in the optimal wing design, in contrast to only the optimal lift distribution of AN. The downside is, it needs a number of iterations for the optimisation while the AN model is run only once. The slowest are the models VLM-SI to VLM-SV. These models use a larger number of panels with respect to the Adapted LL models since they also divide the wing into panels in chordwise direction. The result is that a much larger system of equations need to be solved, which significantly more time.

Within the models VLM-SI to VLM-SV strong differences are found, VLM-SI to VLM-SIII are approximately as fast as each other, while VLM-SIV takes twice and VLM-SV 3 times as long. The difference is speed between these models is due to the number of iterations are performed within the model. VLM-SI to VLM-SIII are run once, while the design based SRF of VLM-SIV needs two to run two times. VLM-SV needs to iterate because of the slipstream deflection model. Usually this is done in 3 runs, but more iterations are sometimes needed.

In terms of optimisation speed the model LL-SIII is the preferred, it provides the analysis of the wing design, is are fast and uses the most advanced propeller slipstream model that is available (without compromising on speed). The AN model could be used in combination with the model LL-SIII to optimise for a matching the lift distribution between the lift on the wing and the optimal lift distribution for minimum induced drag. This would be useful only when optimisation for lift matching is faster than optimising for minimum induced. For the models VLM-SIII, VLM-SIV or VLM-SV the downside is their slower execution times. However, they might make up with their more advanced modelling of the propeller slipstream and wing (with respect to the LL-SIII). Chapter 4 shows that the VLM-SV model indeed makes a better prediction of the lift distribution compared to LL-SIII. This means choosing the model for optimisation is a compromise between accuracy and speed.

Chapter 4

Validation of Adapted Numerical Models

The correct implementation of the numerical models Adapted LL, Adapted VLM and XROTOR is validated in this chapter. The Adapted LL and VLM are validated using the analytic solution for an isolated elliptical wing in Section 4.1. The lift and drag predictions by the Adapted LL and VLM are compared with existing experimental results in Section 4.2. Finally, the prediction capability of XROTOR in terms of thrust and torque are validated with another set of existing experimental data in Section 4.3.

4.1 Verification of Adapted LL and VLM with an Isolated Elliptical Wing

The correct implementation of the Adapted LL and VLM was first verified with the results for an isolated elliptical wing. The results for the lift and induced drag were compared with the analytic solution and another VLM code (Athena Vortex Lattice (AVL) developed by Youngren and Drela (21)). The analytic solution is given by the Adapted AN model.

Figure 4.1 shows the lift distribution on an isolated elliptical wing. The expected elliptical lift distribution was found, with excellent agreement between the Adapted VLM model, AVL code and analytic solution. The total lift and total induced drag is shown in Figure 4.2. Good agreement is found for the Adapted VLM model with the AVL code and analytic solution. This verifies the Adapted VLM model is implemented correctly for isolated wings (without the effect of the propeller-induced velocities).

The Adapted LL shows a slight overprediction of the lift distribution and integral lift, the agreement with for the integral induced drag with the other models and analytic solution is good. This shows that the Adapted LL is correctly implemented.

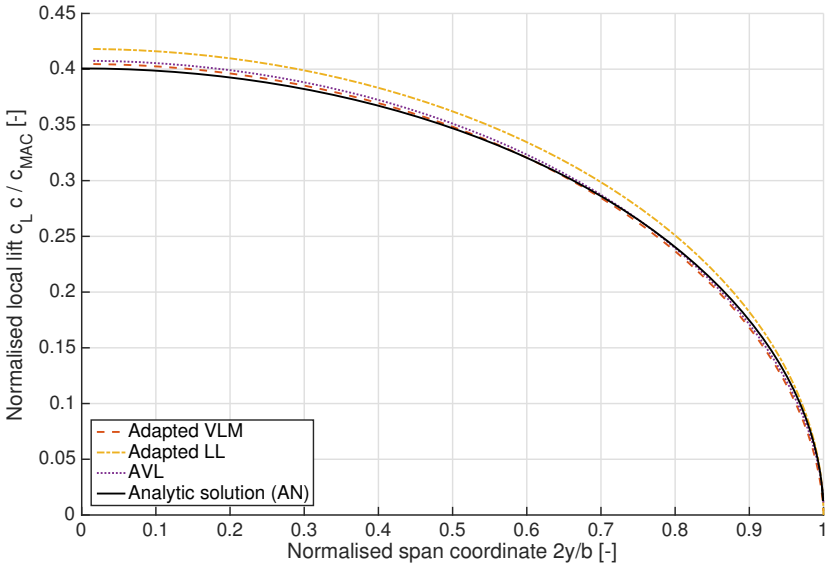

Figure 4.1: Comparison of the adapted VLM code with AVL on the normalized lift distribution of an isolated elliptical wing ($\alpha = 4$ deg, $M = 0.15$).

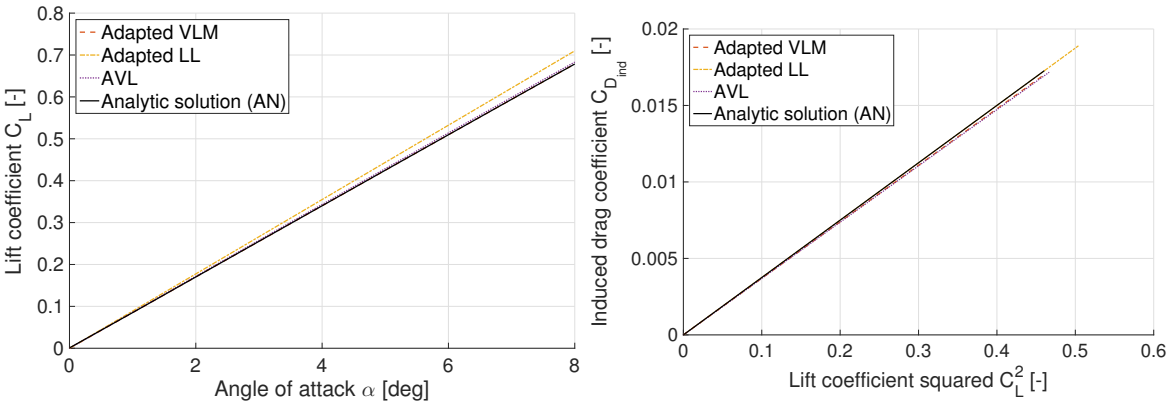

(a) Lift vs angle of attack

(b) Induced drag vs lift squared

Figure 4.2: Comparison of the adapted VLM code with AVL on the total lift and induced drag for an isolated elliptical wing. On the left the total lift coefficient versus angle of attack is shown and on the right the total induced drag versus the lift squared. ($M = 0.15$)

4.2 Validation of Adapted LL and VLM with Existing Experimental Data

The Adapted LL and VLM are validated by comparing the results with existing experimental results from a wind tunnel test on the model PROWIM (3). This experiment consisted of a wing with a wing mounted propeller in tractor configuration and was tested in the Low Turbulence Tunnel (LTT) of the Delft University of Technology. The experimental results shown here are from pressure taps in the wing surface and from balance measurements. The

operating conditions during the experiment are summarised in Table 4.1. The propeller was rotating inboard up for the results used in this section. For more details on the experimental setup the reader is referred to the (3).

Table 4.1: Operating conditions for the experiment with the PROWIM model by Veldhuis (3).

Parameter	Symbol	Value
Freestream velocity	V_∞	50 m/s
Wing angle of attack	α	0,2,4...10 deg
Propeller blade angle (at $r/R = 0.75$)	$\beta_{0.75}$	25 deg
Propeller advance ratio	J	0.85
Propeller thrust coefficient	T_c	0.168

The experimental results on the propeller wing model PROWIM are used to validate the Adapted LL and VLM for the propeller–wing interaction effects on the lift and induced drag.

4.2.1 Lift

The integral lift results from the Adapted LL and VLM models are compared with the experimental results in Figure 4.3. For the propeller-off case (in Figure 4.3(a)) good agreement is found between the experimental results and the Adapted VLM. The Adapted LL, however, overpredicts the lift, especially at higher angles of attack. This might correlate with the overprediction of lift found in Section 4.1.

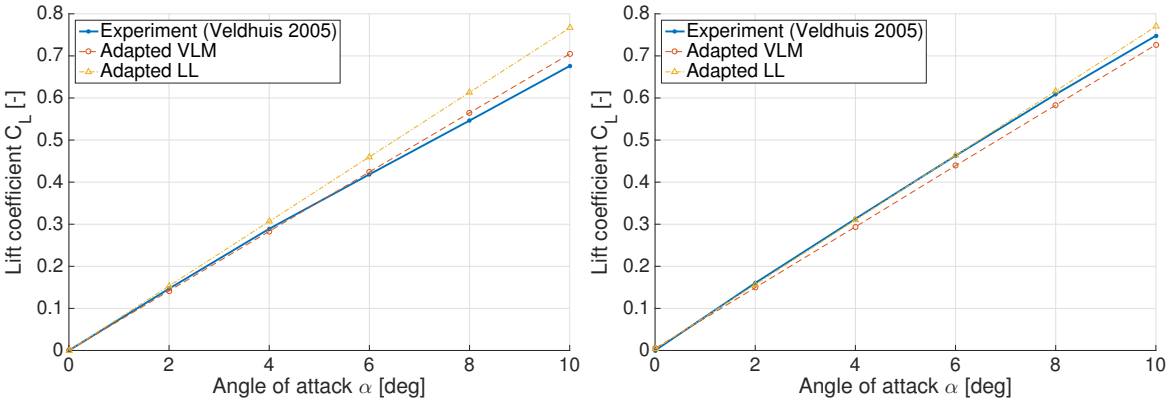

(a) Propeller-off

(b) Propeller-on

Figure 4.3: Integral lift versus angle of attack of PROWIM for the cases propeller-off and propeller-on. The experimental results are from Veldhuis (3).

Figure 4.3(b) shows the lift versus angle of attack for the propeller-on case. Although the Adapted VLM slightly underpredicts the lift, the agreement of both numerical models with the experimental results is good. This validates the prediction of integral lift for both the Adapted LL and Adapted VLM.

The lift distribution is also important to validate, since in these results the effects of propeller–wing interaction are really visible. Figure 4.4 shows the lift distribution for two angles of attack. As can be seen both the Adapted LL and VLM display the main flow effects of propeller wing interaction. The lift directly behind the upgoing blade is increased. Behind the downgoing blade the lift decreases. Outside of the slipstream the lift is also changed. Inboard of the upgoing blade the lift is increased due to the upwash caused by the gradient in the local lift. In a similar manner, the lift on the outboard wing decreases.

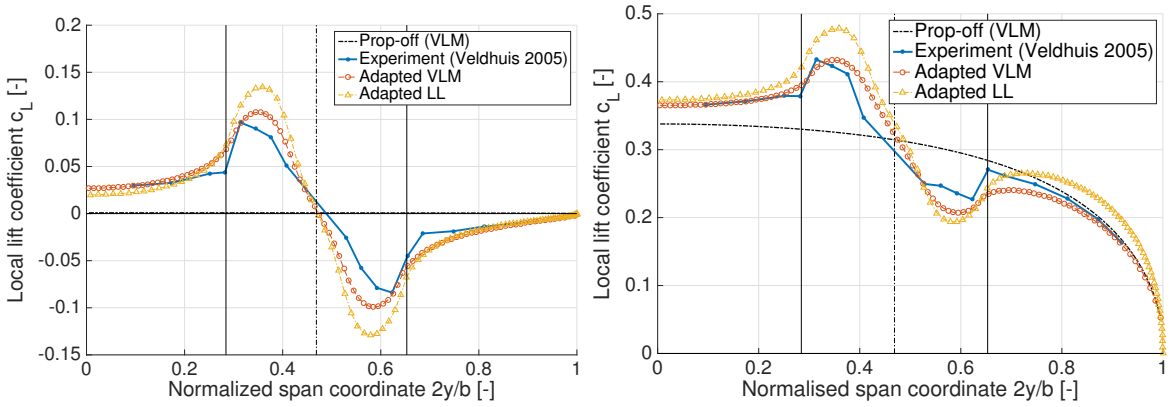

(a) $\alpha = 0$ deg

(b) $\alpha = 4$ deg

Figure 4.4: Lift distribution on PROWIM model with propeller rotating inboard up for angle of attack $\alpha = 0$ and $\alpha = 4$ degrees. The experimental results are from Veldhuis (3). Note that the propeller location is represented by the vertical black lines.

It is also clear from the Figure 4.4 that the Adapted VLM makes a better prediction of the lift distribution with respect to the Adapted LL. This is because the Adapted VLM employs a more advanced slipstream model (see Section 3.5) than the Adapted LL. The effects of the specific slipstream models on the lift distribution results is investigated in Appendix B. Both the Adapted LL and VLM use the correction for the lift equation mentioned in Subsection 3.3.2. Without the correction there would be no agreement with the experimental results at all, as is shown in Appendix A. This shows the correction is indeed needed. The same is true for the swirl recovery factor, as is shown in Appendix B.

From these results it can be concluded that the Adapted VLM is validated for predicting the integral lift and lift distribution. Although the Adapted LL does not accurately predict the lift distribution, it does show the correct propeller–wing interaction effects. This might be a useful benefit since its execution time is faster than that of the Adapted VLM.

4.2.2 Induced Drag

Since the balance measurements provide a summation of the thrust of the propeller, the drag of the nacelle, and the combination of profile and induced drag of the wing, the induced drag cannot be extracted directly from the experimental balance data. Although a quantitative

wake analysis is also performed by Veldhuis (3) and could be used to separate the drag components, this approach breaks down for the propeller-on case, since it only provides the forces generated by the whole system, i.e. the propeller–wing combination. Therefore, a different approach is used to validate the Adapted LL and VLM for the induced drag prediction. The induced drag component was approximated by assuming a parabolic drag relation between the induced drag and lift:

$$C_{D_{\mathbf{ind}}} \approx C_{D_{\mathbf{tot}}} - C_{D_0} = \frac{C_L^2}{\pi A e} \tag{4.1}$$

Figure 4.5 shows the approximated induced drag versus the lift squared. As can be seen for the propeller-off case in Figure 4.5(a) the linear trend indicates the parabolic drag assumption is reasonable. Both the Adapted LL and VLM slightly underpredict the approximated induced drag. This is expected to be caused by the presence of the nacelle. The nacelle causes an increase in the drag with respect to a clean wing. Since the nacelle will create some lift when increasing the angle of attack, the drag also increases. The nacelle is not modelled with the Adapted LL and VLM and is therefore the likely cause of this underprediction of the induced drag.

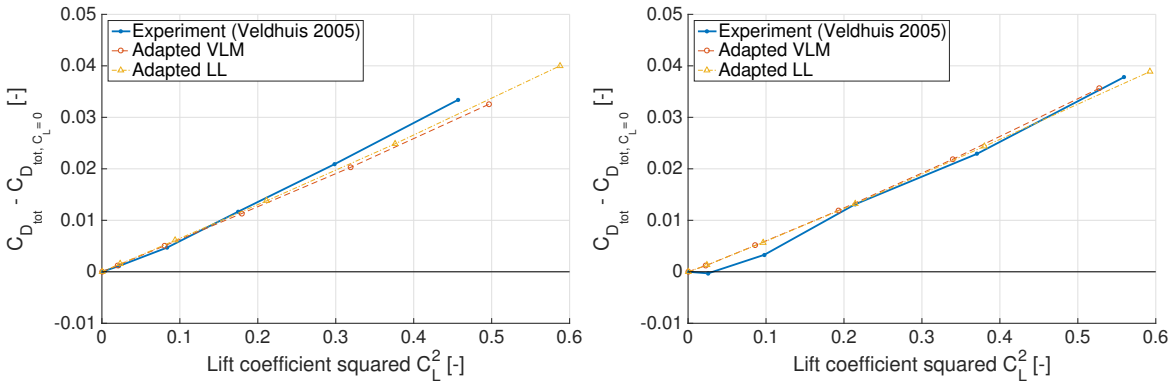

(a) Propeller-off

(b) Propeller-in

Figure 4.5: Approximated induced drag ($C_{D_{\mathbf{ind}}} \approx C_{D_{\mathbf{tot}}} - C_{D_0}$) versus lift squared for the propeller-off and propeller-on cases. The experimental results are from Veldhuis (3).

For the propeller-on case (in Figure 4.5(b)) the agreement of both models with the experimental results is good at higher lift. For lower lift the approximated induced drag results from the experiment show a deviation from the parabolic drag assumption. This is not observed in the results of the Adapted VLM and LL. However, in general both the Adatped LL and VLM models show good agreement with the approximated induced drag results from experimental data. This means the integral drag increase with increase in lift is modelled correctly. No conclusion can be made about the prediction of the absolute induced drag values.

The distribution of induced drag cannot be validated with experimental data, since this data is not available. Therefore, the distribution of induced drag results from the numerical models

is studied on itself. Figure 4.6 shows the induced drag distribution for two angles of attack. As can be seen for $\alpha = 0$ in Figure 4.6(a) the induced drag is negative in both the regions of propeller-induced upwash and downwash. This behaviour can be explained as follows: recall from Section 2.1.1 that the upwash induced by the propeller the lift vector is pointed more forward and therefore reduces the induced drag. The wing in this situation is at $\alpha = 0$ deg which means the upwash causes the lift vector to actually point forward, which causes a negative induced drag. The downwash, combined with a negative lift vector also causes a negative induced drag. In Figure 4.6(b) the wing is at $\alpha = 4$. A negative induced drag in the propeller-induced upwash region is still observed, which indicates a strong upwash velocity is present. The induced drag in the downwash region is positive since the lift is now also positive on this wing section. The differences between the Adapted LL and Adapted VLM observed in Figure 4.6(b) correspond to the differences in lift distribution predicted by the two models.

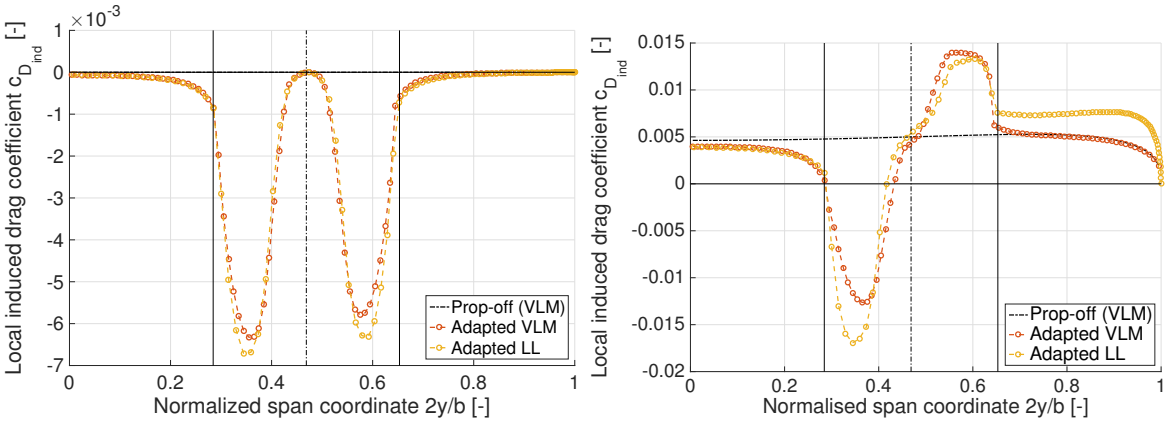

(a) $\alpha = 0$ deg

(b) $\alpha = 4$ deg

Figure 4.6: Induced drag distribution on PROWIM model with inboard-up rotating propeller for an angle of attack $\alpha = 0$ and $\alpha = 4$ degrees. The experimental results are from Veldhuis (3).

The effects found for the induced drag distribution are what is expected from the propeller–wing interaction and therefore the Adapted LL and VLM models are considered to be correctly implemented when the induced drag distribution is considered.

4.3 Validation of XROTOR with Existing Experimental Data for Propeller Thrust and Torque

The propeller thrust and torque predicted by XROTOR are compared with existing experimental data (22). Figure 4.7 shows the thrust and torque coefficient versus advance ratio of the N250 propeller with different blade pitch settings. As can be seen the results from XROTOR are in general in good agreement with the experimental results. For high thrust/torque coefficients and low advance ratios the onset of flow separation on the blades cause the results of XROTOR to diverge from the experimental data.

The N250 propeller is used in the wind tunnel experiment (as described in Chapter 5). In Figure 4.7, the operating point of the propeller in this experiment is indicated with a red circle. Although this operating point is close to the region where the onset of flow separation affects the propeller thrust and power, the predictions by XROTOR are still good.

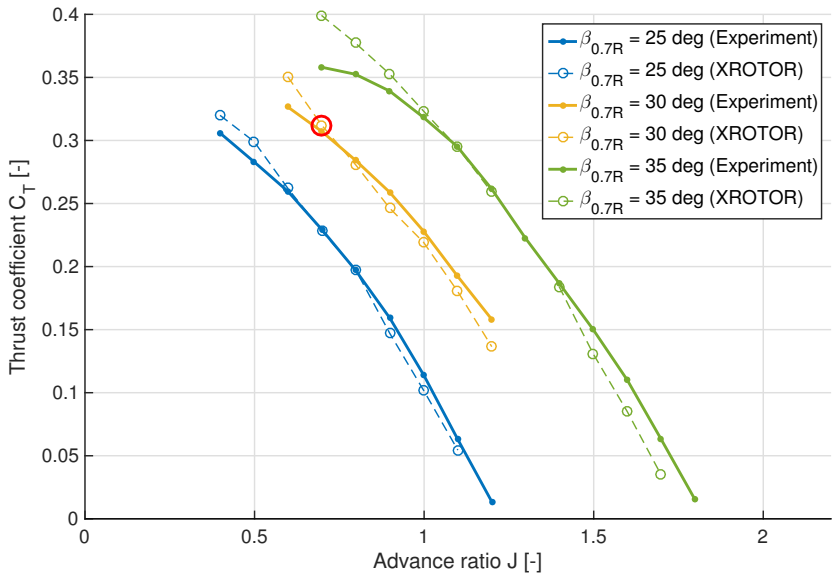

(a) Thrust

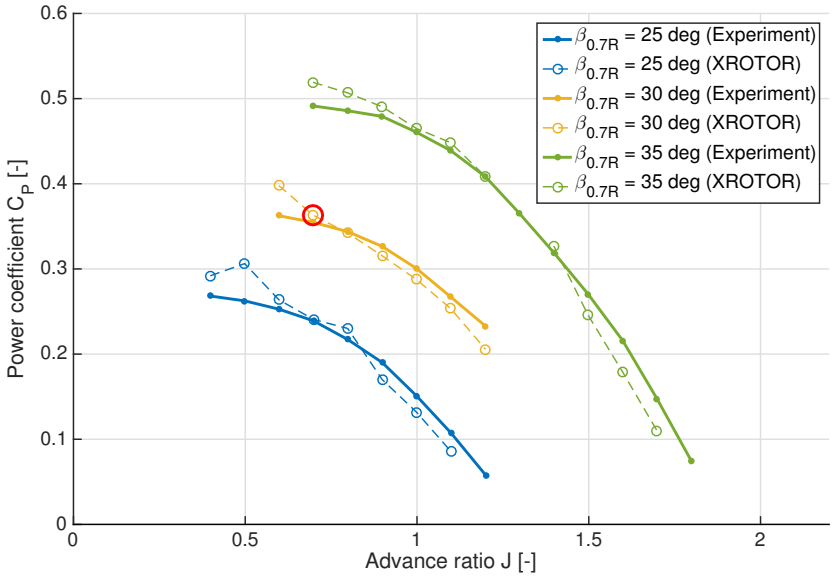

(b) Torque

Figure 4.7: Thrust and torque coefficient versus advance ratio of the N250 propeller with different blade pitch settings, comparing results of XROTOR with experimental data (22). The red circle indicates the operating point of the propeller in the wind tunnel experiment (see Section 5.3).

Chapter 5

Experimental Setup, Measurement Techniques and Data Post-Processing

A wind tunnel experiment was performed in order to validate the change in lift distribution on the wing due to a change in wing twist distribution. Two different wings were tested in a propeller tractor configuration. Both wings are half models, so a wall is used as a symmetry plane. Figure 5.1 shows an overview of the setup. The experiment was performed in the Open Jet Facility (OJF) of Delft University of Technology.

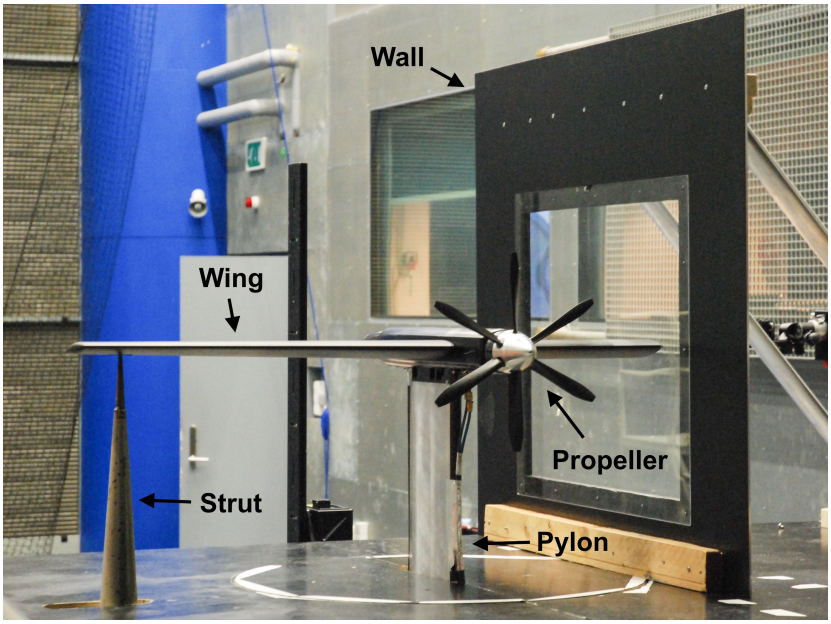

Figure 5.1: Overview of the wind tunnel experimental setup.

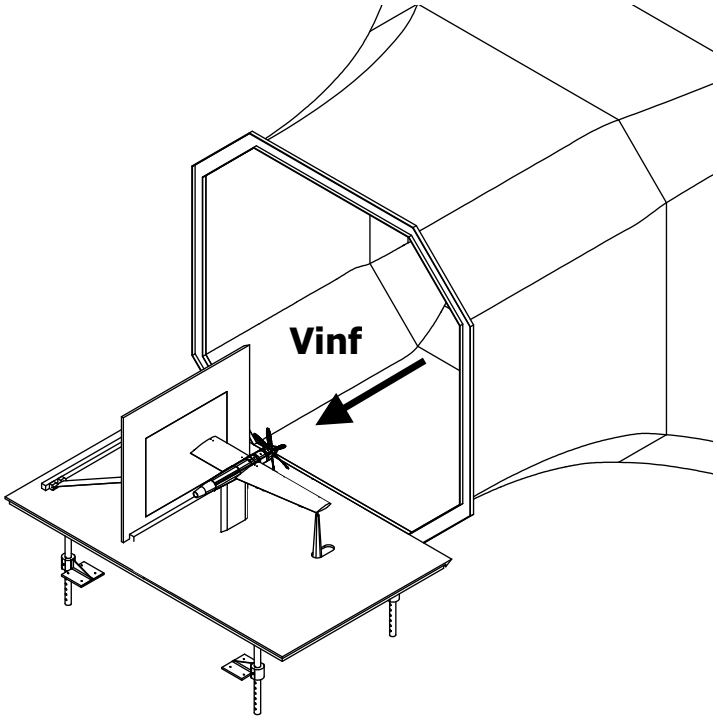

(a) Isometric view

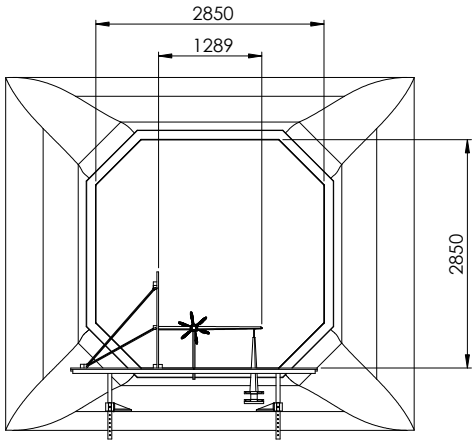

(b) Rear view

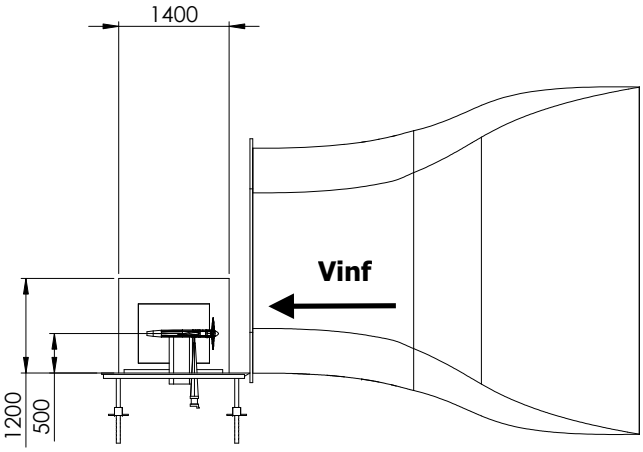

(c) Side view

Figure 5.2: Overview of the wind tunnel experimental setup. Dimensions are in mm.

5.1 Wind Tunnel Facility

The measurements were performed in the Open Jet Facility (OJF). This is a closed circuit wind tunnel with an open test section. The octagonal cross-section of the jet measures

2.85x2.85m and can reach speeds up to 30 m/s. The test section is 6.0 m wide, 6.5 m high and 13.5 m long. A schematic overview of the OJF is given in Figure 5.3.

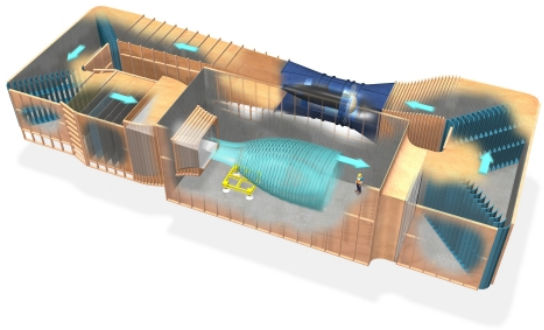

Figure 5.3: Sketch of the Open Jet Facility (OJF) at Delft University of Technology (23) .

5.2 Models

An overview of the models used in the wind tunnel experiment is shown in Figure 5.4. The setup of the experiment starts with the N250 propeller mounted on a pylon. The inboard wing is supported by the pylon (or nacelle) and the wall. The outboard wing is supported by the pylon and strut. Both the inboard and outboard wing have the freedom to rotate such that the angle of attack can be changed. The N250 propeller, wings and wall are discussed in more detail in the following subsections.

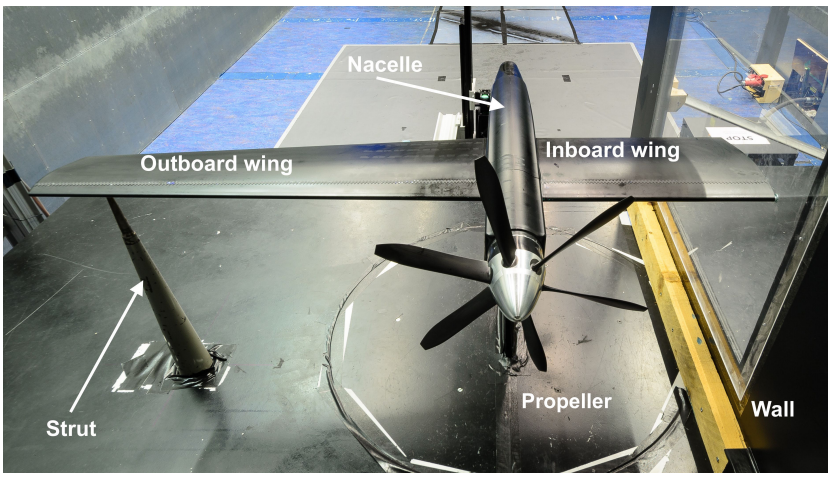

Figure 5.4: Overview of models used in wind tunnel experiment. Two sets of inboard and outboard wings are used: Control wing and Modified wing.

5.2.1 N250 Propeller

The N250 propeller was used for the wind tunnel experiment. A close up of the propeller is depicted in Figure 5.5 and the specifications of the propeller are given in Table 5.1. Figure 5.6 shows the chord and twist distribution and 4 airfoil shapes used along the blade.

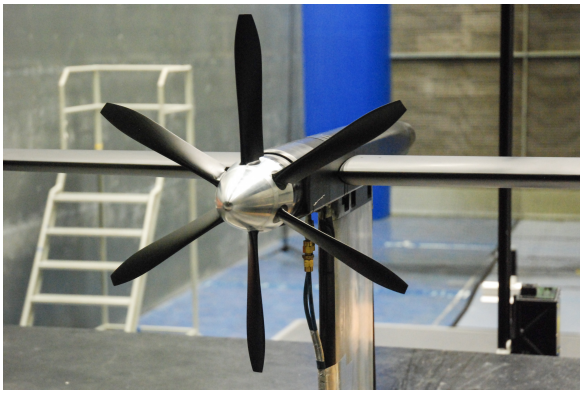

Figure 5.5: Close up of the N250 propeller.

Table 5.1: Summary of the N250 propeller specifications.

Parameter	Symbol	Value	Unit
Number of blades	B	6	-
Diameter	D	0.406	m
Hub diameter	D_{hub}	0.084	m
Blade angle at $r/R = 0.7$	$\beta_{0.7}$	30	deg

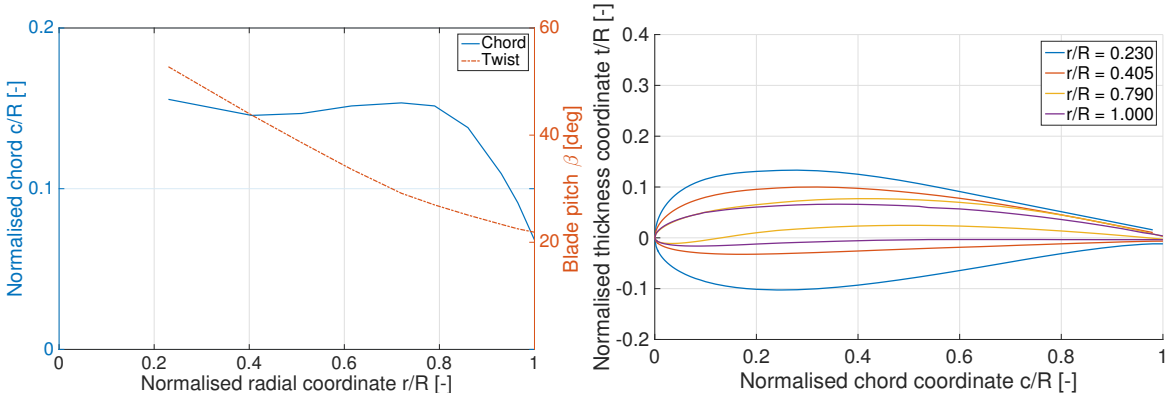

(a) Chord and twist distribution

(b) Airfoil shapes

Figure 5.6: Chord and twist distribution of the N250 propeller and the airfoil shape at 4 radial positions along the blade. The airfoils are shown with zero blade pitch angle.

The propeller is powered by a pneumatic motor with the compressed air supplied by the central air supply of the High Speed Wind Tunnel Laboratory at the Delft University of

Technology. The propeller is mounted on a nacelle which houses the pneumatic motor. The nacelle is connected to a vertical pylon. The propeller setup also contains a rotating shaft balance, which was not operational at the time of the measurement.

5.2.2 Control and Modified Wing

Two wings were tested in the wind tunnel: the *Control wing* and the *Modified wing*. The wings have the same symmetric airfoil (NACA 64_2-015A), span and chord distribution (see Figure 5.7).

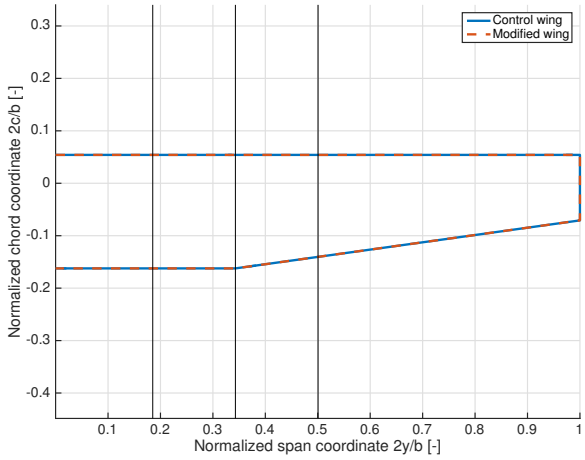

Figure 5.7: Planform of the Control and Modified wings in top view.

Both wings consist of an inboard and an outboard part. The inboard part is mounted on the wall and the nacelle of the propeller. The outboard part is mounted on the nacelle and a strut. All supports connect to the wing at the axis 23 % of the root chord (same axis around which the twist is applied). This gives the opportunity to configure the angle of attack of the wing.

For the experiment zigzag tape is applied on the top and bottom of wing. This is placed on the LE at 7 % of the chord. Experiment with a listening device confirmed the flow is turbulent downstream of the zigzag tape (and laminar upstream of it). The wings were painted black to limit the reflectivity of the laser light during the PIV measurements.

The wing dimensions are chosen as a compromise between manufacturability and to represent a scaled down version of a 2 propeller passenger aircraft. The wing parts were manufactured by a 5 axis CNC mill in which the product length is limited to a span of 900 mm. Therefore, the outboard wing is only 800 mm long, to stay well within the limits. The passenger aircraft that was used to inspire the dimensions of the wing is the ATR 42. Table 5.2 shows a comparison between the Control wing and three common 2 propeller passenger aircraft. Note that geometrically the Control wing is similar to these aircraft, however the Reynolds number is not. Therefore, the findings of the wind tunnel experiment cannot be directly translated to conclusions for full-scale passenger aircraft.

Table 5.2: Comparison between the Control wing and those of the ATR 42 (24), ATR 72 (25) and Fokker 50 (26).

Parameter	Symbol	Unit	Control wing	ATR 42	ATR 72	Fokker 50
Wing span	b	m	2.58	24.57	27.05	29.00
Propeller diameter	D	m	0.41	3.93	3.93	3.66
Number of blades	B	-	6	6	6	6
Wing area	S	m^2	0.62	54.5	61	70
Root chord	c_{root}	m	0.279			
Tip chord	c_{tip}	m	0.161			
Mean aerodynamic chord	c_{MAC}	m	0.24	2.22	2.26	2.41
Sweep angle of LE	Λ_{LE}	deg	0			
Propeller location	$2y_{prop}/b$	-	0.35	0.33	0.3	0.25
Aspect ratio	AR	-	10.9	11.1	12.0	12.0
Diameter to span ratio	$2D/b$	-	0.32	0.32	0.30	0.26
Cruise velocity	V_∞	m/s	19	154	142	139
Reynolds number	Re	10^6	0.3	23	21	22

They only differ in their twist distribution as can be seen in Figure 5.8. The Control wing has a constant twist of zero degrees while the Modified wing has a varying twist. This twist distribution is modified for the specific wing, propeller and operating conditions used in this wind tunnel experiment. The wing twist is applied around a line at 23 % of the root chord.

5.2.3 Wall

The function of the wall is to simulate a symmetry plane for the flow. There is no flow through the wall, therefore the right wing and propeller experience a flow as if there was also a left wing and a mirrored propeller (also rotating inboard up). Appendix D proofs with a numerical investigation the wall is an effective symmetry plane.

A window in the wall facilitates the PIV measurements on the inboard part of the wing. The cameras positioned on the left side of the test section can see the field of view (FOV) around the inboard wing through the window in the wall. Figure 5.9 shows the dimensions and positioning of the wall and window with respect to the wing. Note that the window is quite large at the rear of the wing. The purpose of this was to accommodate a camera looking at an angle at the FOV to perform stereoscopic PIV. However, no stereoscopic PIV was performed (Section 5.4.1 elaborates on why).

The wall was used as a support for the inboard wing part. Three holes in the window keep the inboard wing constrained in its position and angle of attack.

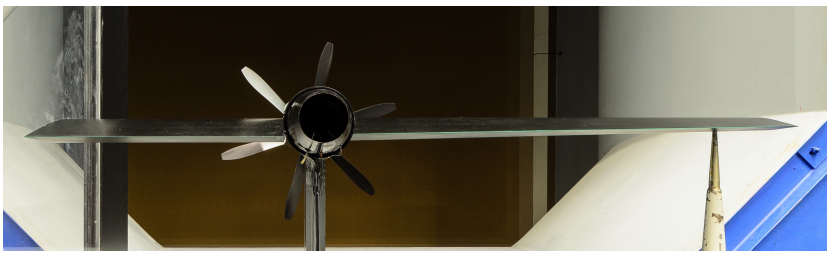

(a) Control wing

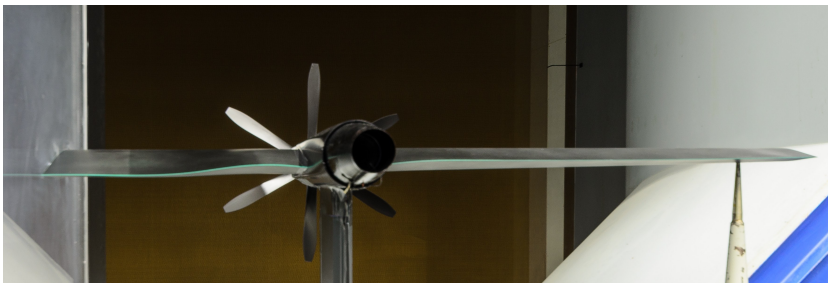

(b) Modified wing

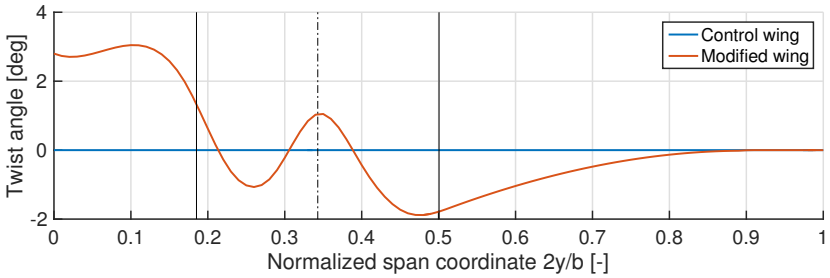

(c) Twist distribution

Figure 5.8: Rear view of the Control wing (top) and Modified wing (middle) and the twist distribution (bottom).

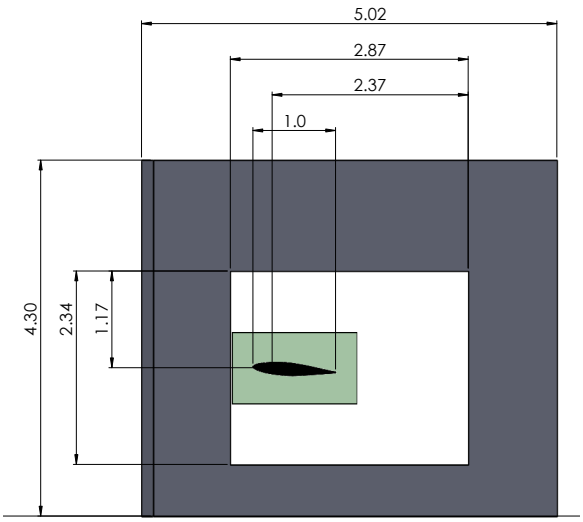

Figure 5.9: Wall used as symmetry plane during the wind tunnel test. Dimensions are normalised with the chord length at the wing root.

5.3 Test Conditions

The general operating conditions of the experiment are summarised in Table 5.3. These settings are a compromise between the wish to measure an as large as possible difference between the two wings and the limitations due to flow separation on the propeller blades or wing and the deterioration of PIV smoke. Specifically the freestream velocity is limited by the PIV smoke, the angle of attack of the wing by flow separation on the wing segment behind the up-going blade and the propeller blade angle, advance ratio and thrust coefficient by the flow separation on the propeller blades.

Table 5.3: Overview of the wind tunnel experiment operating conditions.

Parameter	Symbol	Value
Freestream velocity	V_∞	19 m/s
Wing angle of attack	α	4 deg
Reynolds number	Re	$3 \cdot 10^5$
Propeller angle of attack	α_p	0 deg
Propeller blade angle (at $r/R = 0.7$)	$\beta_{0.7}$	30 deg
Propeller advance ratio	J	0.695
Propeller thrust coefficient (predicted by XROTOR)	C_T	0.30

5.4 Measurement Techniques

Two types of experiments were performed: PIV (on cross-sections of the wing and propeller slipstream) and pressure measurements (of the propeller slipstream).

The objective of the wind tunnel experiment is to validate the Adapted VLM code for changes in lift distribution due to changes in wing design (in this case a change in twist distribution). With planar PIV the flow field around cross sections of the wing is determined and in the flowfield the circulation is used as a measure for the lift. More details on this procedure are given in Chapter 7. Normally, a better way to measure the lift distribution is with pressure taps in the surface of the wing. This can be done by a large number of pressure taps integrated into the wing surface. However, due to time and money constraints this was not feasible for this experiment.

Measurements of the total and static pressure inside the propeller slipstream allowed to determine the propeller thrust and validate XROTOR and the models used to modify the slipstream.

5.4.1 Planar Particle-Image Velocimetry (PIV)

Planar PIV measurements were taken on several cross-sections along the wing span and of the propeller slipstream. As Table 5.4 shows, the measurements of the wing were performed

for the Control (propeller-on and -off) and Modified wing (propeller-on). For the propeller slipstream three configurations were tested: propeller-off, propeller-on and propeller-on with the Control wing mounted. The locations of the PIV measurements are shown schematically in Figure 5.10.

Table 5.4: Overview of the planar PIV measurements.

PIV measurements of the wing

			Propeller-off	Propeller-on	
Nr	Span location (mm)	$2y/b$ (-)	Control wing	Control wing	Modified wing
1	60	0.047	✓	✓	✓
2	180	0.140	✓	✓	✓
3	265	0.206	✓	✓	✓
4	315	0.244		✓	✓
5	371	0.288	✓	✓	✓
6	515	0.400		✓	✓
7	565	0.438		✓	✓
8	620	0.481		✓	✓
9	725	0.562		✓	✓
10	885	0.687		✓	✓
11	1042	0.808		✓	

PIV measurement of the slipstream

			Propeller-off	Propeller-on	
Nr	Span location (mm)	$2y/b$ (-)	No wing	No wing	Control wing
12	442	0.343	✓	✓	✓

Planar PIV was performed at every location. This method gives a 2D, in-plane, vector field of the velocity. The out-of-plane velocity was not measured. In the propeller slipstream this velocity is expected to be significant, therefore stereoscopic PIV would have been the preferred method. However, during the experimental campaign this was tried and deemed infeasible for this specific setup since the second and angled camera did not receive enough light from the smoke particles.

At every location a number of PIV images are taken which are used to compute the time-averaged flow velocities. A large number is needed to remove the unsteady effects and noise in the resulting flow field. Inside the slipstream of the propeller the flow is more unsteady than outside, which is why more images are required here. Table 5.5 summarizes the number of PIV images taken per location.

A Quantel Evergreen 200 mJ Nd:YAG laser is used to light up the smoke particles for the cameras. For the measurement of the propeller slipstream the laser is directed at the Field of View (FOV) from the top-rear side. For the wing the laser sheet had to be split to come from the top-rear and bottom-rear. This was necessary to limit the shadow regions in the

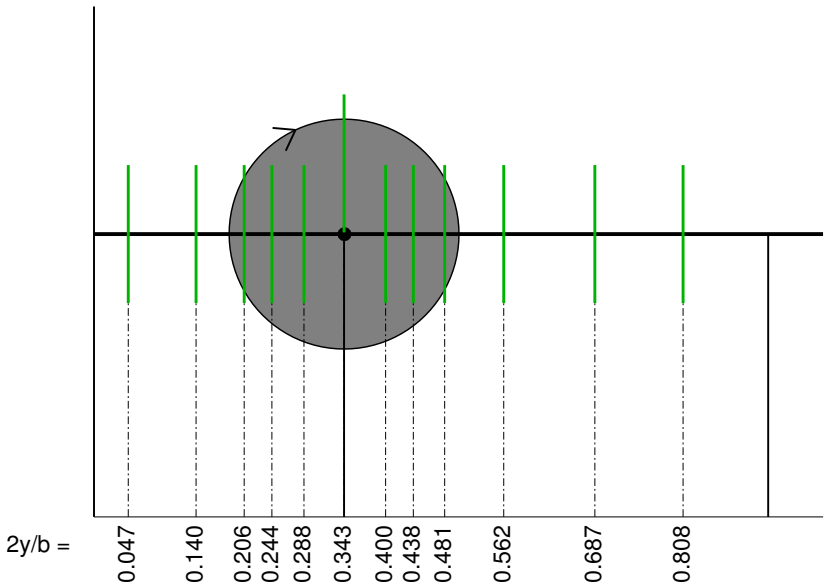

Figure 5.10: Schematic rear view of the propeller, wing, wall and pylon. Indicated are the locations of the planar PIV measurements. The location for the PIV measurement of the propeller slipstream lies a little higher with respect to the measurements of the flow around the wing.

Table 5.5: Number of PIV images taken for each specific location.

Object	Inside slipstream?	Number of images
Propeller	Yes	1000
Wing	Yes	500
Wing	No	250

FOV. Figure 5.11 shows the laser sheet for both the propeller slipstream measurement (left) and the for the wing (right).

Planar PIV measurements were performed, therefore the cameras were oriented straight at the FOV. Two cameras were place on top of each other (Figure 5.12) used to increase the FOV during one measurement. The measurements of the outboard wing were done with the cameras on the right side. For the inboard wing the cameras had to be on the left side since otherwise the propeller pylon would have blocked the FOV. On the left side the cameras looked through the window in the wall.

The FOV was too large to capture it with one camera at once, therefore it is built up from 4 separate parts. Two Lavision Imager Pro LX (16 MP) cameras were available for the experiment which were translated in the flow direction to get all 4 parts of the FOV. Figure 5.13 shows the dimensions of the 4 camera views and how they compose the complete FOV. The overlap in the camera views enables a smooth merging process.

The size of the single FOV resulted in a particle size of $d_\tau = 1-3$ pixels. The time difference between the images was set to $dt = 30\mu s$ which gave an average pixel displacement of ap-

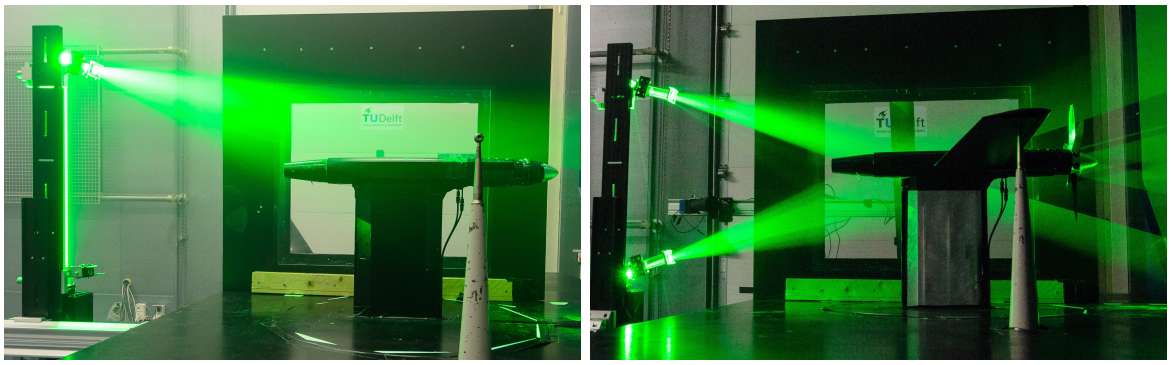

(a) Propeller slipstream (b) Cross-sections along the wingspan

Figure 5.11: Laser sheet for PIV measurements of the propeller slipstream (location 12) and the cross-sections along the wingspan (locations 1-11).

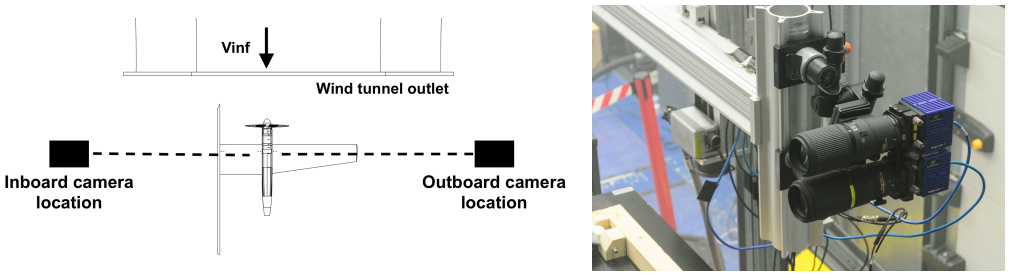

Figure 5.12: The cameras are placed left and right of the test section for the inboard and outboard Planar PIV measurement, respectively (left). And two cameras are placed directly above each other to extend the FOV (right).

proximately 10 pixels (based on the freestream velocity $V_\infty = 19$ m/s). Inside the slipstream a maximum displacement of approximately 18 pixels was found.

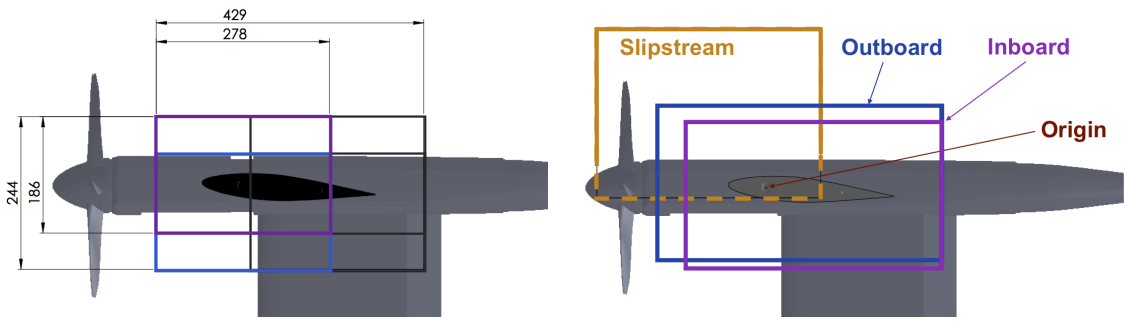

Figure 5.13: Field of view (FOV) consists of 4 separate views (left). The measurements for the propeller slipstream, inboard and outboard wing had their own combined FOV (right). Dimensions are in mm.

5.4.2 Total and Static Pressure Measurement of Propeller Slipstream

Pressure measurements were done in the propeller slipstream for propeller on and off. No wing was mounted during the both measurements. The total and static pressure were measured relative to the atmospheric pressure, $(p_{tot} - p_\infty)$ and $(p_{static} - p_\infty)$ respectively.

As Figure 5.14 shows, a pitot-static tube was placed 64 mm ($x/R = 0.31$) behind the propeller plane and at the height of the propeller axis. The probe was moved horizontally through the slipstream from the nacelle to 250 mm ($y/R = 1.23$) from the propeller axis. The measurement locations were 2mm apart. At every location the measurement was performed for 5 seconds and both pressures are recorded at a sampling rate of 5 Hz.

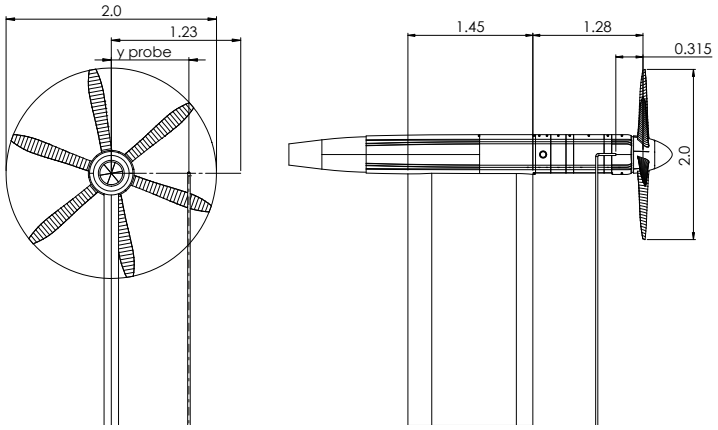

(a) Rear view (b) Side view

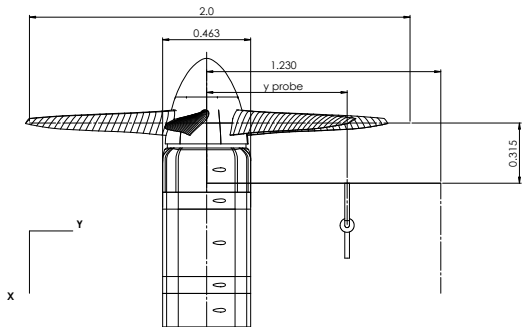

(c) Top view

Figure 5.14: Rear, side and top view of propeller and location of pitot-static tube for the pressure measurements. Dimensions normalised with the propeller radius.

5.5 Data Post-Processing

Post processing of the results from the wind tunnel experiment is done on the PIV images and pressure measurement. The PIV images are first processed to raw averaged velocity fields. Thereafter they are masked, interpolated and stitched to complete and smooth velocity fields. The pressure measurements are also averaged and used to calculate the propeller thrust. These steps are described in more detail in this section.

5.5.1 PIV Image Post-Processing

The direct result of the PIV measurement during the wind tunnel experiment are a set of image pairs. The image pairs are taken with a small time gap between each other. In this time the smoke particles move small amount which allows for a velocity field to be determined. The set of image pairs are first processed to a vector field using cross correlation between the two images. Then the set of vector fields is averaged to get the mean velocity field. During the post processing a number of image processing steps are taken to improve the quality of the image with the goal of improving the end result. These steps are customary in PIV post processing and are performed in Davis (the PIV capturing and post processing program of Lavision).

1. Raw PIV images
2. Reduce reflections / normalize intensity
3. Sharpen image (optional)
4. Cross correlation
5. Remove outliers
6. Take average

After the processing of the images in Davis more post-processing steps are taken. The results from Davis are not perfect, therefore the bad parts are masked. Bad parts are selected based on the standard deviation that is calculated together with the average in Davis and on a visual inspection and judgement of the images.

Thirdly, the gaps in the images are interpolated using the Matlab program *inpaint_nans* (27). The interpolation method used follows the so-called 'spring analogy', which means an empty point in the image wants to be the same as its neighbour. This method fills the gaps smoothly and behaves constant in extrapolation. As can be seen in the figures the bottom left corner is missing, this was true for most of the PIV images taken. This gap is filled by *inpaint_nans* mostly with extrapolation which gives slightly unrealistic results as can be seen by close inspection of the bottom two images of Figure 5.16. It is therefore important that this part of the flow field is not used for any further calculations. The same is true for the boundary layer.

Step four is to combine the separate images to one big velocity field. The small images have a certain overlap region. In this region the value of the new velocity field is based on the

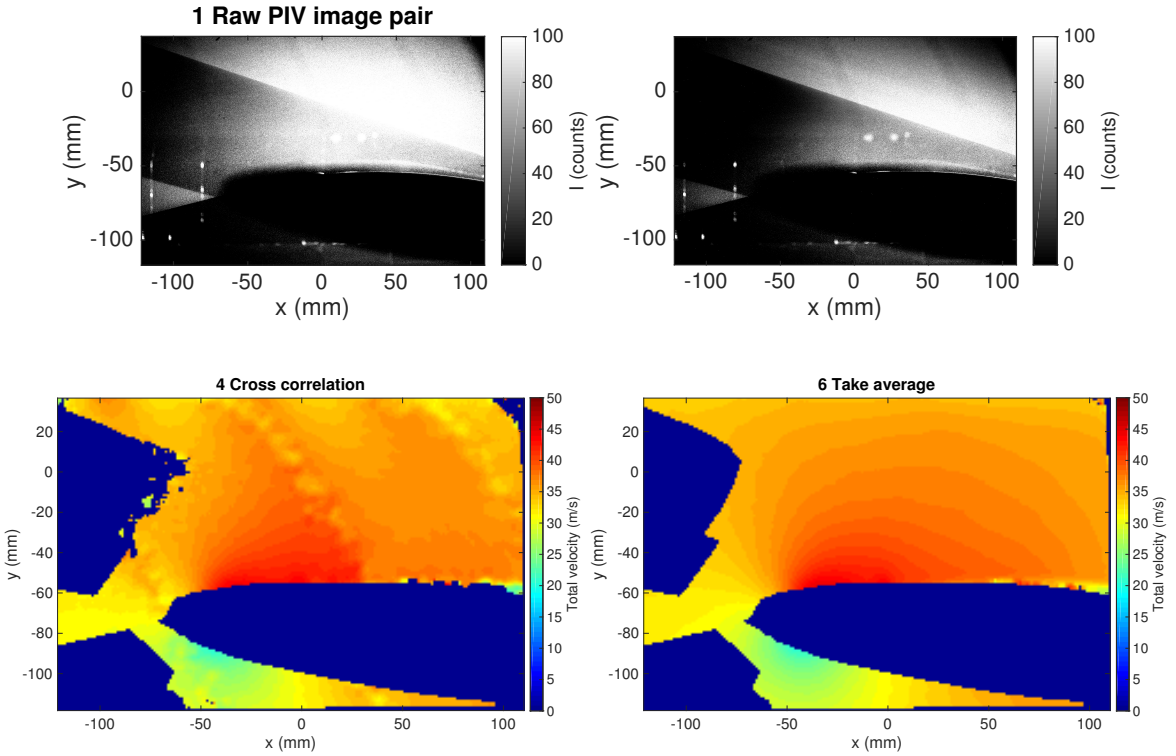

Figure 5.15: A PIV image pair is used to make a velocity field using cross correlation. Then a number of these velocity field results are used to calculate an average velocity field.

weighted average of both small images. The weight depends linearly on the distance in the region to both of the source images.

The last step removes the regions that cannot be trusted in the interpolated velocity field by masking area around the airfoil and the edges of the FOV.

A summary of the steps is given below and Figure 5.16 shows the results.

1. Raw velocity field
2. Masked velocity field
3. Interpolated velocity field (27)
4. Combined velocity field
5. Combined and masked velocity field

5.5.2 PIV Uncertainty Quantification

The final velocity flow fields as are the results of the post processing steps explained above contain some error. Two main sources are identified for this error: Cross correlation and

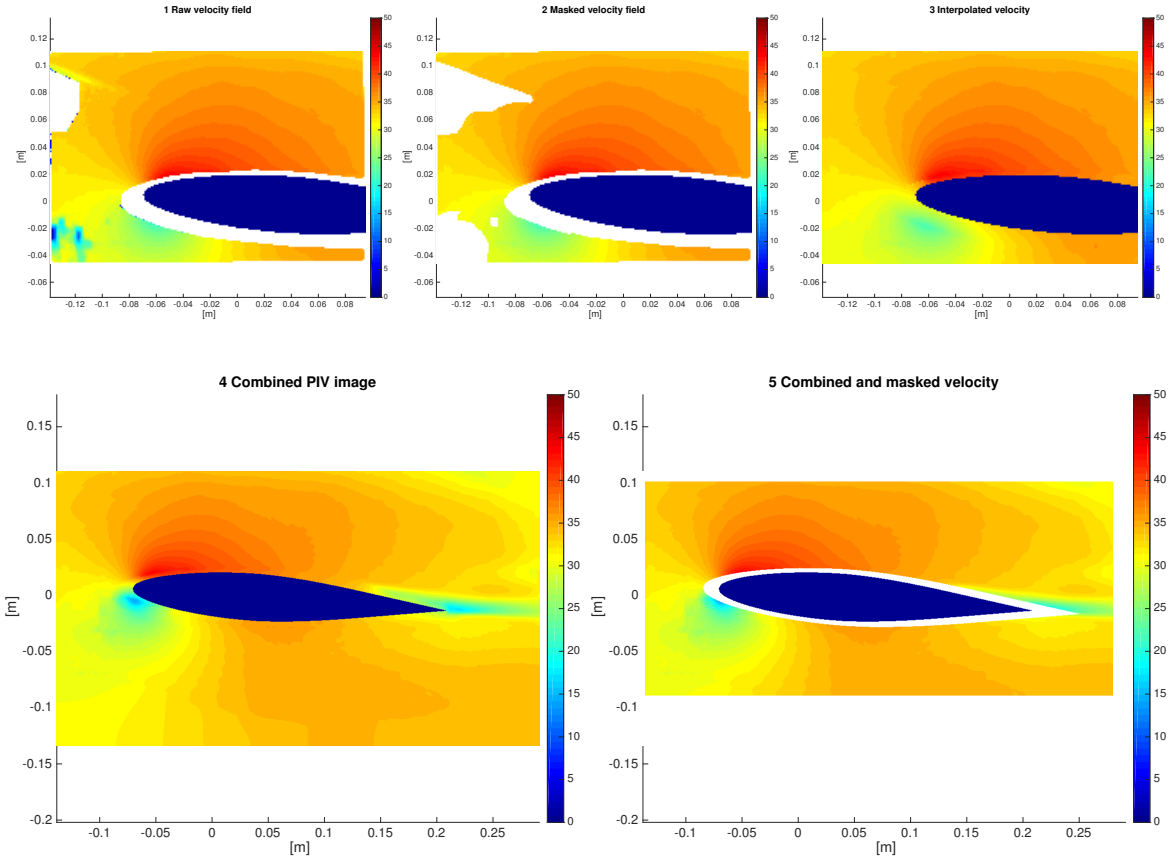

Figure 5.16: Steps of post processing the velocity fields. It starts with the results directly from Davis (top left). The third step is to mask the bad results (top mid). Then the gaps are interpolated with the Matlab program inpaint_nans (27) (top right). Next is to combine the 4 images into the complete FOV (bottom left). Finally the image is masked again to remove the parts which are uncertain (the boundary layer around the airfoil and the edges of the FOV, bottom right).

averaging. The error in cross correlation is quantified in Appendix E, and is shown to be 0.5 m/s. The error in averaging is calculated simultaneously with the average flow field and the standard deviation is saved with it.

It is important to take these errors into account for further calculations on these velocity fields (the circulation for example). The approach to do this is explained here. Before the calculation is performed an error field is added to the velocity field. This error field itself is the sum of two fields, one for the cross correlation error and one for the averaging error. This is represented by the following equations:

$$\Delta \mathbf{U} = \epsilon_{cross} \cdot \mathbf{X} + \sigma_{\mathbf{U}} \cdot \mathbf{Y} \tag{5.1}$$

$$\Delta \mathbf{W} = \epsilon_{cross} \cdot \mathbf{X} + \sigma_{\mathbf{W}} \cdot \mathbf{Y} \tag{5.2}$$

Here are $\Delta\mathbf{U}$ and $\Delta\mathbf{W}$ the matrices containing the error field for the velocity in x and z direction, respectively. The error due to the cross correlation ϵ_{cross} is a scalar with the value found in Appendix E. The error due to averaging is captured with $\sigma_{\mathbf{U}}$ and $\sigma_{\mathbf{W}}$, both are matrices with the same size as the velocity field. The random numbers are generated as a field of the same size and are represented by $\mathbf{X}$ and $\mathbf{Y}$. They are random generated numbers following a standard normal distribution.

5.5.3 PIV-based Circulation and Lift Computation

In the PIV velocity fields the circulation can be calculated. The definition of the circulation is given by Equation 5.3. It is the integral over a closed curve C of the tangential velocity times the distance along C.

$$\Gamma = -\oint_C \mathbf{V} \cdot \mathbf{ds} \tag{5.3}$$

If a closed curve is drawn around the airfoil the circulation of the wing at that span location can be determined. This is done with the velocity field results from the PIV measurements. To account for the uncertainty as mentioned in the previous section the procedure of selecting a contour and calculating the circulation in the velocity field which includes the random error is repeated a number of times. Every new calculation has therefore a slightly changed velocity field and also the contour is changed.

In Figure 5.17 the typical result of generating 100 semi-random curves is shown. The curves are generated by connecting a number of points around the airfoil. These points are randomly generated inside a certain circle. These circle are located in order to guide the curves around the airfoil and away from the regions where most of the velocity field values are a result of interpolation.

Figure 5.18 shows the result of the circulation calculation for a typical velocity field outside and inside the slipstream. As can be seen performing the calculation 300 times is sufficient to find a good mean and standard deviation for the circulation.

5.5.4 PIV- and Pressure-based Propeller Thrust Computation

The propeller thrust is calculated from the pressure measurements and PIV velocity fields. The method used is described in this section.

Following the momentum theory (explained by, amongst others, McCormick (29)) the thrust

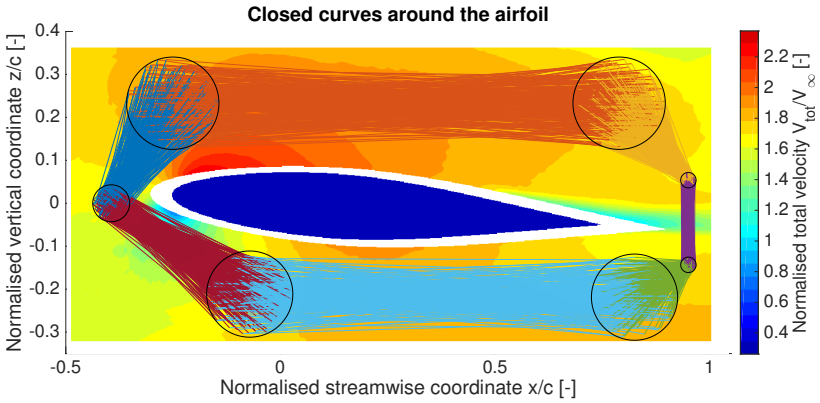

Figure 5.17: Typical result of semi-randomly generating 100 curves around the airfoil. The curves go through points around the airfoil which are randomly generated inside certain circles. These circles guide the curve around the airfoil and away from the regions where the velocity field data is a result of interpolation.

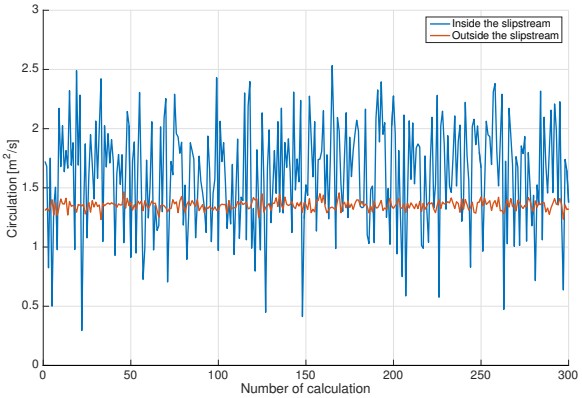

Figure 5.18: Circulation as calculated in the velocity field including the random error, repeated 300 times. Calculation performed on a typical flow field from inside and outside the slipstream.

T on a propeller is given by the pressure difference over the propeller plane:

$$T = A(p_{tot_d} - p_{tot_u}) \tag{5.4}$$

Here is A the area of the propeller plane, p_{tot_d} the total pressure downstream of the propeller plane and p_{tot_u} the total pressure upstream. The total pressure up and downstream are given by:

$$p_{tot_u} = p_\infty + \frac{1}{2}\rho V_\infty^2 = p_1 + \frac{1}{2}\rho V_1^2 \tag{5.5}$$

$$p_{tot_d} = p_\infty + \frac{1}{2}\rho V_3^2 = p_2 + \frac{1}{2}\rho V_1^2 \tag{5.6}$$

Here are p_1 and p_2 the static pressure before and behind the propeller plane, respectively. The velocities V_1 and V_3 are at the propeller plane and far downstream, respectively. Note that the velocity in these relations is the total velocity. See Figure 5.19 for the naming convention used in these equations.

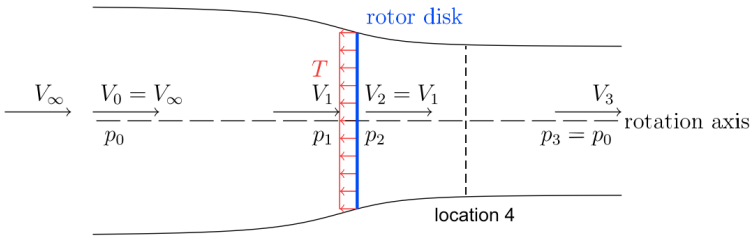

Figure 5.19: Schematic side view of the streamtube around a propeller. The velocities and pressures are indicated to show the naming convention used in the equations in this section. Image taken from Kuijk (30) and added location 4.

To isolate the contributions from the propeller blades, Equation 5.4 is adapted to:

$$T = A(p_{tot_d} - p_{tot_u})_{pOn} - A(p_{tot_d} - p_{tot_u})_{pOff} \tag{5.7}$$

Here the subscripts pOn and $pOff$ refer to the propeller on and propeller off case, respectively.

These relations are used to determine the thrust from the measurements. For the pressure measurement Equation 5.7 can be rewritten as:

$$T = \int_{r_{\text{hub}}}^{R} 2\pi r \left[\left(p_{tot_d} - p_\infty - \frac{1}{2}\rho V_\infty^2 \right)_{pOn} - \left(p_{tot_d} - p_\infty - \frac{1}{2}\rho V_\infty^2 \right)_{pOff} \right] dr \tag{5.8}$$

The pressure difference changes along the radius of the propeller, therefore the equation is rewritten as an integral over the radius of the propeller. The total pressure upstream is rewritten as the sum of static and dynamic pressure. During the experiment the quantity $p_{tot_d} - p_\infty$ was measured and can be directly used in this equation. The freestream dynamic pressure $\frac{1}{2}\rho V_\infty^2$ is calculated from the measured freestream density ρ and velocity V_∞.

In order to calculate the thrust from the velocity fields (from the PIV measurements) a different formulation is needed for Equation 5.4:

$$T = \int_{r_{\text{hub}}}^{R} 2\pi r \left[\left(p_4 + \frac{1}{2}\rho V_4^2 - p_\infty - \frac{1}{2}\rho V_\infty^2 \right)_{pOn} - \left(p_4 + \frac{1}{2}\rho V_4^2 - p_\infty - \frac{1}{2}\rho V_\infty^2 \right)_{pOff} \right] dr$$

(5.9)

Similar as before the rewritten as an integral over the propeller radius. However, now the total pressure downstream is rewritten as the sum of the static and dynamic pressure at location 4. This is the location downstream of the propeller where the velocity is extracted from the velocity fields.

The static pressure p_4 in Equation 5.9 was not measured during the wind tunnel experiment. Rewriting Equation 5.4 for thrust to isolate the effect of the static pressure gives:

$$\begin{aligned} T = &\int_{r_{\text{hub}}}^{R} 2\pi r \left[\left(\frac{1}{2}\rho \left(V_4^2 - V_\infty^2 \right) \right)_{pOn} - \left(\frac{1}{2}\rho \left(V_4^2 - V_\infty^2 \right) \right)_{pOff} \right] dr \\ &+ \int_{r_{\text{hub}}}^{R} 2\pi r \left[(p_4 - p_\infty)_{pOn} - (p_4 - p_\infty)_{pOff} \right] dr \end{aligned} \tag{5.10}$$

Here the latter part represents the thrust due to the static pressure. Two approaches are now possible to circumvent the missing data of the static pressure in the PIV measurement. One, the static pressure found with the pressure measurement is used to fill in the missing static pressure for the PIV velocity field. Note that it is important to take location 4 at the same distance behind the propeller as the pressure measurement was performed. Also note that the pressure measurement was performed on a horizontal axis on the right side of the nacelle and the PIV measurement was in a cross section with a vertical (not horizontal) component.

Chapter 6

Experimental Results: Propeller Slipstream

Results from the wind tunnel experiment on the propeller are the total and static pressure in the slipstream and the velocity field acquired with planar PIV. This chapter covers these results, the calculated thrust from both sources and finally compares the results with the Adapted VLM model.

6.1 Total and Static Pressure in Propeller Slipstream

The total and static pressure are measured in the propeller slipstream on a horizontal axis at right side and at $\Delta x/R = 0.315$ behind the propeller plane. Figure 6.1 shows these results for the isolated propeller with the propeller on and off.

With the propeller off the total pressure is constant for the whole range that is measured. This is as expected since no momentum is added because the propeller is off. the static pressure is lower with respect to the freestream conditions because the velocity is slightly increased around the nacelle. This is especially visible close to the nacelle.

Propeller on shows a strong increase of the total pressure inside the slipstream. This is due to the added energy to the flow. A part of this added as static pressure which is increased over a large range of the slipstream. The rest is put into an increased velocity in the slipstream. Near the edge of the slipstream the static pressure drops because of the blade tip vortices. Inside these vortices the velocity is very high and the static pressure drops because of it. A slight drop of total pressure at the edge of the slipstream is also visible. This indicates the loss of energy due to viscosity inside the tip vortices.

Outside the slipstream the static pressure is also increased even though the total pressure is equal to the propeller off case. This indicates the velocity is decreased with respect to the freestream.

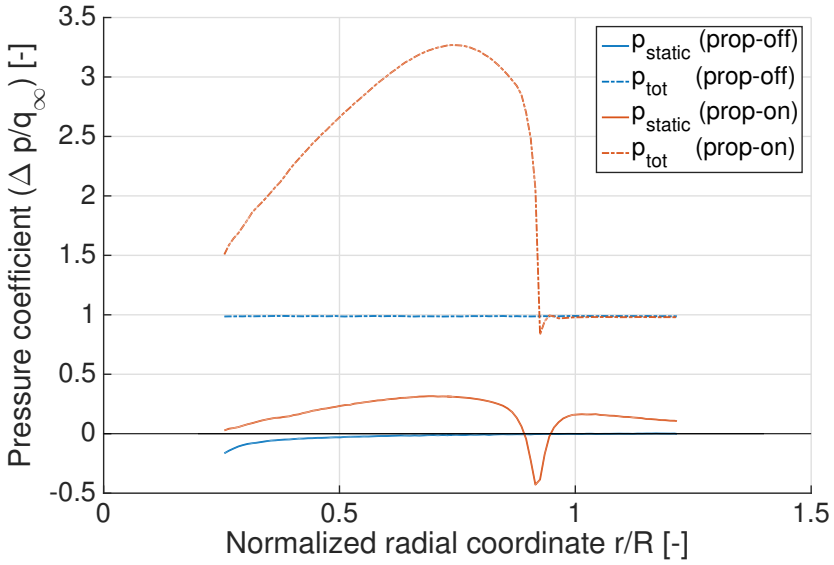

Figure 6.1: Results of pressure measurement for propeller on and off. The total and static components are relative to the atmospheric pressure and made non-dimensional with the freestream dynamic pressure, $\frac{p_{tot}-p_\infty}{q_\infty}$ and $\frac{p_{static}-p_\infty}{q_\infty}$ respectively.

6.2 Velocity Field of Propeller Slipstream

With planar PIV the velocity field of the propeller slipstream is measured. It concerns the the cross section formed by the propeller centre axis and the z axis in upward direction. Figure 6.2 shows the this velocity field for propeller off, propeller on without wing and propeller on with the Control wing. Note that the propeller location is indicated with a straight line (which is dotted for the propeller off case) and that the nacelle is indicated by the dark blue area surrounded with a white band. The Figure shows the velocity magnitude and direction.

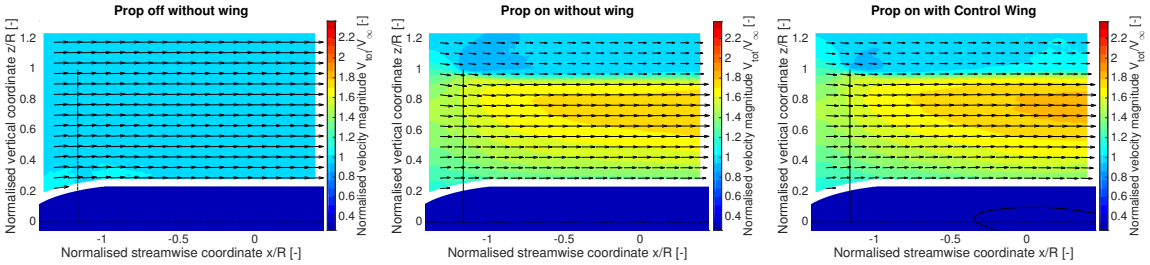

Figure 6.2: Velocity magnitude field and flow vectors of the slipstream of propeller off (left), isolated propeller (middle) and with propeller and the Control wing (right). Location of the planar PIV measurement was at $y/\frac{b}{2} = 0.34$ with respect to the wing and $\Delta y_p/R = 0$ with respect to the propeller location.

In the left figure the propeller-off case is shown. The flow velocity is therefore almost equal to the freestream velocity. Only a small effect of the nacelle is noticeable by two aspects. One, a slight increase is the velocity around the nose of the nacelle (which coincides with the results from the pressure measurements). And two, the streamlines show a slight upward motion of

the flow to go around the nacelle.

The middle figure contains the flow field for propeller on without the wing. A strong increase of the flow velocity indicates the propeller effect. The axial development of the velocity is also visible. Furthermore a small contraction of the slipstream can be noticed looking at the streamlines.

The effects that are noticed are the result of the conservation of energy and mass. The increase in static pressure behind the propeller as noticed in the results of the pressure measurement are the source of the axial velocity increase. The propeller adds energy to the flow in the form of increased static pressure and increased velocity. The static over pressure is then converted into axial velocity moving downstream. The increase in axial velocity means the area of the slipstream contracts to ensure the conservation of mass. This goes together with a decrease of the velocity (and increase of the static pressure) outside of the slipstream. This is confirmed by the pressure measurements in Figure 6.1 and the velocity acquired by PIV measurement in Figure 6.3.

The result for propeller on with the Control wing is shown in the right figure. Again the increase of the velocity is clear. Also the axial development of the velocity is present. Compared with without wing the velocity is slightly higher. The contraction of the slipstream is only seen just behind the propeller, further downstream the slipstream seems to grow bigger in size. The increase in velocity and contraction and expansion are better visible in Figure 6.3. Both of these effects can be explained by the presence of the wing. The flow around an isolated wing has an increased velocity over the wing and a certain circulation around the wing. Superposition of this effect with the isolated slipstream explain the increased velocity observed in the slipstream and the way the streamlines bend around the wing.

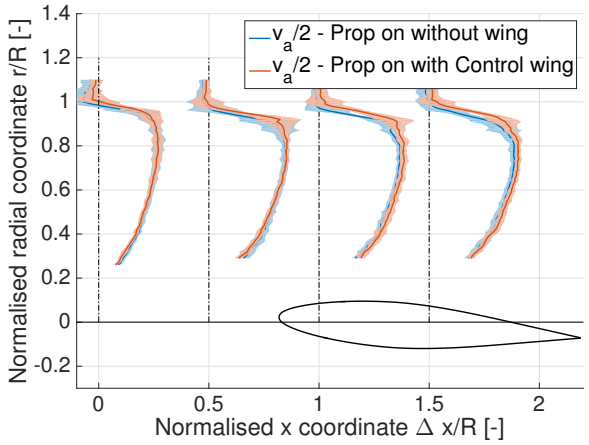

Figure 6.3: The axial velocity component in the propeller slipstream at different locations behind the propeller. The dotted line indicates the location of the corresponding velocity profile. The value of the velocity divided by 2 is plotted with respect to this dotted line.

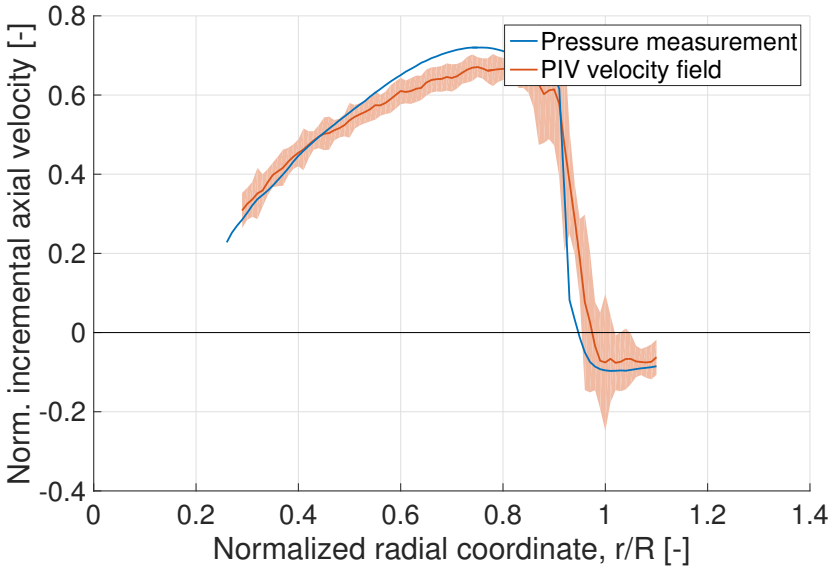

Figure 6.4: Axial velocity increase at $\Delta x/R = 0.135$ behind the propeller plane.

6.3 Propeller Thrust

As described in Subsection 5.5.4 the propeller thrust can be calculated from the pressure measurements. Table 6.1, which shows the propeller thrust from the pressure measurement and XROTOR, shows that XROTOR overpredicts the propeller thrust with 15%.

Table 6.1: Propeller thrust coefficient.

Source	C_T
Pressure	0.2644
XROTOR	0.3043

The propeller thrust can also be calculated from the PIV velocity fields (see Subsection 5.5.4), however, this is only the thrust based on the axial velocity component. From the pressure measurement the same component can also be calculated. Both are compared in Table 6.2, which shows their values match very good. Considering that these results are based on same location downstream of the propeller, but at different azimuthal position, indicates that the thrust coefficient of the pressure measurement is correct and that of XROTOR is not.

Table 6.2: Propeller thrust coefficient component from axial velocity.

Source	**Location**	$C_{T_{\text{axia velocity}}}$
Pressure	$\Delta x/R = 0.315$	0.2188
PIV velocity field	$\Delta x/R = 0.315$	0.2203

No acceptable explanation for the overprediction by XROTOR is available at this time.

6.4 Comparison with Adapted VLM Results

In this section the results of the wind tunnel experiment are compared with the numerical (Adapted VLM) results. Both the slipstream contraction and development of the axial velocity are discussed. Unfortunately the swirl recovery cannot be analysed with the results on the propeller from the experiment.

First, look at the contraction of the slipstream. Figure 6.5 repeats the PIV velocity field for the propeller slipstream without wing and with the Control wing. This time the contraction as predicted by the Adatped VLM is added. For the isolated propeller it is clear the contraction is not modelled well. Although it is in the right order of magnitude within this field of view, it seems to move away from the actual contraction as found in the PIV measurement.

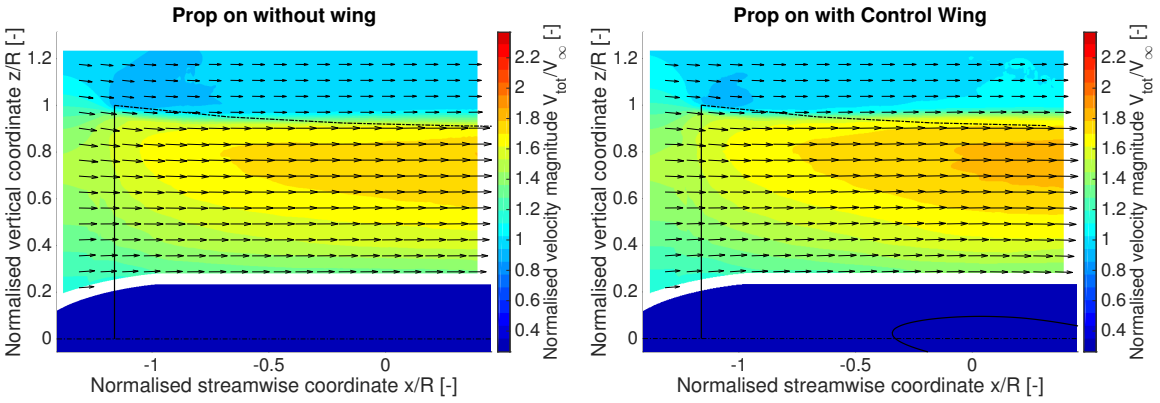

Figure 6.5: Contraction of the slipstream predicted by the Adapted VLM code (shown with the dotted line) compared to the velocity field measured by PIV.

The presence of the nacelle is not accounted for in the model of the slipstream contraction. Also, the flow here moves upward to go around the nacelle, as has already been shown with the propeller off configuration. This would move the edge of the slipstream more outward and make the contraction less than expected. Therefore the nacelle is the likely reason for this miss match. Including the nacelle in the model is recommended to improve it.

With the presence of the wing it is not better. The effect of the wing is modelled and noticeable in the result, however the absolute values are not correct. This indicates the model for deflecting the slipstream needs refinement.

Second, the development of the axial velocity is shown in Figure 6.6 for the isolated propeller configuration. The increase of axial velocity is noticeable in both the PIV velocity field and Adapted VLM results. However, the numerical model starts with an under prediction of the velocity and then has a stronger increase moving downstream. Halfway over the wing maximum velocity is predicted almost equal. This indicates the simplification (basing the development factor on an elliptical blade loading) used to model this might be an oversimplification.

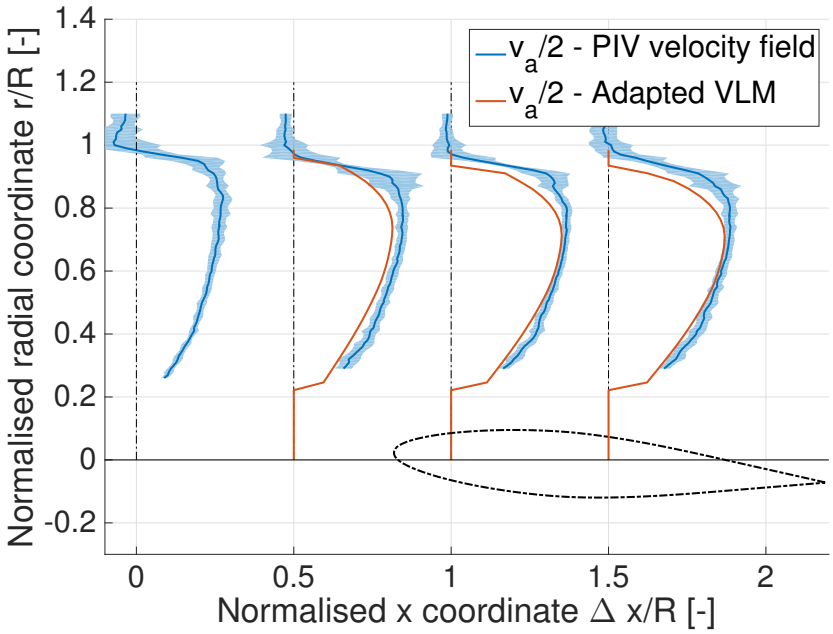

Figure 6.6: Development of the axial velocity in the slipstream predicted by the XROTOR and Adapted VLM code compared with the PIV velocity flow field. Axial velocity is divided by 2 and plotted with respect to the dotted line, this line is also the location of the where the velocity is measured.

Chapter 7

Experimental Results: Wing Lift Distribution

Results from the wind tunnel experiment based on the velocity fields around the wing profile sections are analysed in Section 7.1. The lift distribution, obtained from these velocity fields, is compared with the results of the Adapted VLM model in Section 7.2.

7.1 Velocity Fields around Wing Profile Sections

The velocity fields that are found with the PIV measurement are a 2D vector field of the velocity in the x-z plane at the corresponding span location (in y direction). The results can be distinguished into 4 groups based on the location of the measurement plane:

- Outside the slipstream.
- At the edge of the slipstream.
- Inside the slipstream, behind the upgoing blade.
- Inside the slipstream. behind the downgoing blade.

These typical flow fields are shown in Figure 7.1 and are discussed below.

First are the result outside of the slipstream. Outside of the slipstream is both inboard and outboard of the slipstream for both the Control and Modified wing. Also the flow around the Control wing with propeller off is considered flow outside of the slipstream. As can be seen in the top left figure the mean flow velocity is around the freestream velocity. As expected, the flow above the airfoil is faster than below. There is also a distinct region with low velocity at the lower side of the airfoil nose, coinciding with the expected location of the stagnation point. Furthermore, the wake of the wing is clearly visible as a region of lower velocity directly behind the airfoil. This is the result of the loss of momentum in the viscous boundary layer around the airfoil.

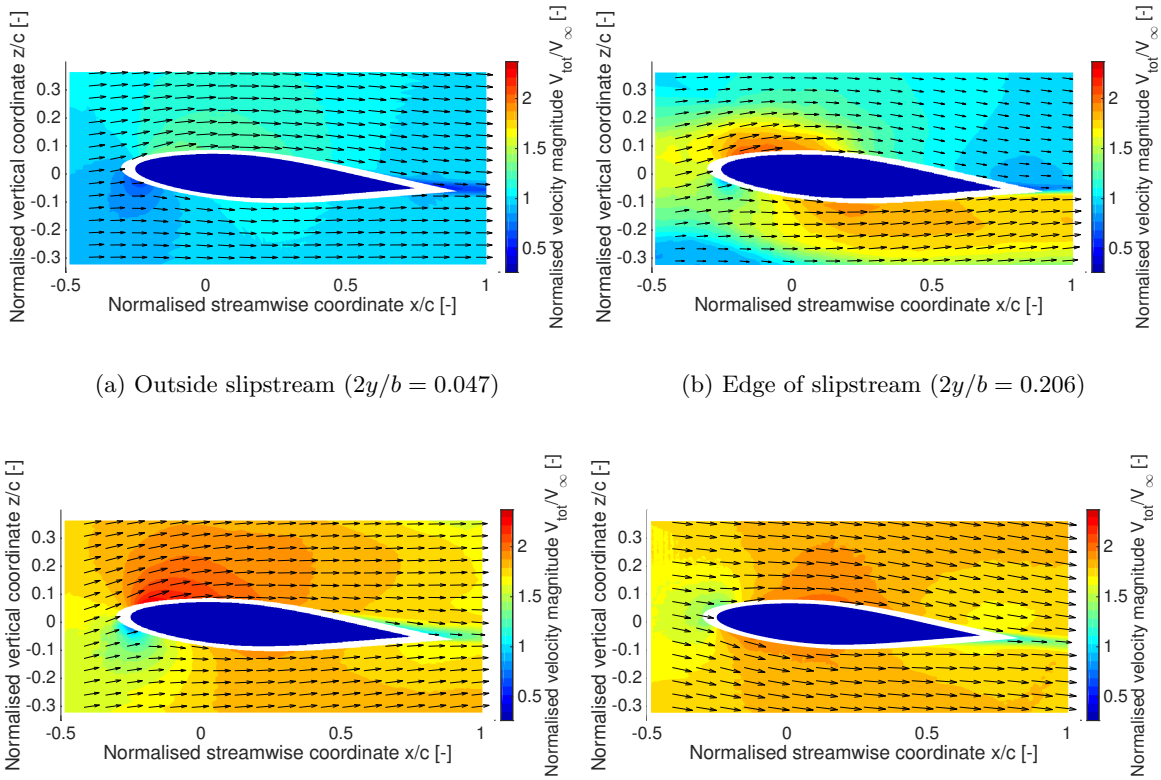

(a) Outside slipstream ($2y/b = 0.047$)

(b) Edge of slipstream ($2y/b = 0.206$)

(c) Inside slipstream, behind upgoing blade ($2y/b = 0.244$)

(d) Inside slipstream, behind downgoing blade ($2y/b = 0.400$)

Figure 7.1: Typical flowfield result from the PIV measurement. The velocity magnitude and direction are shown for a station outside the propeller slipstream, on the edge of it and inside it behind the upgoing blade and the downgoing one (bottom right).

Next is the flow inside the slipstream behind the upgoing blade (bottom left). The effect of the propeller is clearly seen in the increased velocity and upgoing direction of the streamlines. The usual effects around an airfoil, also noticed in the flow field outside of the slipstream are also noticeable here: Increased velocity on top of the airfoil, low velocity at the lower side of the nose and the wake behind the airfoil.

For the flow behind the downgoing blade look at the bottom right figure. Also at this location the flow behaves as expected. The velocity is increased, the flow has a downgoing component and there is a wake behind the airfoil. However, there is not much difference in velocity between the upper side compared to the lower side of the airfoil. Moreover, the stagnation point is found slightly above the nose (instead of under it). This suggests there is not much lift generated and it might even be a bit negative. This will be confirmed with the calculation of circulation in Section 7.2.

Finally the flow field at the edge of the slipstream is shown in the top right figure. This particular field is behind the upgoing blade as can be seen by the upward component of the

incoming flow velocity. The increase in velocity in the slipstream is only visible in part of the the flow field, which suggests that this is actually the edge of the slipstream. Remarkable is the difference is size of the region with increased velocity above the airfoil compared to below. This can be explained by the spanwise shear of the slipstream when it impinges on the wing. On the lower side the slipstream moves inboard and on the top side outboard. This is the reason a larger part of the slipstream is visible on the lower side of the airfoil.

Now to predict the lift at this location is very difficult. Clearly the velocity on the lower side is much higher than on the upper side. Normally this would suggest a very large negative lift following the Bernoulli's principle of a high velocity creating a low static pressure. However, the static pressure inside the slipstream is increased due to the propeller at the propeller plane. Although it is true that the static pressure recovers when moving downstream (and increasing the axial velocity and contracting the slipstream in the process) it is not expected that is already fully recovered at this location. It is therefore not possible to say anything about the actual lift at this location without quantifying the static pressure as well. Unfortunately this was not possible in this setup and therefore there is not lift result at this (and the other edge of the slipstream) location. This is the reason that Section 7.2 shows lift results for all locations along the span except at the slipstream edges. It is possible to calculate the circulation at these edges and perform the calculation for the lift, however, it would not produce correct results. Another way of looking at this is that the flow at the slipstream edges is highly 3 dimensional and quite complex compared to the other locations. The method used to determine the lift from circulation is a result that is only valid in a 2D flow; using this for these locations would not be valid.

Lift prediction for the other span locations have almost the same challenges. There is one difference which makes it possible to predict the lift without knowing the increase in static pressure. Any location on the wing, except on the edge of the slipstream, experiences on the upper and lower side flow either fully from the propeller or from the freestream conditions. This means that inside the slipstream the upper and lower side experience the same increase in static pressure. The effect of this cancel each other when the lift is calculated from the difference in pressure between the upper and lower side of the wing.

7.1.1 Comparison of Propeller On and Off

Now the flow around the Control wing is compared between propeller-on and -off. Outside the slipstream no significant changes are expected, which is confirmed in Figure 7.2.

Inside the slipstream the velocity is, of course, much higher than for the propeller-off case. Figure 7.3 shows the velocity field for a span location inside the slipstream. The increase is velocity is very obvious and also the up flow behind the upgoing blade is clearly visible from the streamlines.

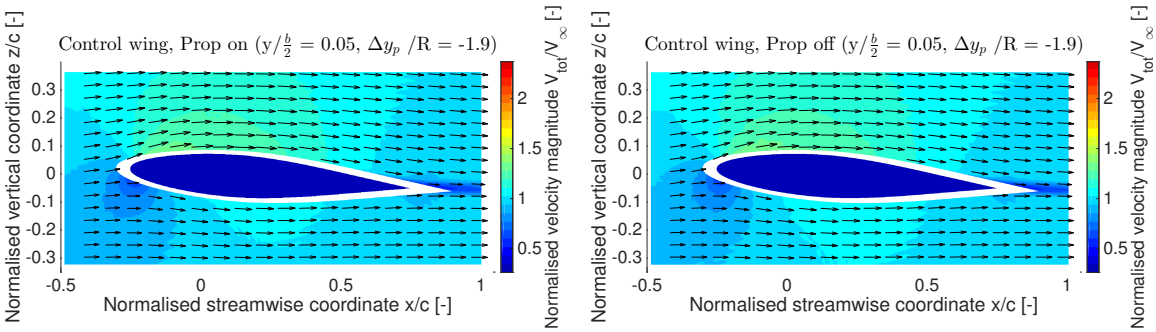

(a) Propeller-on (b) Propeller-off

Figure 7.2: Velocity magnitude field around the Control wing for propeller-on and propeller-off. Span location is outside the slipstream.

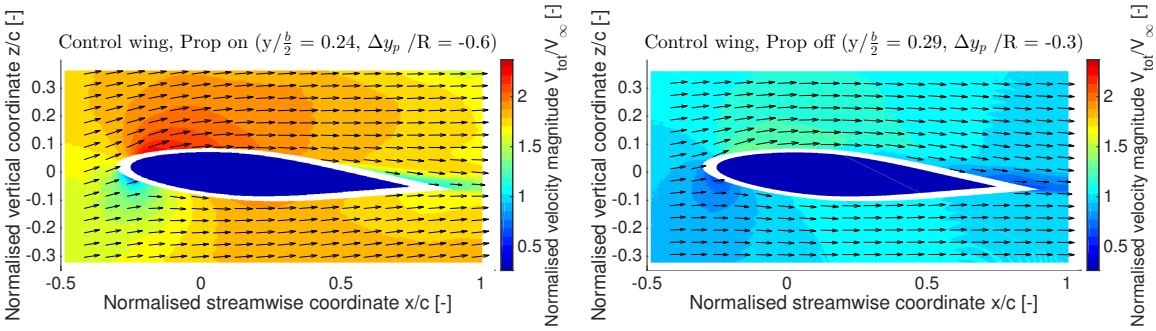

Figure 7.3: Velocity magnitude field around the Control wing for propeller on (left) and propeller off (right). Span location is inside the slipstream.

7.1.2 Comparison of Control and Modified Wing

Comparing the Control and Modified wing with propeller on is done in the following section. The flow field outside of the slipstream is shown in Figure 7.4. This shows two very similar velocity fields. However, by looking closely a the flow vectors it is observed that the Modified wing deflects the flow stronger downwards, which suggests a stronger lift. This is due to the increased angle of attack of the local airfoil has with the flow. The changed twist distribution increased the angle of the airfoil at this location, which also increased the angle of attack the airfoil here experiences. When the airfoil is at a higher angle of attack the lower velocity at the bottom gets slower and the higher velocity over the top gets faster.

Inside the slipstream, the twist of the Modified wing is almost the same as the Control wing. This also leads to almost the same velocity field (Figure 7.5). The same lift on both of these wing sections is expected.

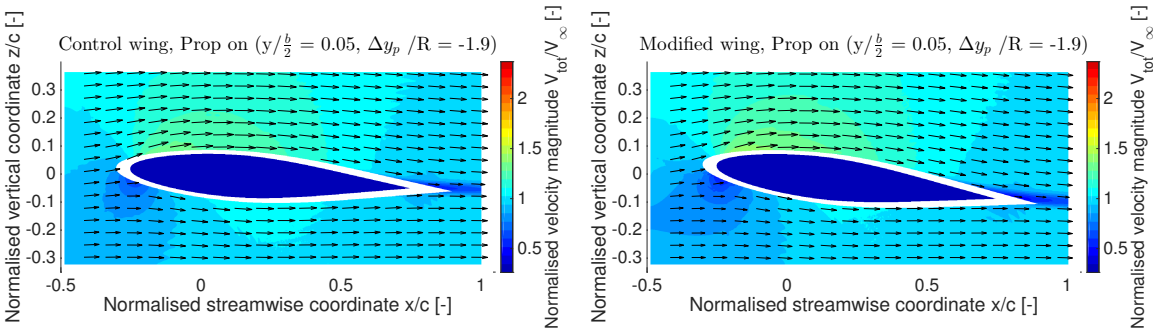

Figure 7.4: Velocity magnitude field around the Control (left) and Modified (right) wing with propeller on. Span location is outside the slipstream.

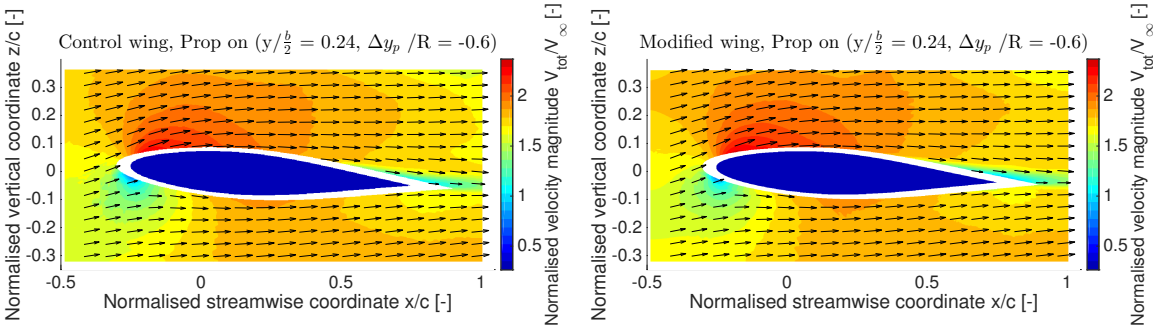

Figure 7.5: Velocity magnitude field around the Control (left) and Modified (right) wing with propeller on. Span location is outside the slipstream.

7.2 Lift Distribution

From the velocity fields the circulation can be calculated. The method used to do this is explained in Section 5.5.3. The results are compared with the predictions by the Adapted VLM model. This model is used to analyse the same setup as is tested in the wind tunnel, including the propeller-induced velocities, wing, wall, pylon and floor. Figure 7.6 shows how this setup is represented in the Adapted VLM model.

The results for the lift distribution are first discussed for the Control wing for the propeller-off case, then the effect of the propeller induced velocities is discussed for the Control wing with propeller on. Finally, the differences in the lift distribution between the Control and Modified wing are observed.

7.2.1 Control Wing with Propeller-off

The results are shown in Figure 7.7 for the Control wing for the propeller-off case. The experimental results include an error bar that indicates one standard deviation of the variation

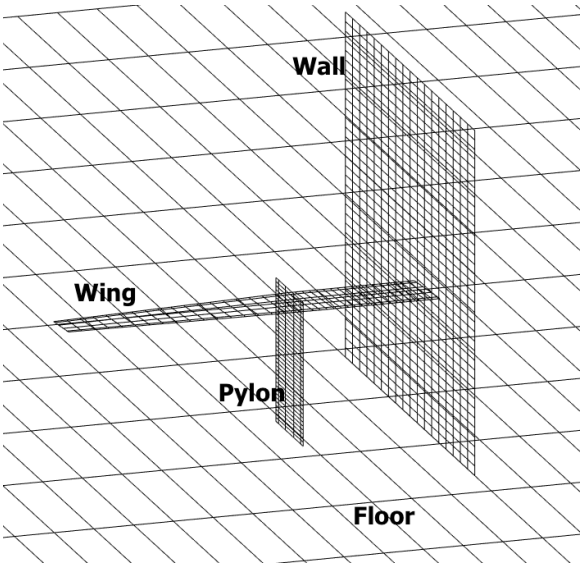

Figure 7.6: Representation of the setup of the wind tunnel experiment in the Adapted VLM model.

found when the circulation is calculated (see Section 5.5.3). This is used as an indication of the accuracy of the experimental data. From Figure 7.7 it is clear that the surfaces, besides the wing, in the wind tunnel setup influence the lift distribution of the wing. These surfaces are the pylon, wall and the floor. When these surfaces are modelled with the 'Adapted VLM - WT setup' the lift distribution on the wing is predicted within reasonable accuracy. Since the effect of the pylon,wall and floor cannot be ignored, the propeller-on cases are analysed only with the 'Adapted VLM - WT setup' model. Doing otherwise would not result in a valid comparison of the results.

7.2.2 Control Wing with Propeller-on

Figure 7.8 shows the lift distribution for the Control wing with propeller on. The zones of influence, mentioned in Subsection 2.1.1, are indicated as well. The propeller–wing interaction effects are clearly visible. With respect to the propeller-off case, the lift increases in zones W-I and W-II an decreases in zones W-III and W-IV. The agreement with the experimental results outside of the slipstream is good, while inside the lift is overpredicted. This indicates an oversimplification of the swirl recovery model. A swirl recovery factor (SRF) constant for the whole slipstream is used, while the result indicate a stronger swirl recovery occurs in zone W-II and a weaker one in zone W-III. The amount of swirl recovered is varies over the wing span, and should therefore be modelled as such.

The reason for such a strong difference between swirl recovery inboard and outboard of the propeller axis is because of the experiment setup. The wing was placed at $\alpha = 4$ deg, while the propeller was aligned with the incoming freestream velocity ($\alpha_p = 0$). Therefore, the wing section in zone W-II experiences a high local angle of attack and therefore a strong swirl recovery, while in zone W-III the wing experiences a low local angle of attack with a

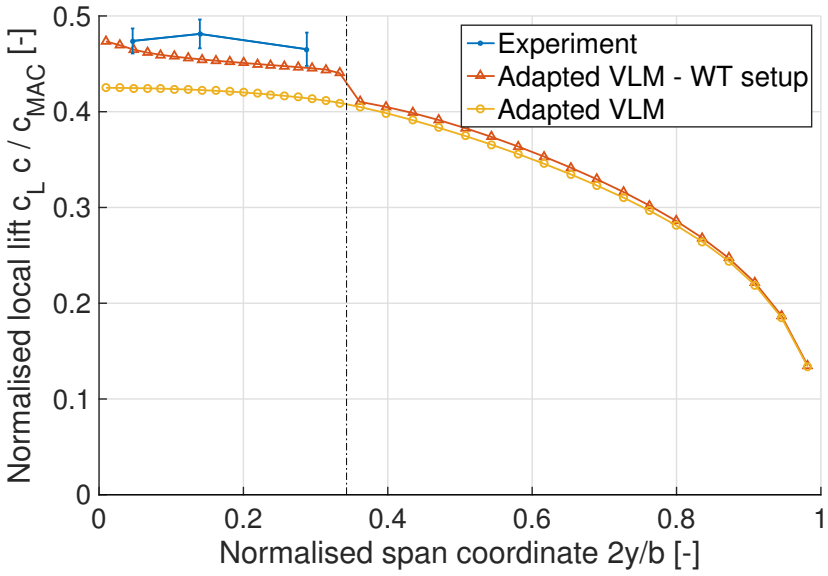

Figure 7.7: Lift distribution of the Control wing for the propeller-off case. Wind tunnel results are compared with the numerical models. 'Adapted VLM - WT setup' indicates the results with the Adapted VLM on the wind tunnel setup, instead of the wing and propeller-induced velocities only. The vertical dotted line indicates the spanwise location of the pylon.

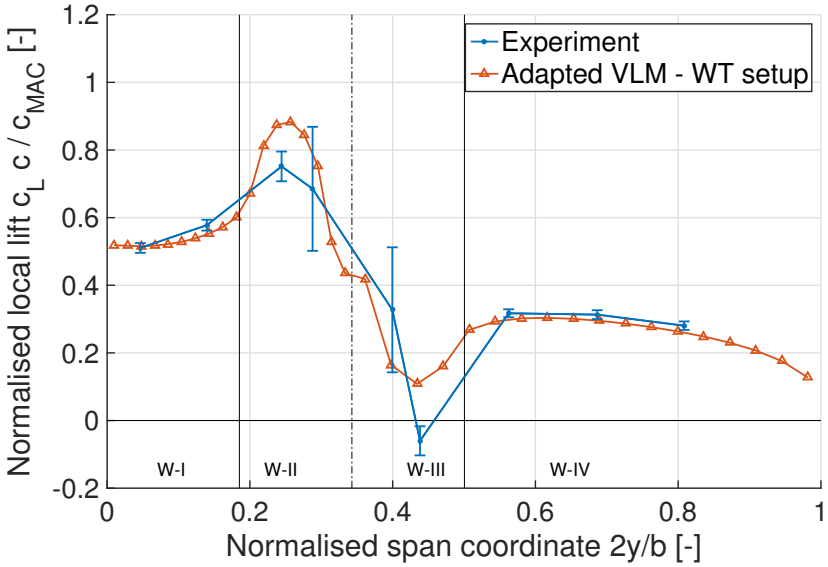

Figure 7.8: Lift distribution of the Control wing for the propeller-on case. Wind tunnel results are compared with the numerical models. 'Adapted VLM - WT setup' indicates the results with the Adapted VLM on the wind tunnel setup, instead of the wing and propeller-induced velocities only.

corresponding low swirl recovery.

7.2.3 Comparing the Control and Modified Wing

Figure 7.9 shows the lift and twist distribution for both the Control and Modified wing. The lift distribution measured on the Modified wing differs from that found the Control wing due to the changes in the twist angle. Outside of the slipstream they are explained by the changes in the wing twist. Inside the slipstream only small changes in the lift distribution are found even though the twist is decreased on this section of the wing. This can be explained by the increased lift in zone W-I, which leaves a trailing vortex on the boundary between zone W-I and W-II which induces an upwash on the wing section in zone W-II. In turn, this counteracts the effect of the decreased twist angle.

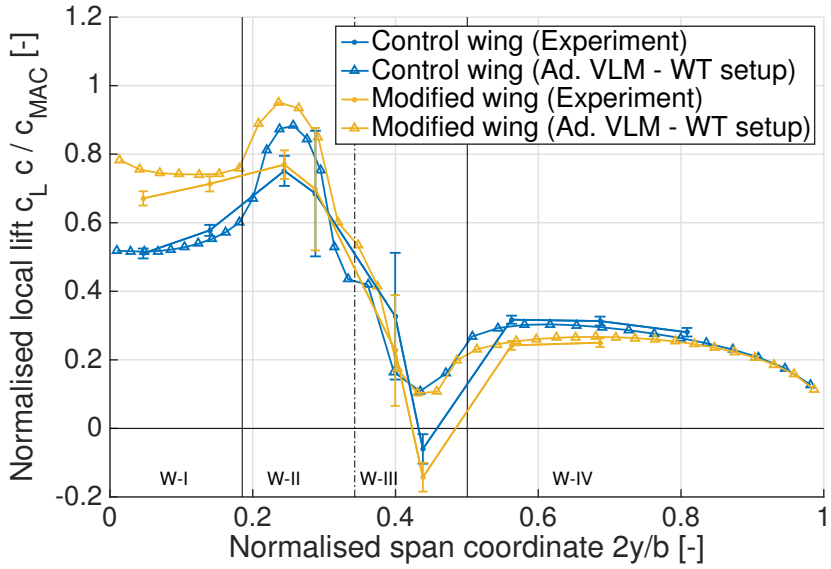

(a) Lift distribution

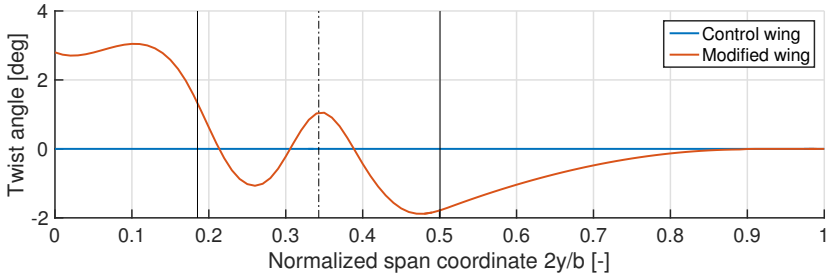

(b) Twist distribution

Figure 7.9: Lift and twist distribution of the Control wing compared with the Modified wing, for the propeller-on case. Wind tunnel results are compared with the numerical models. 'Adapted VLM - WT setup' indicates the results with the Adapted VLM on the wind tunnel setup, instead of the wing and propeller-induced velocities only.

The 'Adapted VLM -WT' setup model predicts the lift distribution of the Modified wing with

the accuracy as for the Control wing: outside of the slipstream the match with experimental results is good, inside the lift is overpredicted due to the oversimplified swirl recovery model. The differences in the lift distribution between the Modified and Control wing are captured well, especially outside of the slipstream. Inside the slipstream the absolute values of the lift distribution are incorrect. However, the relative changes between the lift distribution of the Control and Modified wing are captured reasonably well with the 'Adapted VLM-WT setup' model.

In conclusion, the Adapted VLM model has proven to predict the lift distribution with good accuracy outside of the slipstream, while inside the slipstream the absolute lift distribution is not capture correctly. The model is also accurate for predicting differences in lift distribution due to changes in the wing twist, especially outside of the slipstream. Even though, inside the slipstream the absolute lift distribution is captured accurately, the relative changes are. The last observation is important since in the optimisation process design changes are made continuously to find the optimum. Due to the inaccuracies in predicting the lift distribution inside the slipstream, the resulting wing design of an optimisation using this model might also contain inaccuracies. This means that qualitative design choices based on the results of the Adapted VLM are expected to be correct, while the absolute values of the resulting design can be inaccurate. For example, it is found that the twist angle of the wing section behind the upgoing blade must be decreased to find the best compromise between the local beneficial effect of the propeller-induced upwash and the local counteracting effect of the wing-induced downwash. This effect is considered to be accurate. The wing design resulting from an optimisation with the Adapted VLM model might say this twist angle must be -2 deg. This specific design value can be inaccurate and should be verified with higher-order numerical models or a wind tunnel experiment.

Chapter 8

Optimisation of the Wing Chord and Twist for Minimum Drag

This chapter uses the Adapted VLM model to optimise the wing chord and twist distribution. Section 8.1 explains the optimisation method used. Then the Control wing from the wind tunnel experiment is optimised, first for a matching lift with the analytic solution (in Section 8.2). Optimising the twist to obtain minimum induced drag is shown in Section 8.3. Finally, in Section 8.4 the chord and twist are optimised for minimum total drag.

8.1 Optimisation Method

The optimisation method used to optimise the chord and twist distribution of the wing is explained in this section, it is divided into stating the design variables and their bounds in Subsection 8.1.1 and the objective functions are given in Subsection 8.1.2.

8.1.1 Design Variables

The chord and twist distribution of the wing need to be varied to find the optimal design. This is done by defining the geometry of the wing as follows: The leading edge of the Control wing on the same straight line. The trailing edge is allowed to move according to the required local chord length. The local twist angle is applied around the line in spanwise direction through the quarter chord point at the root of the wing.

The local chord length and twist angle are varied during the optimisation to find the optimal combination of the chord and twist distribution. Two splines, one for the local chord length and one for the twist angle, control their distribution. Splines are defined by control points. The number of these control points define the number of degrees of freedom of the optimi-

sation. By using splines the number of degrees of freedom can be limited while the number of spanwise panels can be high to get accurate results with the numerical models. Typically the number of control points is in the order of 10 while the number of spanwise panels is 100. Another benefit of using splines is that the chord and twist distribution follow a continuous curve, which keeps the wing design reasonably smooth.

Bounds are applied to the local chord and twist angle. The chord is limited to prevent the design changes that might create problems for the structural design of the wing. Limitations to the twist are used to prevent unrealistic wing designs. The bounds are summarised in Table 8.1.

Table 8.1: Bounds to the local chord and twist angle. The chord of the initial wing is represented by c_0

Parameter	Symbol	Lower bound	Upper bound
Local chord	c	$0.75 \cdot c_0$	$1.5 \cdot c_0$
Local twist angle	θ	-10 deg	10 deg

8.1.2 Objective Functions

Three different objective functions for optimisation are used in this thesis:

- Lift matching with the optimal lift distribution.
- Minimise the induced drag with constant lift.
- Minimise the total drag with constant lift.

The lift matching is done as follows: the optimal lift distribution is gotten from the analytical method, AN, while the wing is analysed with the Adapted VLM or Adapted LL method to get the actual lift distribution. During the optimisation the wing chord and/or twist distributions are changed in order to get the actual lift distribution equal to the optimal one. The cost function to minimise is given by:

$$f_{\text{lift matching}} = \varepsilon_{lift} = \sum_{n} \left(l(n) - l_{optimal}(n)\right)^2 \tag{8.1}$$

Which states that the error is calculated as the difference between the actual lift distribution and the optimal one, the difference is squared and then summed over every station n along the span of the wing.

The minimisation of the induced and total drag is performed by analysing the wing with the Adapted VLM or Adapted LL to get the lift and drag values. Then the wing chord and/or

twist distributions are changed in order to minimise the drag (induced or total) while keeping the lift equal to that of the original wing.

The problem is solved by a gradient-based optimisation, which follows the local gradient down towards a local minimum. In order to ensure this is also the global minimum the same optimisation can be performed with different initial conditions. This is employed by taking the optimised wing from the first optimisation, mirroring the twist and inverting the chord distribution (root chord becomes tip chord) for the new initial wing for the second run of the optimisation. The optimisation is performed with the Matlab® function *fmincon*.

8.2 Lift Matching with Optimum Lift Distribution

The Modified wing was designed with the lift matching optimisation. The methods used for the optimisation were the AN for the optimal lift distribution and the VLM-SI for the actual lift. The last method uses an oversimplified model for the propeller induced velocities, the slipstream model SI, which models the velocities as their far downstream values. This neglects slipstream contraction, the development of the axial velocity, effect of swirl recovery and the deformation of the slipstream by the propeller inclination and wing upwash and downwash (see Section 3.4). At the time the more realistic slipstream model SV, which does account for the effects mentioned, was not available. Analysis with the method VLM-SV shows that the lift distribution of the Modified wing was not equal to the optimal one.

The lift matching optimisation is performed again with the VLM-SV method for the actual lift distribution, to create the Lift matched wing. Figure 8.1 shows the lift (a) and twist (b) distribution of the Control, Modified and Lift matched wings. As can be seen the lift distribution of the Lift matched wing is equal to the optimal lift distribution, in contrast to the Control and Modified wing.

The lift and induced drag of the three wings is presented in Table 8.2. The Modified and Lift matched wing were designed to have the same lift as the Control wing. While this is this is actually true for the Lift matched wing, the Modified wing has a slightly larger lift. This is because the Modified wing was designed using a different analysis method, the lift is equal when the VLM-SI method is used, but with the current VLM-SV this is not the case. The table also shows that the Modified and Lift matched wings are not the optimal designs since they have a higher induced drag than the Control wing. For the Modified wing this is expected since it does not have the optimal lift distribution. The fact that the Lift matched wing is actually performing worse indicates that the analytical method AN does predict the optimal lift distribution correctly. The reason for this lies in the propeller induced velocities on the wing. The AN method assumes these velocities can be taken as the far downstream values, while the VLM-SV models the velocities to account for slipstream contraction, development of axial velocity, effect of swirl recovery and the deformation of the slipstream due to the propeller inclination and wing induced velocities. In other words the assumption in the analytical method AN that the propeller and wing can be modelled very far apart, such that the influence of the wing on the propeller does not have to be modelled, is incorrect.

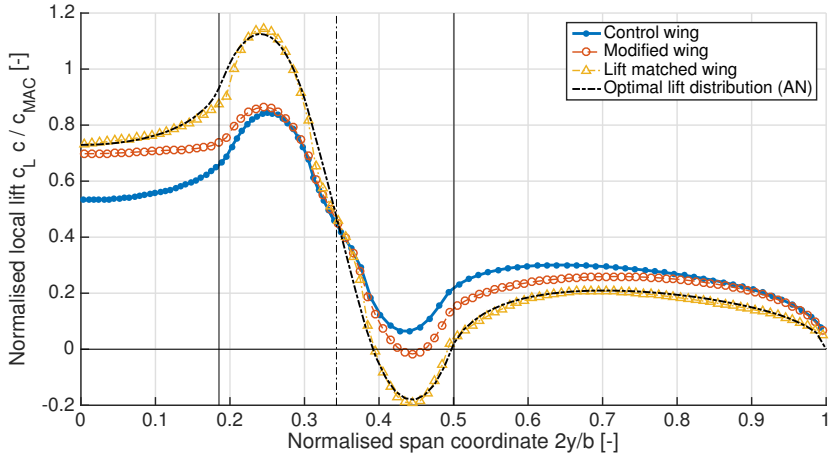

(a) Lift distribution

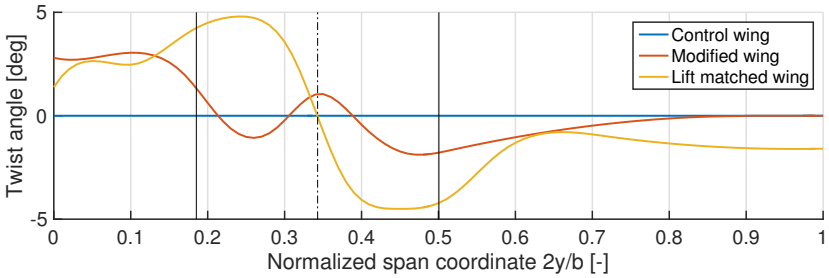

(b) Twist distribution

Figure 8.1: Lift and twist distribution of the Control, Modified and Lift matched wings compared to the analytical optimal lift distribution, for wind tunnel experiment operating conditions.

Table 8.2: Lift and induced drag coefficients for the Control and Modified wings at wind tunnel experiment operating conditions. The term $\Delta C_{D_{ind}}$ represents the difference in induced drag with respect to the Control wing.

Wing	C_L	$C_{D_{\mathbf{ind}}}$	$\Delta C_{D_{\mathbf{ind}}}$
Control wing	0.384	-0.01056	-
Modified wing	0.391	-0.01001	0.00055
Lift matched wing	0.382	-0.00487	0.00569

8.3 Optimise Twist of Control Wing for Minimum Induced Drag

The twist distribution of the Control wing is optimised for minimum induced drag, while keeping the lift and chord distribution constant. The operating conditions of the wing are the same as used in the wind tunnel experiment. The optimised wing is called Minimum induced

drag wing. Table 8.3 shows the lift and induced drag coefficient, as well as the difference in induced drag coefficient with respect to that of the Control wing. As can be seen the Minimum induced drag wing has an induced drag coefficient that is 7 drag counts lower than that of the Control wing (one drag count is $\Delta C_D = 0.0001$). This shows the optimisation successfully reduced the induced drag of the Minimum induced drag wing.

Table 8.3: Lift and induced drag coefficients for the Control and Minimum induced drag wing at the wind tunnel experiment operating conditions. The subscript Cw indicates induced drag coefficient of the Control wing is considered.

Wing	C_L	$C_{D_{\mathbf{ind}}}$	$C_{D_{\text{ind}}} - C_{D_{\text{ind Cw}}}$
Control wing	0.384	-0.01056	-
Minimum induced drag wing	0.384	-0.01126	-0.00070

The twist, lift and induced drag distribution of the Minimum induced drag wing are shown in Figure 8.2. A number of observations can be made in these figures, which explain how the reduction in induced drag is realised. The wing is divided into four zones as shown in Figure 8.2(a) (similar as in done in Subsection 2.1.1). In the following discussion, unless otherwise mentioned the changes mentioned are with respect to the Control wing.

- The changes in the lift distribution follow the changes in the twist distribution. The twist increase in zone W-I causes the lift to increase in the same zone, the same is true in zone W-III, while in zone W-IV the lift is decreased due to the lower twist angle. In zone W-II the lift stays approximately the same, even though the twist is decreased on this section of the wing. This is because of the lift increase in zone W-I, which results in a trailing vortex around the inboard edge of the slipstream. This vortex induces an upwash in zone W-II, which apparently cancels the twist decrease effect on the lift distribution.
- Figure 8.2(b) shows a reduction in the induced drag is found behind the propeller-induced upwash in zone W-II. This is interesting because the twist angle in this region is decreased and the lift approximately the same as for the Control wing. The propeller-induced upwash is counteracted by the wing-induced downwash (as also discussed in Section 8.2 and investigated in Appendix F). In this zone the wing-induced downwash is lower with respect to the Control wing because of the increased lift in zone W-I. The net result is a locally reduced induced drag for the Minimum induced drag wing.
- A reduction of the induced drag is also found on the outboard wing, in zone W-IV. This is a direct consequence of the reduced lift on this part of the wing.
- In order to keep the integral lift constant the local lift is increased in zones W-I and W-III, which causes the induced drag to increase in these zones as well.
- The lift distribution of the Minimum induced drag wing is very different from the lift distribution predicted by the Adapted AN method. Section 8.2 already showed that this method does not produce a wing design that has a lower induced drag. In Figure 8.2(a) it is clear that the resulting lift distribution from the Adapted AN is actually very different from the optimal lift distribution for minimum induced drag.

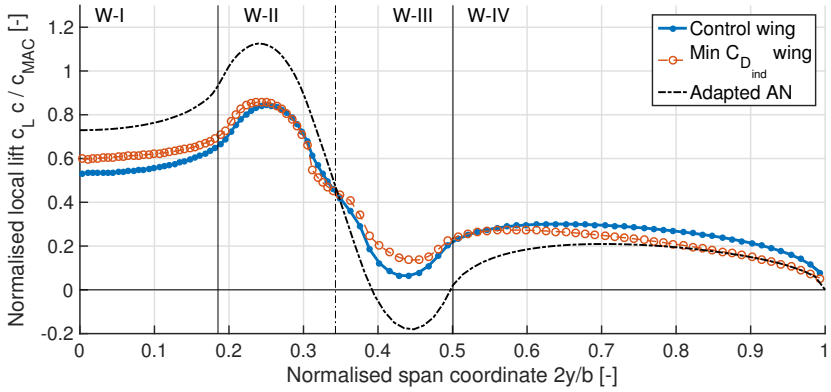

(a) Lift distribution

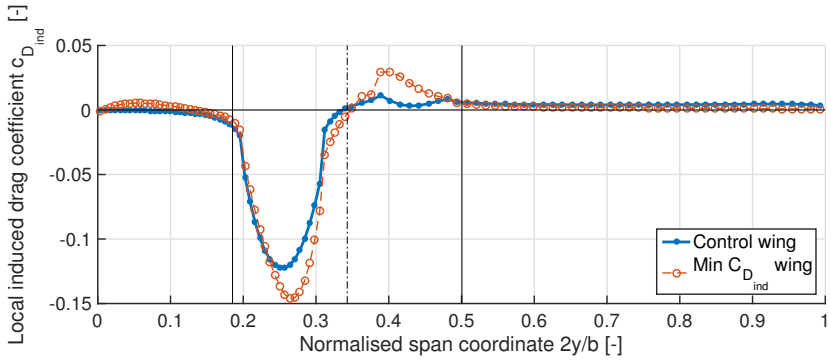

(b) Induced drag distribution

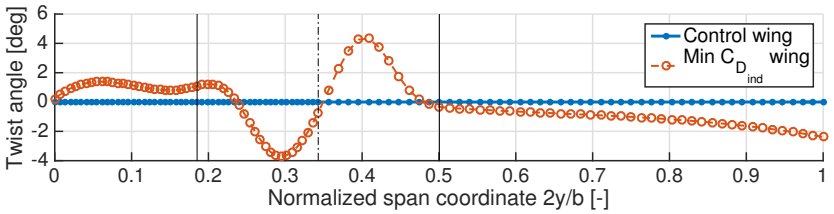

(c) Twist distribution

Figure 8.2: Lift, induced drag and twist distribution of the Control and Minimum Induced drag wings, for wind tunnel experiment operating conditions.

8.4 Optimise Chord and Twist of Control Wing for Minimum Total Drag

The chord and twist distribution of the Control wing are optimised for minimum total drag, while keeping the lift constant. The operating conditions of the wing are the same as used in the wind tunnel experiment. The optimised wing is called Minimum total drag wing. Since

the chord distribution, and therefore surface area, of the Minimum total drag wing is changed the use of coefficients for the lift, induced drag and total drag is not sufficient to capture all the differences between the wings. Therefore, Table 8.4 shows the lift, induced drag and total drag as percentage difference with respect to their values for the Control wing. As is clear from the table the Minimum total drag wing as a 34.6% lower total drag than the Control wing. This indicates that the optimisation of the chord and twist distribution can successfully reduce the total drag. The induced drag is reduced with 14.5%, which a stronger reduction with respect to the Minimum induced drag wing. The additional freedom of changing the chord distribution, compared to only the twist distribution, gives the opportunity to reduce the induced drag even more.

Table 8.4: Differences in the lift, induced drag, and total drag with respect to those of the Control wing, displayed as percentages of their values of the Control wing. The subscript Cw indicates the lift or drag of the Control wing is considered.

Wing	$\frac{L-L_{\mathrm{Cw}}}{\lvert L_{\mathrm{Cw}}\rvert}$	$\frac{D_{\mathrm{ind}}-D_{\mathrm{ind\ Cw}}}{\lvert D_{\mathrm{ind\ Cw}}\rvert}$	$\frac{D_{\mathrm{tot}}-D_{\mathrm{tot\ Cw}}}{\lvert D_{\mathrm{tot\ Cw}}\rvert}$
Control wing	0 %	0 %	0 %
Minimum induced drag wing	0 %	-6.7 %	-5.9 %
Minimum total drag wing	0 %	-14.5 %	-34.6 %

Figure 8.3 shows the wing planform and twist distribution for the Control, Minimum induced drag and Minimum total drag wings. As can be seen in figure 8.3(a) the chord distribution of the Minimum total drag wing is changed, it actually reaches the lower chord bound on the outboard wing and the upper chord bound at the wing root. The twist, depicted in Figure 8.3(b), of the Minimum total drag wing is different from the Minimum induced drag wing, although it does show a somewhat similar trend. The direction of the twist change with respect to the Control wing is the same in zones W-I to W-III. Only in zone W-IV, the twist of the Minimum total drag wing is not decreased, while this is the case for the Minimum induced drag wing.

Figure 8.4 shows the lift and total drag distribution. They are not made non-dimensional because of the different surfaces areas of the wing. Using coefficients is this case would make interpreting the results more difficult. Even though the twist distributions of the Minimum total drag and Minimum induced drag wings are not the same, their lift distributions (shown in Figure 8.4(a)) on large parts of the wing actually are. This is due to the changes in the chord distribution.

When compared to the Control wing, the Minimum total drag wing shows the following differences in total drag distribution (see Figure 8.4(b)):

- In zone W-I the peak in the total drag occurs at the wing root, this is due to the large increase of the wing root chord.
- Zone W-II shows a reduction of the total drag with respect to the Control wing. The cause of this reduction lies in the induced drag component and is similar as explained for the Minimum induced drag wing in Section 8.3.

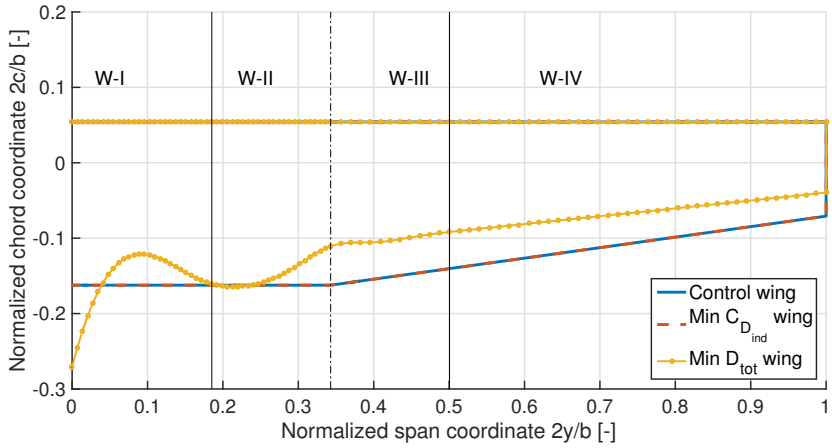

(a) Wing planform

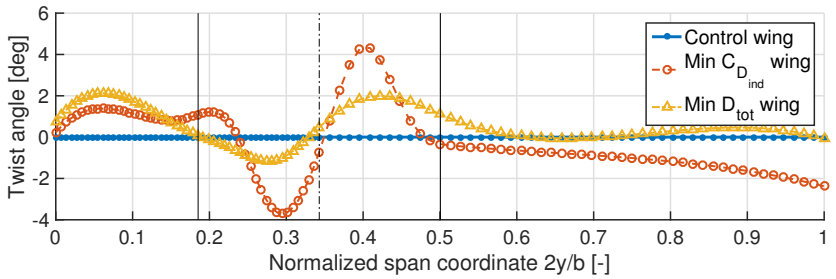

(b) Twist distribution

Figure 8.3: Wing planform and twist distribution of the Control and Minimum total drag wings.

- No significant differences are observed in zone W-III.
- In zone W-IV both the induced and viscous drag are reduced. The induced drag the same reason as explained for the Minimum induced drag wing: a lower lift on this wing section. The reduced viscous drag is caused by the smaller wing chords. The reduction, even together, is small and difficult to see in the Figure. However, the reduction is real and substantial when integrated over the whole span of the wing section.

With respect to the Minimum induced drag wing these are the differences:

- In zone W-I the total drag is lower in general except for the peak at the wing root. Both effects are explained by the change in wing chord in the section.
- Zone W-II shows a small increase of the total drag. This is related to the larger (less negative) twist angle. Even though the lift on both wings in this section is approximately equal, the fact that a larger twist angle is necessary to keep it this way indicates a larger wing-induced downwash is present. As found earlier the wing-induced downwash locally counteracts the propeller-induced upwash which causes the induced drag to increase.

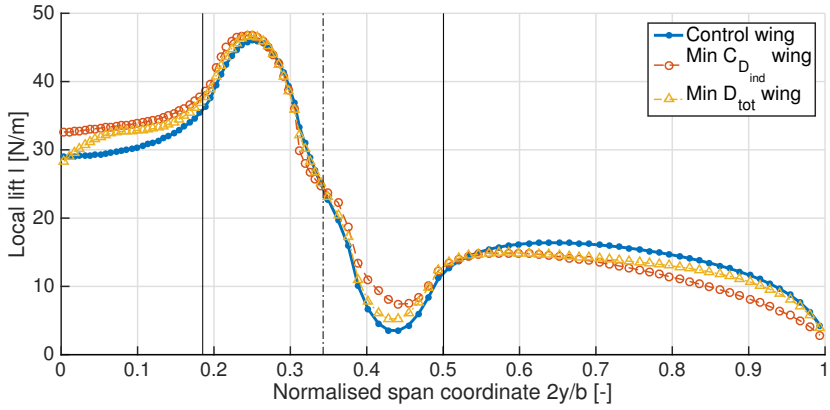

(a) Lift distribution

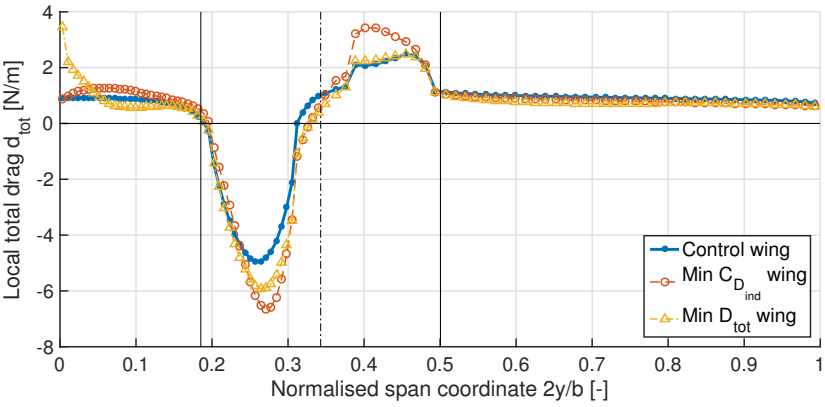

(b) Total drag distribution

Figure 8.4: Lift, total drag and twist distribution of the Control and Minimum total drag wings, for wind tunnel experiment operating conditions.

- The wing chord in zone W-III is smaller for the Minimum total drag wing, which causes a decrease in the local viscous drag. This is the main reason for the lower total drag found in this zone.
- In zone W-IV a smaller wing chord is also the reason for a lower viscous drag and therefore total drag.

Chapter 9

Conclusions and Recommendations

This chapter presents the conclusions and recommendations derived from all the content of this report. They are discussed in Section 9.1 and Section 9.2, respectively.

9.1 Conclusions

Even though propellers are the oldest form of propulsion in aviation, propeller aircraft are still used today. The superior efficiency of propellers over jet engines is an important benefit in certain market segments. This is true for small aircraft in general aviation, passenger aircraft flying the shorter/regional routes and for the increasing market of Unmanned Aerial Vehicles (UAVs). This thesis focusses on the aircraft with two wing-mounted propellers. These aircraft experience strong propeller–wing interactions which affects the aerodynamic performance of the vehicle. This performance is of course crucial for the always important challenge to reduce fuel consumption (and therefore operating costs) or increase endurance or range.

The research objective was to validate and apply low-order numerical models, adapted to include propeller–wing interaction effects, for the optimisation of the wing chord and twist distribution in a tractor propeller configuration. Low-order models are used, in contrast to higher-order ones, since they have short execution times, which are required for optimisation. Propeller–wing interaction is of an unsteady nature, however, it is shown in literature that for design purposes considering only the time-averaged effects is sufficient. These time-averaged effects can be put into two categories: the effect of the propeller on the wing and the effect of the wing on the propeller and its slipstream. The effects in the first category are captured with a Lifting Line and Vortex Lattice Method, both adapted to include the effect of the propeller-induced velocities on the wing, respectively called Adapted LL and Adapted VLM. The effects in the second category are modelled with a propeller analysis tool (XROTOR) and a combination of slipstream models. These slipstream models are for the slipstream contraction, deflection, axial development of the axial velocity and swirl recovery. The Adapted LL and VLM models use XROTOR and the slipstream models for the propeller-induced velocities on

the wing. Two corrections are applied in these combinations of models: a swirl recovery factor (SRF) is applied to the propeller-induced tangential velocity and the axial velocity component of the propeller-induced velocities is removed from the equation for the lift ($l = \rho\Gamma(V_\infty + u_w)$ instead of $l = \rho\Gamma(V_\infty + u_w + u_p)$). Next to these models, an analytic solution for the optimal lift distribution for minimum induced drag is implemented and is referred to as the AN.

The validation and application of these models is discussed in Subsection 9.1.1 and 9.1.2, respectively.

9.1.1 Validation

The implementation of the Adapted LL and VLM models is validated with existing experimental data from a wind tunnel test on a propeller–wing combination. In general both models show good agreement with the experimental results for the integral lift, lift distribution and the approximated induced drag. It is also shown that the Adapted VLM provides better predictions of the lift distribution with respect to the Adapted LL. The propeller thrust and torque prediction capabilities of XROTOR is validated with another set of existing experimental results for a propeller.

In order to validate the Adapted LL and VLM for predicting changes in the lift distribution due to changes in the wing twist distribution, a wind tunnel experiment was performed. The experiment involved two almost identical wings, only different in their twist distribution, which were placed downstream of a propeller. The velocity fields around the wing and of the propeller slipstream were measured using planar particle-image velocimetry (PIV). Additionally, total and static pressure measurements were performed to characterize the propeller slipstream.

The velocity fields show expected qualitative behaviour of the flow. For the propeller slipstream the increase in axial velocity, contraction and axial development are observed. The flow around the wing shows an increase of velocity over the wing and a decrease on the lower side. Furthermore, the streamlines are observed to deflect downwards more when the local wing twist angle is increased. And inside the slipstream the propeller-induced upwash and downwash are clearly noticeable.

The propeller slipstream velocity fields are used to validate the slipstream models for contraction, deflection, axial velocity and its axial development. With respect to the model, the slipstream is observed to have a stronger contraction to start with and a slower continued contraction moving downstream. The same is true for the axial velocity of the slipstream. Two differences between the model and the real situation can be the explanation for this error: the nacelle is not modelled and the model assumes a constant blade loading (which is not the case). Slipstream deflection in front of the wing is modelled well, while behind the wing the deflection downwards is overpredicted. This is likely the result of modelling the deflection is two discrete changes in the slipstream deflection angle, one a the propeller plane and one at the wing quarter chord point. The propeller thrust is estimated based on the pressure measurements and the axial velocity found in the velocity fields by assuming a circumferentially

averaged blade loading. The propeller thrust is overpredicted by XROTOR with 15 %. Even though the slipstream models are not perfect, the propeller-induced velocities are modelled in the right order of magnitude, direction and approximate location on the wing. Therefore, the slipstream models are found to be validated for their use in the Adapted VLM model.

The velocity fields around the wing are used to determine the local lift. The lift distribution is predicted reasonably well by the Adapted VLM, both for the isolated wing as well as with propeller on. The expected changes in lift distribution due to changes in twist distribution are predicted in the correct direction and with similar magnitude. However, inside the slipstream the predicted lift distribution does not fall within the measurement error. Both in the propeller-induced upwash and downwash the lift is overpredicted, which indicates an error in the modelling of the swirl recovery. It seems that the swirl recovery for the propeller-induced upwash region is underestimated, while for the propeller-induced downwash it is overestimated. The swirl recovery is modelled to be equal for the whole of the slipstream, which might be an oversimplification.

Although the Adapted VLM model contains inaccuracies in predicting the lift and drag distributions, it does follow the correct trend in the lift and drag distribution on one wing as well as the changes between two different wings. It can therefore be used for optimisation studies, as long as the results are carefully interpreted. This means that qualitative design choices based on the results of the Adapted VLM are expected to be correct, while the absolute values of the resulting design can be inaccurate. For example, it is found that the twist angle of the wing section behind the upgoing blade must be decreased to find the best compromise between the local beneficial effect of the propeller-induced upwash and the local counteracting effect of the wing-induced downwash. This effect is considered to be accurate. The wing design resulting from an optimisation with the Adapted VLM model might say this twist angle must be -2 deg. This specific design value can be inaccurate and should be verified with higher-order numerical models or a wind tunnel experiment.

9.1.2 Application

The Adapted VLM is used for optimisation of the wing chord and twist distribution. The Control wing is optimised with three different optimisation objective functions. The chord was bound to be within 75% and 150% of the original chord length and the lift is constrained to stay constant.

- Lift matched wing, by varying the wing twist to match the wing lift distribution with the optimal lift distribution predicted for that wing by the Adapted AN model.
- Minimum induced drag wing, by varying the wing twist distribution to minimise the induced drag.
- Minimum total drag wing, by varying the wing twist and chord distribution to minimise the total drag.

Analysis with the Adapted VLM shows that the induced drag of the Lift matched wing is 57

drag counts higher than that of the Control wing (1 drag count is $\Delta C_D = 0.0001$). Therefore, the Adapted AN model does not correctly predict the optimal lift distribution for minimum induced drag. This model does not use any of the slipstream models, which is expected to be the reason for this error.

The Minimum induced drag wing does show a small decrease of the induced drag (7 drag counts) with respect to the Control wing. The induced drag reduction is realised in two locations on the wing: One, on the wing section in the propeller-induced upwash by decreasing the twist angle (lowering the local angle of attack). On this section the local wing-induced downwash is counteracting the propeller-induced upwash. The optimum between these two is found, in this case, by reducing the local angle of attack.

A strong drag reduction (34.6%) is found for the Minimum total drag wing. Since the chord distribution and therefore surface area of this wing has changed the use of drag coefficients is not sufficient to capture the differences between the wings. The wing twist distribution of this wing follows the same trend as for the Minimum induced drag wing, only with smaller amplitudes. This is possible due to the changes in the wing chord distribution. Together they result in a lift distribution that is almost equal to that of the Minimum induced drag wing. The drag reduction is realised by a combination of reducing the induced drag and viscous drag. Similarly as for the Minimum induced drag wing, the reductions are found in the propeller-induced upwash region and the outboard section of the wing.

To conclude, the Adapted VLM model is validated for predicting changes in the lift distribution due to changes in the wing twist. The model is then successfully used to study the optimum wing chord and twist distribution for minimum induced/total drag, which showed for example the compromise between propeller-induced upwash and wing-induced downwash. Even though the result should be carefully interpreted, the model is ready to be used on a real aircraft wing in order to determine the how much drag reduction is really possible.

9.2 Recommendations

Based on a number of observations made during this thesis the following recommendations are made:

- Optimise the wing of an actual aircraft to determine what reduction of the drag is possible to achieve for a situation that is representative for a real life situation (in contrast to the Control wing at the operating conditions used in this thesis).
- Perform an experiment in order to definitively confirm (or deny) the use of this equation for the lift: $l = \rho \Gamma V_\infty$. This could be done with an experiment on a propeller–wing combination with both measurement with pressure taps in the wing and PIV measurement of the flow around the wing, both at the same location. The pressure taps provide the actual lift and the circulation can be determined in the velocity field acquired by the PIV measurement.
- Swirl recovery is an effect that varies in strength along the wingspan, it should be

modelled such that it can vary in this direction (as mentioned in Subsection 7.2.2).

- Develop a numerical model based on a vortex lattice method or lifting line, including the propeller blades and their wake. This will definitely increase the execution time of the model, however the more advanced modelling of the propeller-wing interactions, and especially the effect of the wing on the slipstream (or propeller wake), might give valuable insights in how to make a simplified but physically more accurate model for the swirl recovery.
- The same exercise could also shine a light on the correction made to the lift equation mentioned in Subsection 3.3.2 and Appendix A.
- The slipstream models could be improved by doing one or more of the following: base the contraction model on the actual propeller blade loading, include the effects of the nacelle, model the slipstream deflection due to the wing upwash and downwash in a continuous manner (instead of two discrete changes).

Bibliography

[1] L. R. Miranda and J. E. Brennan, "Aerodynamic effects of wing-tip mounted propellers and turbines," *American Institute of Aeronautics and Astronautics*, vol. 86-1802, pp. 221–228, 1986.

[2] I. Kroo, "Propeller-Wing Integration for Minimum Induced Loss," *Journal of Aircraft*, vol. 23, no. 7, pp. 561–565, 1986.

[3] L. L. M. Veldhuis, *Propeller wing aerodynamic interference*. PhD thesis, Delft University of Technology, 2005.

[4] B. R. Rakshith, S. M. Deshpande, R. Narasimha, and C. Praveen, "Optimal Low-Drag Wing Planforms for Tractor-Configuration Propeller-Driven Aircraft," *Journal of Aircraft*, vol. 52, no. 6, pp. 1791–1801, 2015.

[5] C. Alba, "A Surrogate-Based Multi-Disciplinary Design Optimization Framework Exploiting Wing- Propeller Interaction," tech. rep., Delft University of Technology, Delft, 2017.

[6] J. Cho and J. Cho, "Quasi-steady aerodynamic analysis of propeller-wing interaction," *International Journal for Numerical Methods in Fluids*, vol. 30, no. 8, pp. 1027–1042, 1999.

[7] I. Gonzalez-Martino, M. Costes, B. Rodriguez, and P. Devinant, "Application of an Unsteady Curved Lifting-Line Theory to Propeller Simulations," *AIAA Applied Aerodynamics Conference*, vol. 30th, no. June, 2012.

[8] D. P. Witkowski, R. T. Johnson, and J. P. Sullivan, "Experimental Results of a Propeller/ Wing Interaction Study," *SAE*, vol. 910998, 1991.

[9] J. D. J. Anderson, *Fundamentals of Aerodynamics*, vol. 3rd Editio. New York: McGraw-Hill, 3rd ed., 2001.

[10] S. Miley, "On the design of airfoils for low Reynolds numbers," *Archive Set 115*, 1963.

[11] M. M. Munk, "The Minimum Induced Drag of Aerofoils," *NACA Report*, vol. 121, 1921.

[12] I. H. Abbott and A. E. van. Doenhoff, *Theory of Wing Section*. New York: Dover Publications, Inc, 2nd ed., 1959.

[13] T. Melin, "A Vortex Lattice MATLAB Implementation for Linear Aerodynamic Wing Applications," tech. rep., Royal Institute of Technology (KTH), Stockholm, 2000.

[14] W. F. Phillips and D. O. Snyder, "Modern adaptation of Prandtl's classic lifting-line theory," *Journal of Aircraft*, vol. 37, no. 4, pp. 662–670, 2000.

[15] M. Drela, "XFOIL: An Analysis and Design System for Low Reynolds Numer Airfoils," in *Low Reynolds Number Aerodynamics. Springer-Verlag. Lecture Notes in Engineering*, vol. 54, pp. 1–12, 1989.

[16] M. Drela, "XROTOR," 2003.

[17] N. van den Dungen, "Synthesis of an Aircraft Featuring a Ducted-Fan Propulsive Empennage," tech. rep., Delft University of Technology, Delft, 2017.

[18] S. Goldstein, "On the Vortex Theory of Screw Propellers," *Proceedings fo the Royal Society of London. Series A*, vol. 123, no. 792, pp. 440–465, 1929.

[19] J. T. Conway, "Analytical solutions for the actuator disk with variable radial distribution of load," *Fluid Mechanics*, vol. 297, pp. 327–355, 1995.

[20] J. De Young, "Propeller at High Incidence," *Journal of Aircraft*, vol. 2, no. 3, pp. 241–250, 1965.

[21] M. Drela and H. Youngren, "Athena Vortex Lattice (AVL)," 2007.

[22] NLR, "N250 propeller shoptest," tech. rep., National Aerospace Laboratory, Amsterdam, 1993.

[23] "The Open Jet Facility," 2016.

[24] ATR, "ATR 42-600 Brochure."

[25] ATR, "ATR 72-600 Brochure."

[26] Fokker Services, "Fokker 50 - Basics."

[27] J. D. Errico, "inpaint_nans - File Exchange - MATLAB Central - Accessed on 2017-02-19," 2012.

[28] M. Raffel, C. Willert, S. Wereley, and J. Kompenhans, *Particle Image Velocimetry*. Springer, 2nd ed., 2007.

[29] B. W. Mccormick, *Aerodynamics, Aeronautics and Fligth Mechanics*. New York: John Wiley & Sons, inc, 2nd ed., 1995.

[30] J. van Kuijk, "Analysis of Swirl Recovery Vanes," tech. rep., 2015.

Appendix A

Investigation of Vortex Lattice Method Formulation

The formulation of the equations used for the adapted Vortex Lattice Method (VLM) is investigated in this Appendix. Two different formulations are compared with result from the experiment performed by Veldhuis (3). This experiment consisted of a wing with a wing mounted propeller in tractor configuration and was tested in the Low Turbulence Tunnel (LTT) of the Delft University of Technology (see Figure A.1). The experimental results shown here are from pressure tap measurements in the wing surface. For more details on the experimental setup the reader is referred to the (3).

Although no formula is presented with which the pressure coefficient is calculated form the pressure measurements it is assumed the standard definition (9) is used:

$$C_P \equiv \frac{p - p_\infty}{q_\infty} \tag{A.1}$$

Which means the pressure difference is made dimensionless with the freestream dynamic pressure.

The same is assumed for the lift coefficient:

$$C_l = \frac{2l}{\rho V_\infty^2 c} \tag{A.2}$$

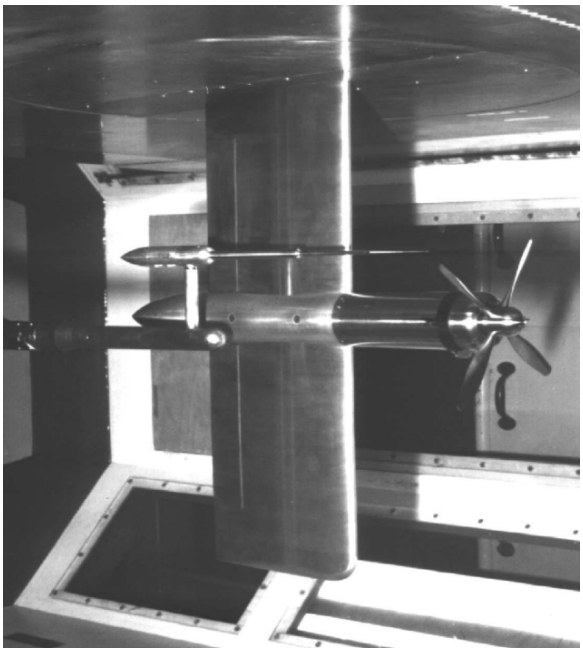

Figure A.1: Wind tunnel experiment on the PROWIM model by Veldhuis (3).

A.1 The Adapted Vortex Lattice Method

In a Vortex Lattice Method the wing is modelled with a number of panels. All these panels have a corresponding horseshoe vortex with a certain circulation strength Γ. This horseshoe vortex induces a certain velocity distribution on the complete flowfield following the the Biot-Savart law:

$$\mathbf{dV} = \frac{\Gamma}{4\pi}\frac{\mathbf{dl}\times\mathbf{r}}{|\mathbf{r}|^3} \tag{A.3}$$

On every panel there should be no flow through the panel, or in other words the normal velocity on the panel should be zero. This condition is used to determine the strength of all the horseshoe vortices. The velocity to consider for the adapted VLM is the total velocity (including the propeller induced velocities):

$$\mathbf{V} = \mathbf{V}_\infty + \mathbf{V}_{wing} + \mathbf{V}_{prop} \tag{A.4}$$

When the strengths of all the vortices are known the force is calculated with:

$$\mathbf{dF} = \rho\Gamma\mathbf{V}\times\mathbf{dl} \tag{A.5}$$

This is a vector interpretation of the Kutta-Joukowski theorem given by Phillips and Snyder (14). The result of this equation is a local force vector (in Newton per meter) and can be decomposed into the lift, induced drag and a spanwise force.

A.2 Correct Definition for the Velocity

Now it would be intuitive to use the same definition for the velocity in this equation as is used to determine the circulation, namely the local total velocity (including the freestream, wing and propeller induced velocities). However, using this definition results in a highly overestimated lift inside the slipstream. This can be seen in Figure A.2. This figure shows the lift distribution on the PROWIM wing for experimental and numerical results. The numerical results are calculated based on the following:

- The circulation is determined using the local and total velocity ($V = V_\infty + V_{wing} + V_{prop}$).
- Then the forces are calculated using Equation A.5. In this equation the definition of the velocity V is varied.

Since the first, and intuitive, definition of the velocity gives results that do not match with the experimental results other definitions are tried in order to find a better model. In total three options are modelled:

1. All propeller induced velocities are added ($V = V_\infty + V_{wing} + V_{prop}$).
2. None of the propeller induced are added ($V = V_\infty + V_{wing}$).
3. Only the tangential velocities are added ($V = V_\infty + V_{wing} + V_{prop,tangential}$).

To show in a more intuitive way what the effect is of these options Equation A.5 is expanded for a wing with no taper, sweep or dihedral (this assumes the vector **dl** only has a component along the span of the wing). Table A.1 shows the equations for lift and induced drag for the different velocity definition options.

Table A.1: The effect of different definitions of velocity in Equation A.5 on the equation for lift and induced drag.

Velocity option	Lift	Induced drag
1	$l = \rho\Gamma\left(V_\infty + u_{wing} + u_{prop}\right)$	$d_{ind} = -\rho\Gamma\left(w_{wing} + w_{prop}\right)$
2	$l = \rho\Gamma\left(V_\infty + u_{wing}\right)$	$d_{ind} = -\rho\Gamma w_{wing}$
3	$l = \rho\Gamma\left(V_\infty + u_{wing}\right)$	$d_{ind} = -\rho\Gamma\left(w_{wing} + w_{prop}\right)$

Again look at Figure A.2, here it is clearly seen that options 2 and 3 show a much better agreement with the experimental results. The resulting lift distribution for options 2 and 3 are the same since both models do not take the propeller axial velocity into account which is main driver for the lift to be overestimated by option 1.

The difference between options 2 and 3 becomes clear for the induced drag distribution, shown in Figure A.3. Removing the effect of the tangential components of the propeller induced velocities (the non axial components) completely changes the behaviour of the induced drag inside the slipstream. This is because the induced drag is modelled as the lift times the local induced angle of attack. And the propeller up or downwash has a very large effect on this angle.

The induced drag cannot be compared to experimental results as these are not available. However, based on the expected behaviour of the induced drag one of the options can be chosen. The induced drag inside the slipstream is expected to change as follows due to the up and downwash of the propeller.

First consider how induced drag on a wing without the effects of a propeller is defined. For this consider a small spanwise section of the wing. Locally this part of the wing produces a lift force perpendicular to the local flow direction. Due to the downwash created by the trailing vortices behind the wing this local flow direction is changed somewhat. More specifically the extra downwash reduces the local angle of attack. Therefore the lift vector points a bit rearward. In the frame of reference of the freestream the local force can now be decomposed into a lift and a induced drag force.

Now consider the effects of the propeller. Behind the upgoing blade the wing locally experiences an upwash due to the propeller slipstream. This upwash increases the local angle of attack. In turn this points the local lift force more forward. And therefore the induced drag decreases. Behind the down going blade the wing experience a downwash and this will in general decrease the local angel of attack and therefore increase the induced drag.

Coming back to the results of the models on the induced drag distribution it can be seen that the options 1 and 3 behave as expected (and explained above).

The choice of the definition of velocity in Equation A.5 can now be understood. Option 3 results in a lift distribution that has good agreement with the experiment and has an induced drag distribution that behaves as expected.

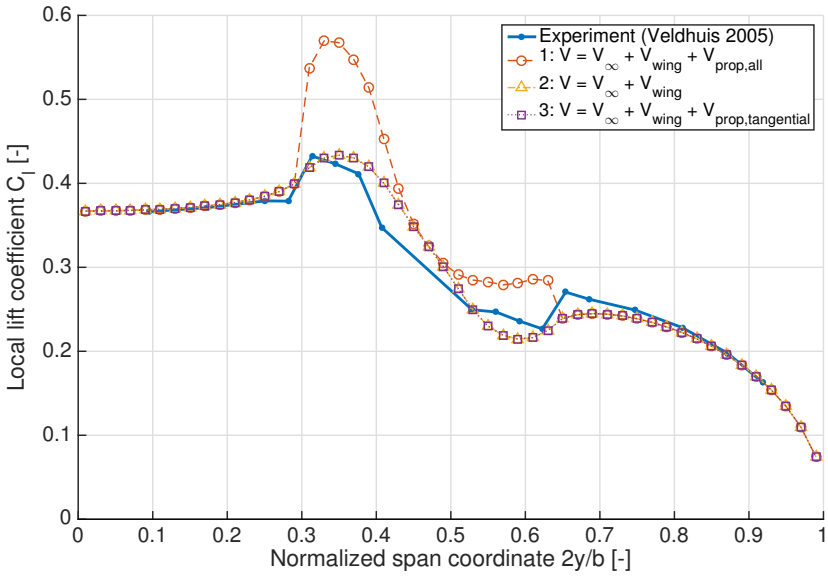

Figure A.2: Predicted lift distribution on PROWIM (at $\alpha = 4$) for two different formulations, compared to experimental results by Veldhuis (3). Note that the propeller location is represented by the vertical black lines.

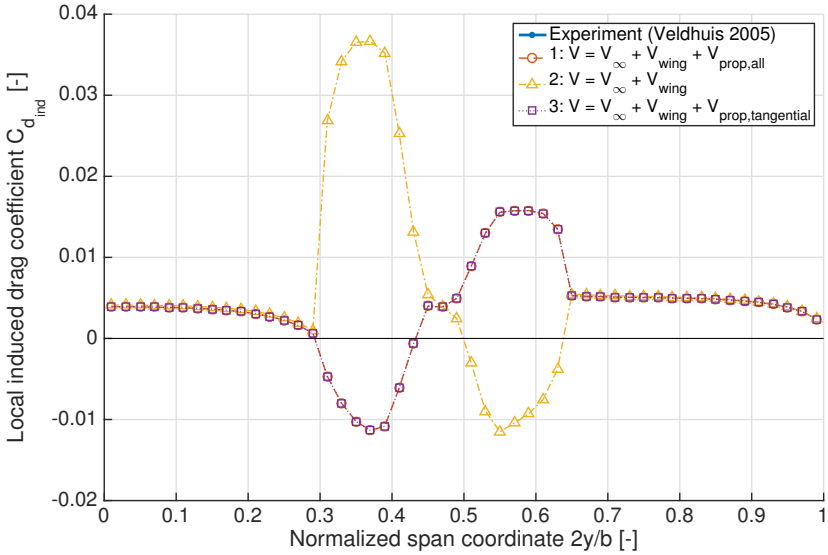

Figure A.3: Predicted induced drag distribution on PROWIM (at $\alpha = 4$) for different definitions for the velocity in Equation A.5. For the induced drag no experimental results were available. Note that the propeller location is represented by the vertical black lines.

A.3 Discussion About the Used Model

In the previous section it is argued that the chosen model best fits the experimental results for the lift distribution and the expectations for the induced drag. However, it is still conceptually strange that only the tangential components of the propeller induced velocities should be added for the calculation of the forces. This section makes a few observations to the use of

this model that can lead to a further investigation into what is physically going on here.

First, the Kutta-Joukowski theorem is derived for an object in a two-dimensional space (or for a straight wing with infinite span). However, this theorem proves to be useful for finite wings as well provided that its aspect ratio is larger than 4. Using the same theorem for a propeller wing interaction problem might be too far away from the 2d assumptions that it is based on.

Second, the propeller slipstream in this method is modelled as a velocity field that varies in both radial and axial direction. The distribution of velocity is determined mainly by the propeller while the effect of the wing is only limited to a general up and downwash by the wing. This effect deflects the slipstream tube somewhat up in front of the wing and somewhat down over and behind it. The structure of the slipstream is not changed.

However, the slipstream might be modelled better by a series of bound and trailing vortices. The trailing vortices are free to move, and will take the form of a helix if a isolated propeller at zero incidence angle is considered. With the presence of the wing the trailing vortices will move differently and will divert locally from the helical shape. With a different orientation of these trailing vortices their induced velocity on the wing also changes. Modelling these effects might increase the understanding of the choice of model made in this Appendix.

Appendix B

Investigation of the Effect of the Individual Slipstream Modification Models

As described in Section 3.5, 5 different slipstream models can be used. In this Appendix the effect of these slipstream models are investigated. The first model, SI, are the slipstream velocities far downstream of the propeller as predicted by XROTOR. Model SII uses the slipstream velocity results from XROTOR and then corrects these values for the finite distance of the wing behind the propeller. This is done by applying the slipstream contraction and axial development of the slipstream. The next model, SIII, is the same as model SII with the addition of a prescribed (and constant) SRF for the tangential velocities in the slipstream. Model SIV is also based on model SII but now with a design based SRF.. The last model, SV, is based on model SIV with the addition of modelling the slipstream deflection.

Figure B.1 shows the lift distribution on the PROWIM model (from Veldhuis (3)) for the Adapted VLM model combined with the different slipstream models. The results are compared with the experimental results. As can be seen, using the more advanced slipstream model is (closer towards SV) the better the prediction of the lift distribution becomes. Note that the slipstream deflection (difference between VLM-SIV and VLM-SV), the swirl recovery (difference between VLM-SII and VLM-SIII) and the design based swirl recovery factor (difference between VLM-SIII and VLM-SIV) are important effects. The slipstream contraction and axial development (difference between VLM-SI and VLM-SII) have only a limited effect.

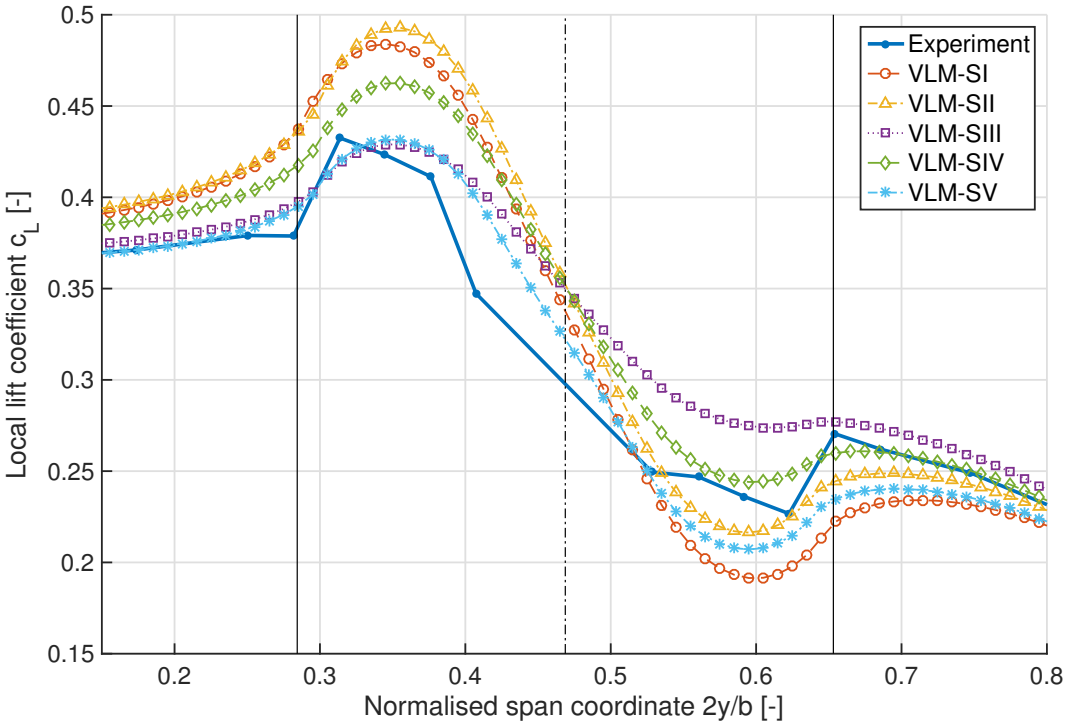

Figure B.1: Lift distribution on PROWIM model for $\alpha = 4$ degrees modelled by the Adapted VLM with the different slipstream models. The experimental results are from Veldhuis (3). Note that the results are zoomed in on the location of the propeller effects and that the propeller location itself is represented by the vertical black lines.

Appendix C

Technical Drawings Of Wings and Wall

This Appendix contains the technical drawings of the following parts produced for the wind tunnel experiment:

- Control wing inboard
- Control wing outboard
- Modified wing inboard
- Modified wing outboard
- Wall frame
- Dummy propeller spinner

C.1 Control Wing Inboard

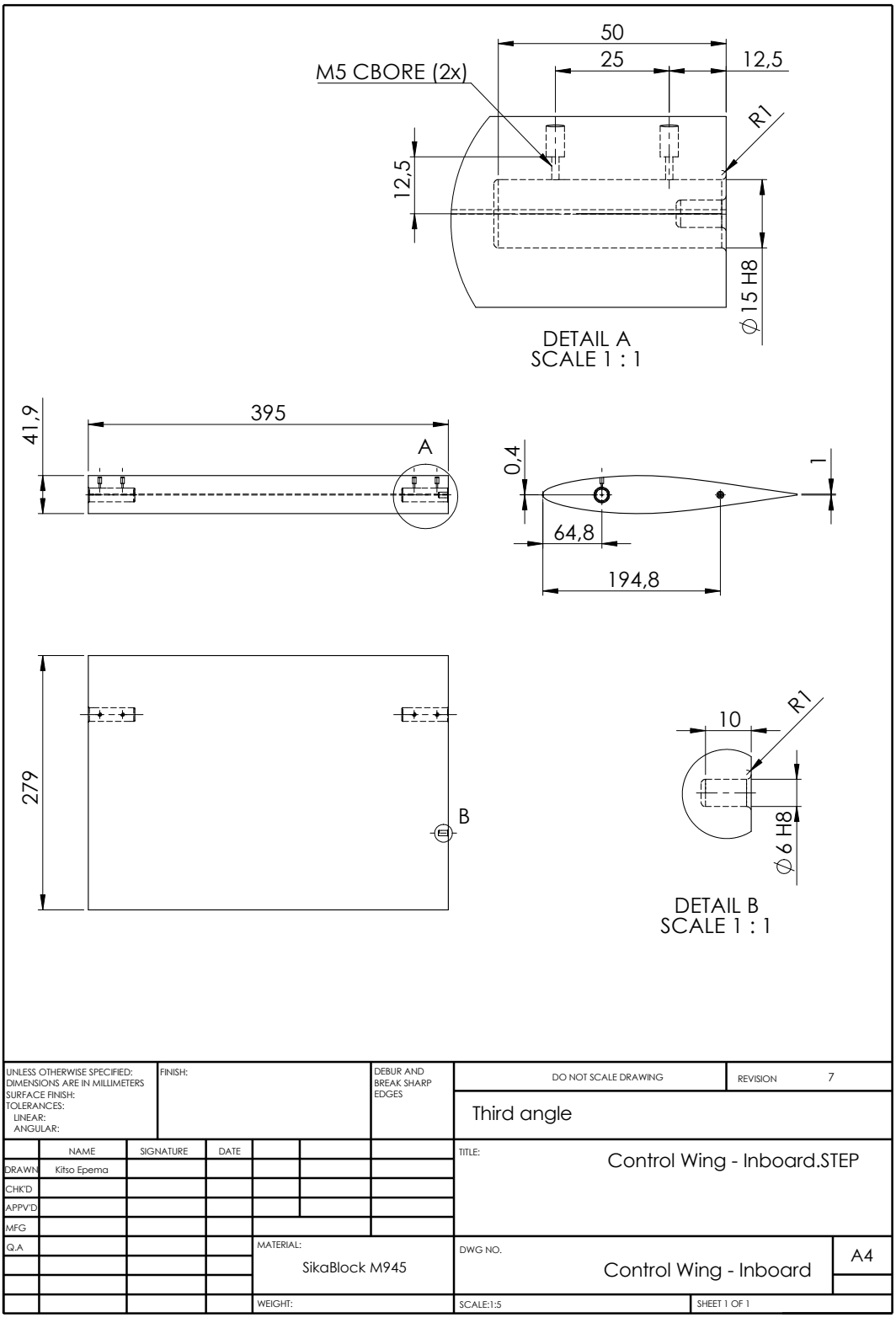

C.2 Control Wing Outboard

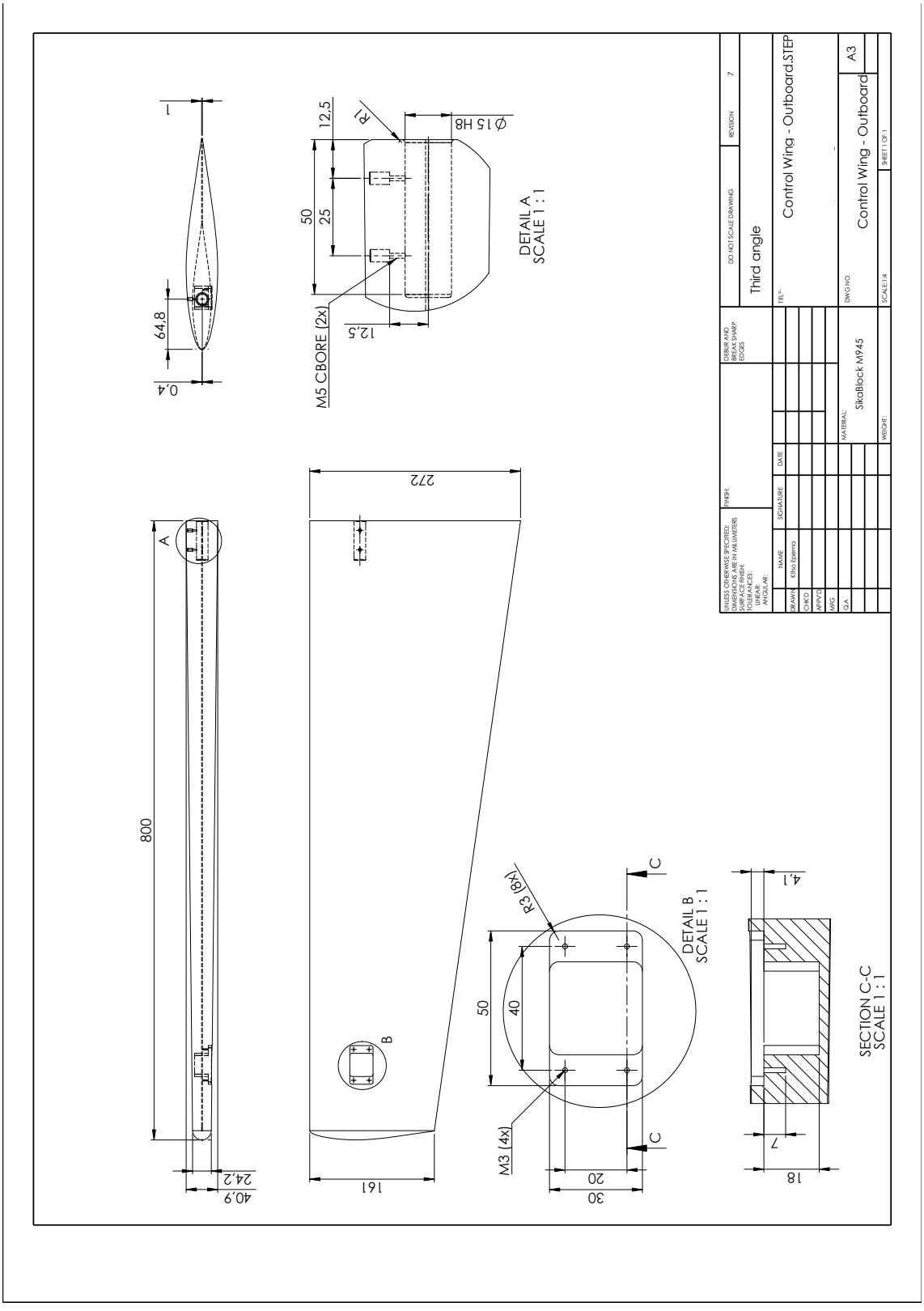

C.3 Modified Wing Inboard

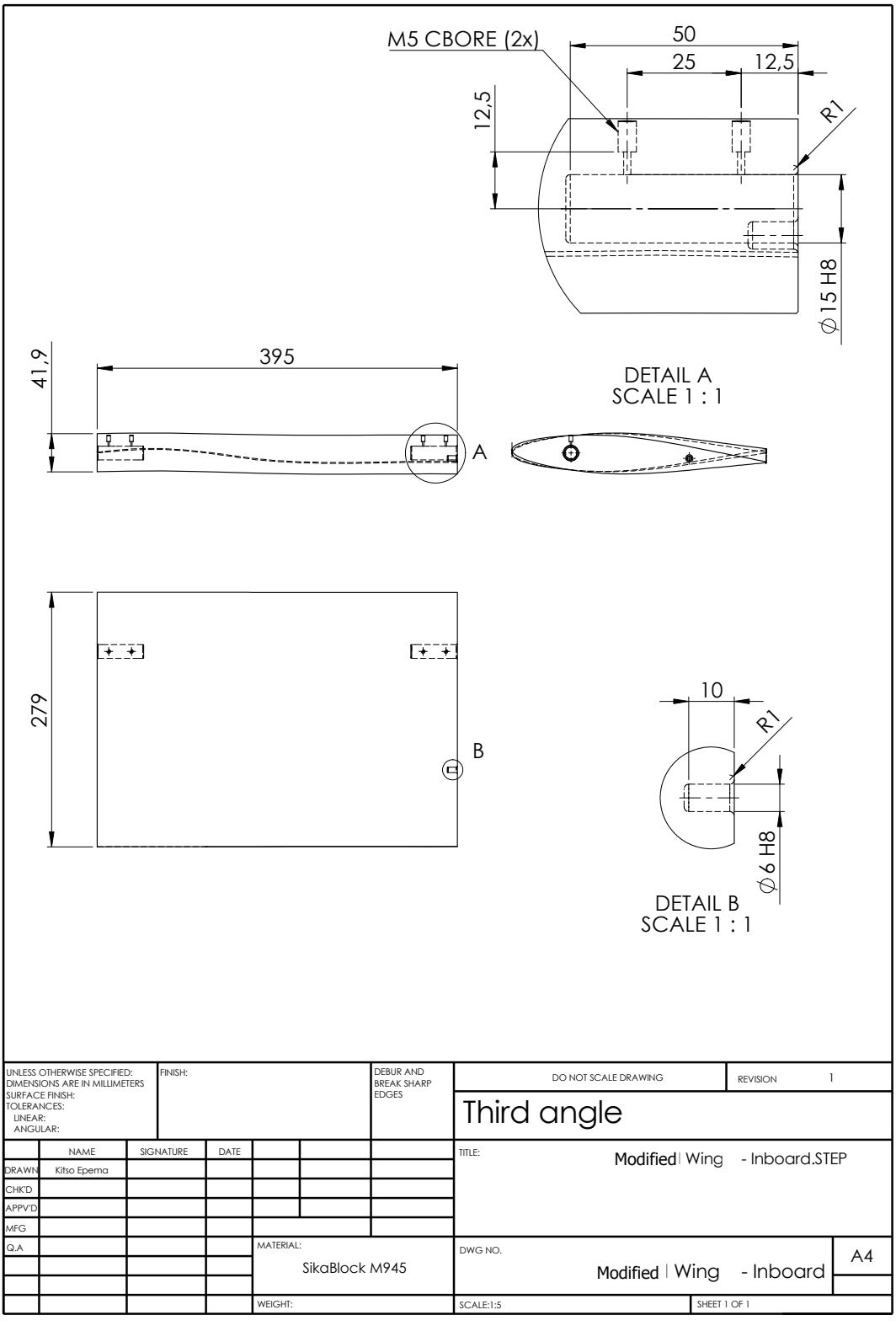

C.4 Modified Wing Outboard

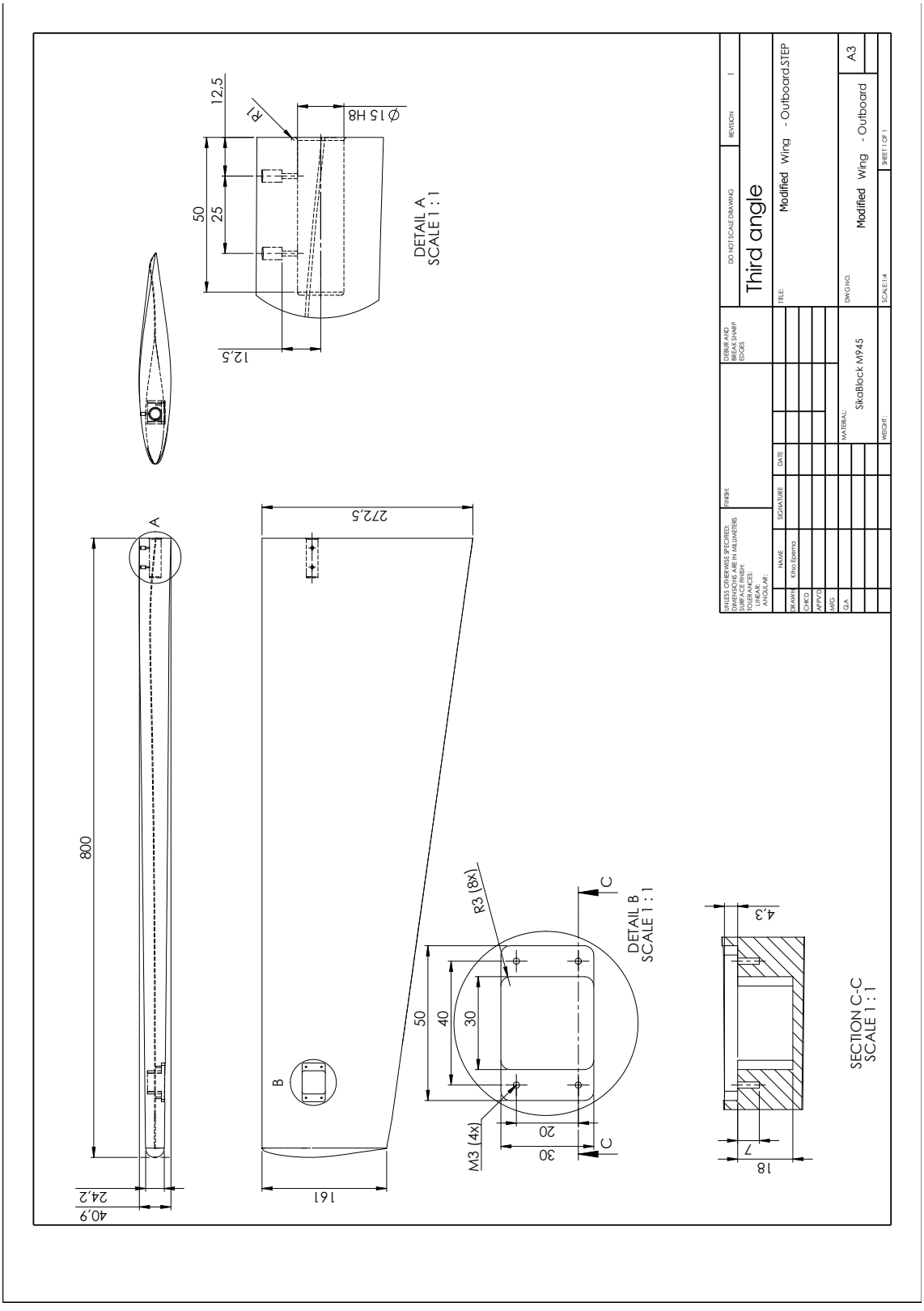

C.5 Wall Frame

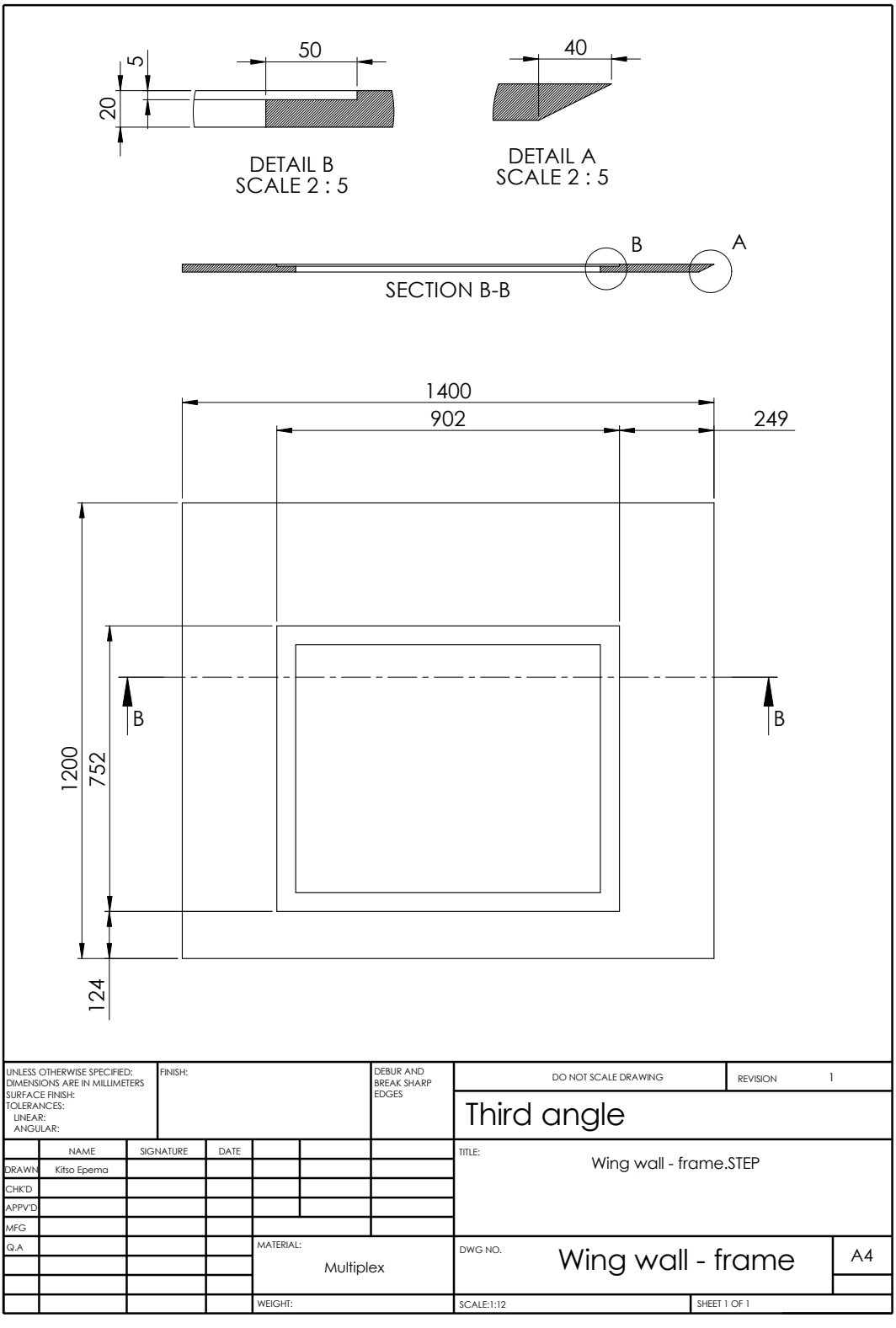

C.6 Dummy Propeller Spinner

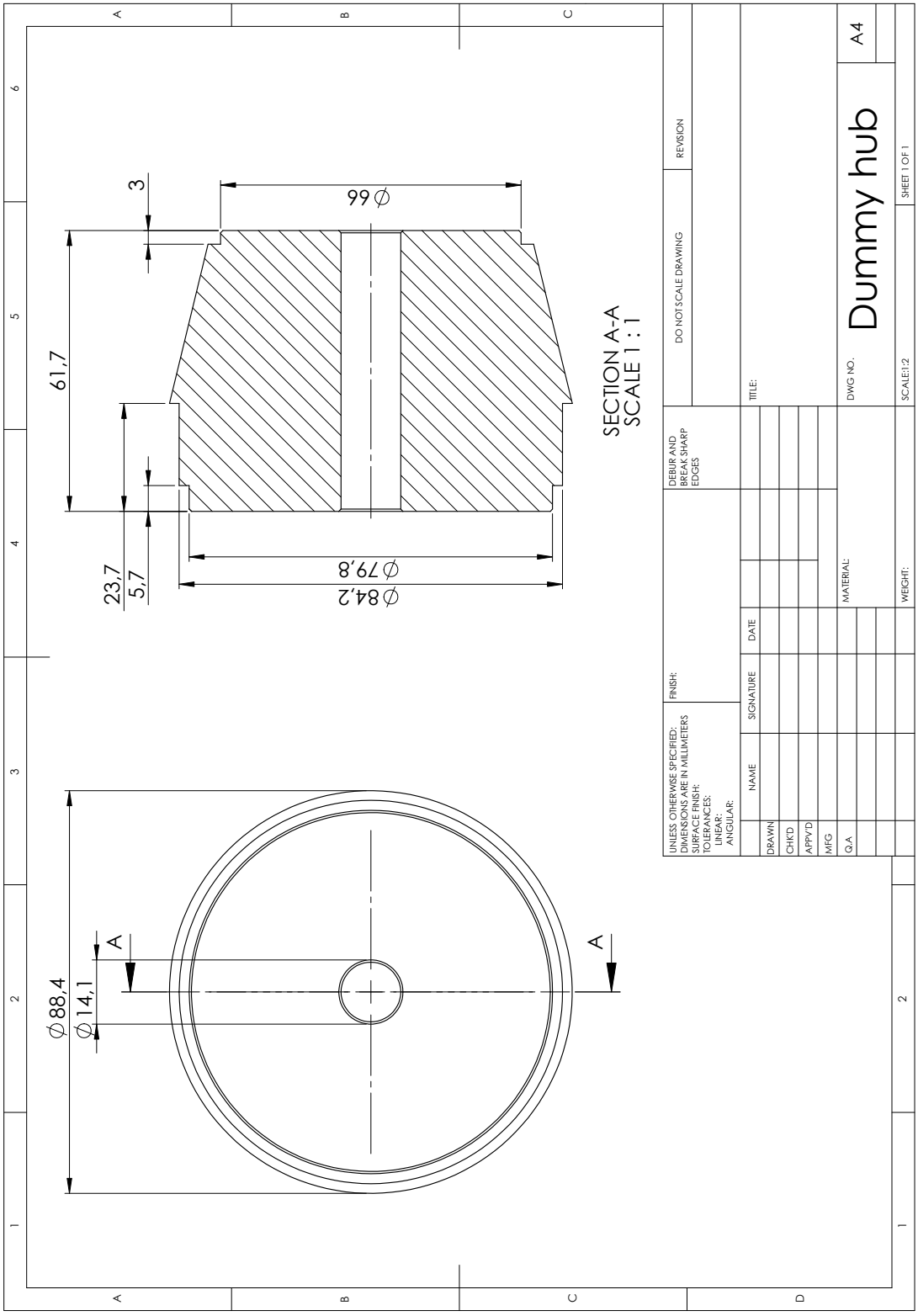

Appendix D

Numerical Investigation of the Effect of the Wall on the Lift Distribution

To verify the wall is large enough to operate as an effective symmetry plane an analysis is performed with the VLM SIM model. Three wing configurations are analysed with the numerical model: full span wing, only the right wing and the right wing with the wall. Figure D.1 shows the circulation distribution of all three configurations. As can be seen the circulation distribution of the wing with wall is almost equal to the full span wing. This means the wall is expected to be an effective symmetry plane.

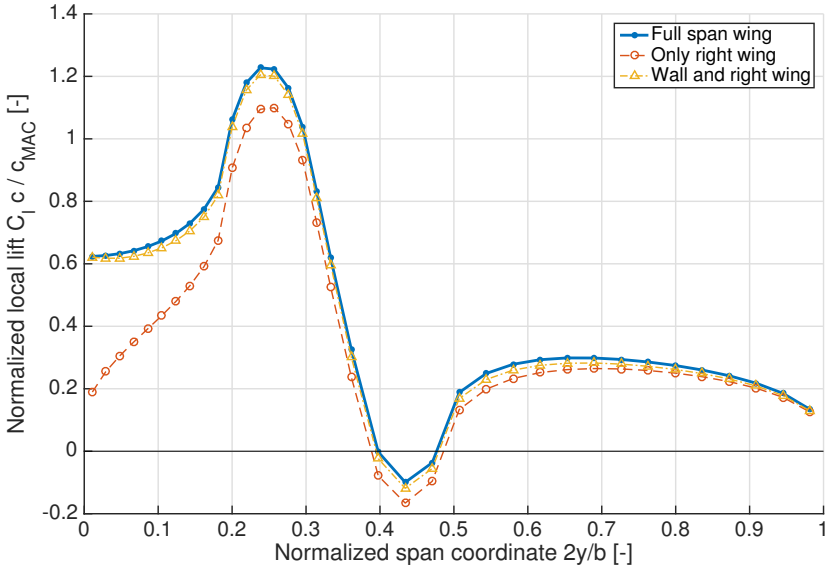

Figure D.1: Lift distribution of a full span wing, only right wing and right wing with wall. The distribution for the wing with wall is almost equal to the full span wing which shows the wall is expected to be an effective symmetry plane.

Appendix E

Uncertainty in PIV Measurement

There are a number of sources of uncertainty in PIV measurements and the post processing of the images afterwards. This uncertainty is quantified here.

These are the parameter influencing the uncertainty as given by Raffel (28).

- Particle image diameter
- Particle image shift
- Particle image density
- Quantization level
- Background noise
- Displacement gradient
- Out of plane motion

Out of plane motion is quantified within the particle image density and is therefore not shown in Tables E.1 and E.2.

The error in the velocity is in the order of approximately 0.5 m/s.

Table E.1: Summary of parameters of PIV measurement.

Parameter	**Symbol**	**Value**	**Unit**
Free stream velocity	V_∞	19	m/s
Time step between frames	d_t	30	μs
Pixel size		17.5	$pixel/mm$
Particle image diameter	d_τ	1-3	$pixel$
Particle image shift		10	$pixel$
Particle image density	N	varying	
Background noise		10 %	-
Displacement gradient		varying	$pixels/pixel$
Quantization level	QL	8	bit

Table E.2: Uncertainty in PIV measurements.

Source	**RMS (pixel)**	**RMS (m/s)**
Particle image diameter	0.10	
Particle image shift	0.02	
Particle image density	0.03	
Background noise	0.03	
Displacement gradient	0.05	
Quantization level	0.03	
Total	0.26	0.495

Appendix F

Effect of Twist on the Wing Inside the Slipstream on the Induced Drag Distribution

The initial approach to decrease the induced drag of a wing in a tractor propeller configuration is to increase the twist angle of the wing in the section of the slipstream behind the up going blade. The effect of this change in the twist distribution on the induced drag is investigated in this section. Based on the Control wing, two new wings are designed by changing only the twist distribution on the wing section inside the inboard part of the propeller slipstream. On this wing section the twist is increased for the Twist up wing and decreased for the Twist down wing, as shown in Figure F.1.

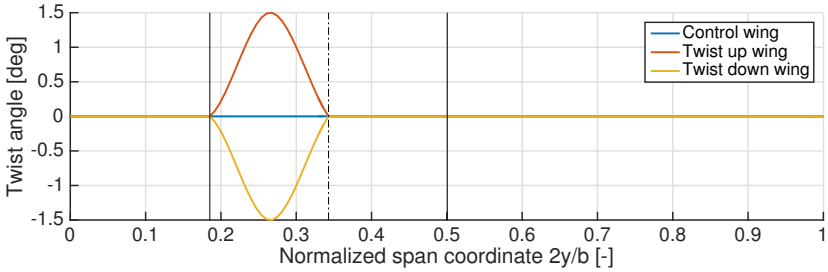

Figure F.1: Twist distribution for the Control, Twist up and Twist down wing.

These three wings are analysed with PW-VLM-SV at the wind tunnel experiment operating conditions. The resulting lift and induced drag coefficients are shown in Table F.1. Compared to the Control wing the increase of wing twist on the Twist up wing also increases the lift coefficient and the decrease of the wing twist on the Twist down wing decreases the lift coefficient, as expected. For the induced drag, however, the effect of the change of wing twist is not as initially expected. Actually, with the increased wing twist the induced drag is increased with respect to the Control wing, and the other way around for a decrease of the wing twist.

In order to explain why the induced drag behaves this way remember that the induced drag

Table F.1: Lift and induced drag coefficients for the Control, Twist up and Twist down wings at wind tunnel experiment operating conditions (method: PW-VLM-SV).

Wing	C_L	$C_{D_{ind}}$	$\Delta C_{D_{ind}}$
Control wing	0.384	-0.00987	-
Twist up wing	0.406	-0.00946	0.00016
Twist down wing	0.372	-0.00968	-0.00006

is the product of the density, circulation and total induced downwash:

$$d_{ind} = \rho\Gamma \left(w_{wing} + w_{prop}\right) \tag{3.40}$$

The distribution of the circulation and total induced downwash are shown in Figure F.2. First consider the wing section inside the inboard part of the slipstream of the Control wing. Here a peak in the lift distribution (Figure F.2(a)) coincides with a negative total downwash (Figure F.2(b)), which results in a negative induce drag (Figure F.2(c)). For the Twist up wing the circulation is increased with respect to the Control wing (on the same wing section). The total downwash is also increased which results in a higher (less negative) induced drag. For the Twist down wing the effect is reversed, a lower lift with a lower downwash causes a lower induced drag.

In order to explain the change in the total downwash first consider the section of the Control wing inside the inboard part of the slipstream again. This part of the wing generates a stronger circulation (and also lift) then the surrounding parts of the wing. This can be modelled by a stronger bound vortex together with two trailing vortices on both sides of this wing section. The trailing vortices induce a downwash on this wing section which partly counteracts the upwash (or negative downwash) induced by the propeller. Since the total downwash is still negative (the upwash of due to the propeller is stronger than the wing induced downwash) the induced drag on this wing section is negative. Now compare the distribution of the circulation, downwash and induced drag of Twist up wing with those of the Control wing on the same wing section. The increase of circulation on the Twist up wing also increases the strength of the downwash induced by the trailing vortices on this wing section. The propeller upwash is not affected which results in an increased downwash. The same effect, but reversed, happens for the Twist down wing.

The fact that the induced drag is the product of the circulation and the downwash, and that the downwash depends on the distribution of circulation suggests there is an optimum circulation distribution to minimize the induced drag. This is confirmed by analysing the induced drag on a set of wings, the Twist varying wings, with varying twist distributions, similar as the Twist up and Twist down wings. The set of wings have non zero twist angle on the wing section inside the inboard part of the propeller slipstream. The maximum value of the twist angle is varied between -5 and 5 degrees. Figure F.3 shows the induced drag coefficient of the new wing versus the maximum twist angle of that wing. As can be seen the induced drag finds a minimum around a maximum twist angle of -2 degrees.

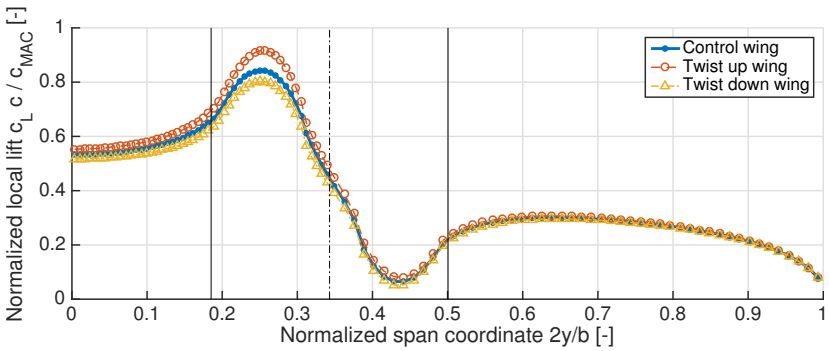

(a) Circulation distribution

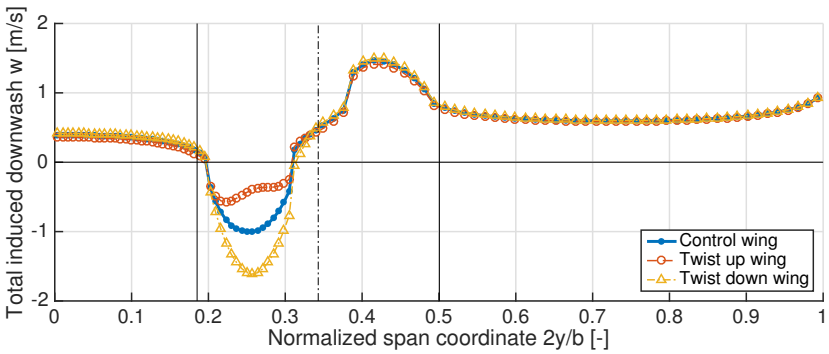

(b) Downwash distribution

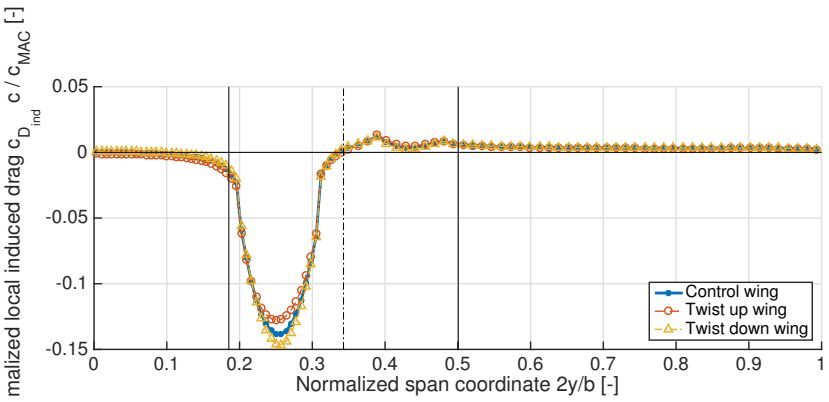

(c) Induced drag distribution

Figure F.2: Distribution of the lift, total downwash and induced drag for the Control, Twist up and Twist down wing analysed with PW-VLM-SV at the wind tunnel experiment operating conditions.

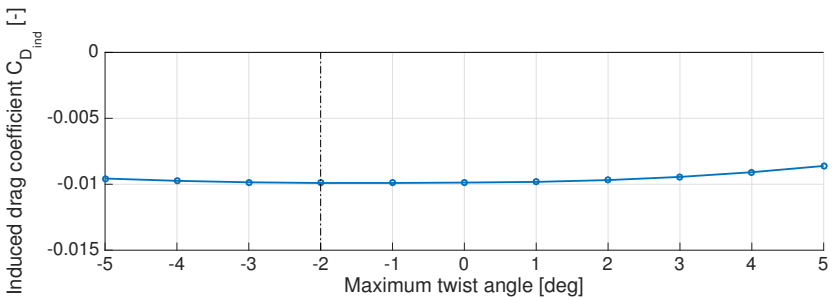

Figure F.3: Induced drag of the Twist varying wings versus the maximum value of the wing twist. The vertical dotted line indicates value of the maximum twist angle for the minimum induced drag.